惑星大気研究会：あかつき・金星ワークショップ (2016/03/28–29，神戸大学・CPS)

金星大気スーパーローテーションの理論と数値的研究

高木征弘（京都産業大学理学部）

スーパーローテーションの理論

- 夜昼間対流メカニズム
- 熱潮汐波メカニズム
- 重力波メカニズム
- 子午面循環メカニズム
- 多重平衡解
- 熱潮汐波＋子午面循環メカニズム

夜昼間対流メカニズム

- Schubert and Whitehead (1969)
- Thompson (1970)
- Takagi and Matsuda (1999, 2000)

Moving flame mechanism

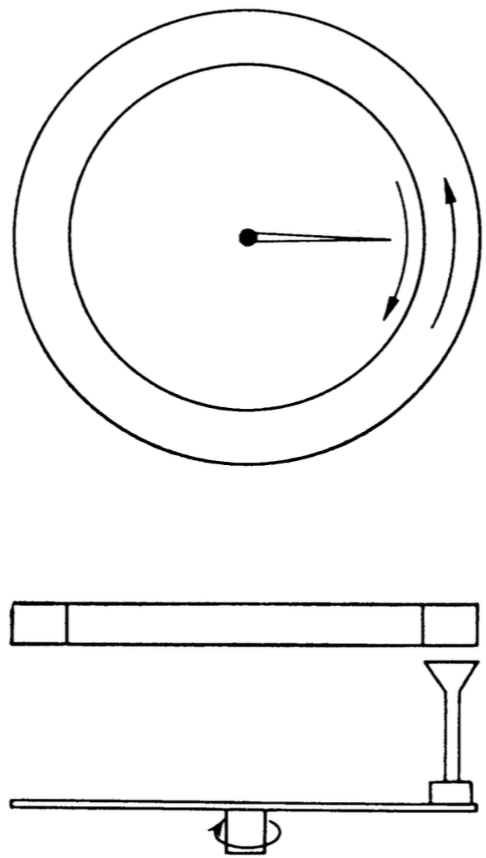

Fig. 1. Schematic diagram of the apparatus for the moving flame experiment.

The speed of the flame was 1 mm/sec. In a steady state, the mercury was rotating so rapidly in a direction counter to that of the flame, about 4 mm/sec.

Schubert and Whitehead (1969)

Thompson mechanism

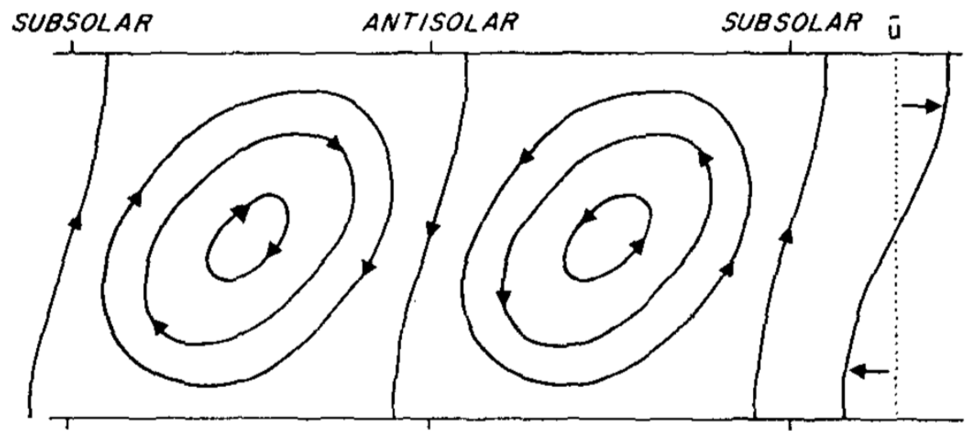

FIG. 1. Interaction between the mean shear and the tilted cells.

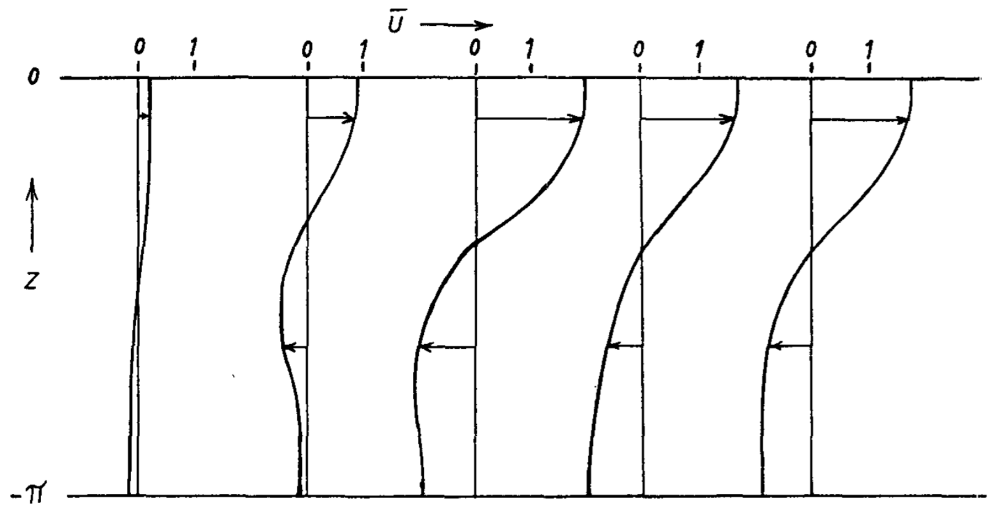

FIG. 6. Mean zonal wind $\bar{u}$ for $t=0.0$, 10.2, 26.2, 106.3, 122.2 and 166.8, with $K=0.1$, $E=0.01$, $G=1$, $\Gamma=1$.

Thompson (1970)

Takagi and Matsuda (1999, 2000)

- Thompson (1970) を三次元球面上に拡張し，夜昼間対流の線型安定性を調査　→安定

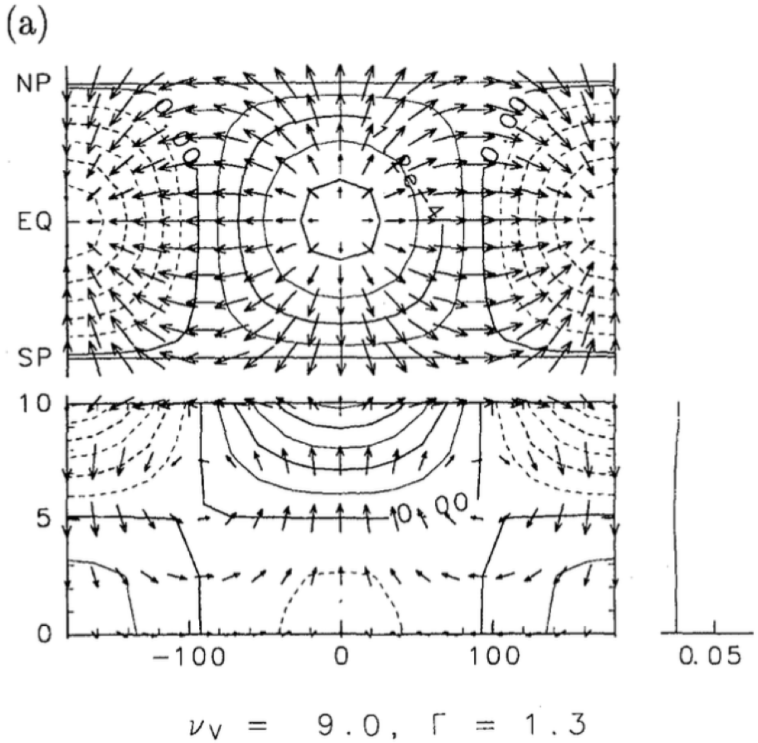

Takagi and Matsuda (1999)

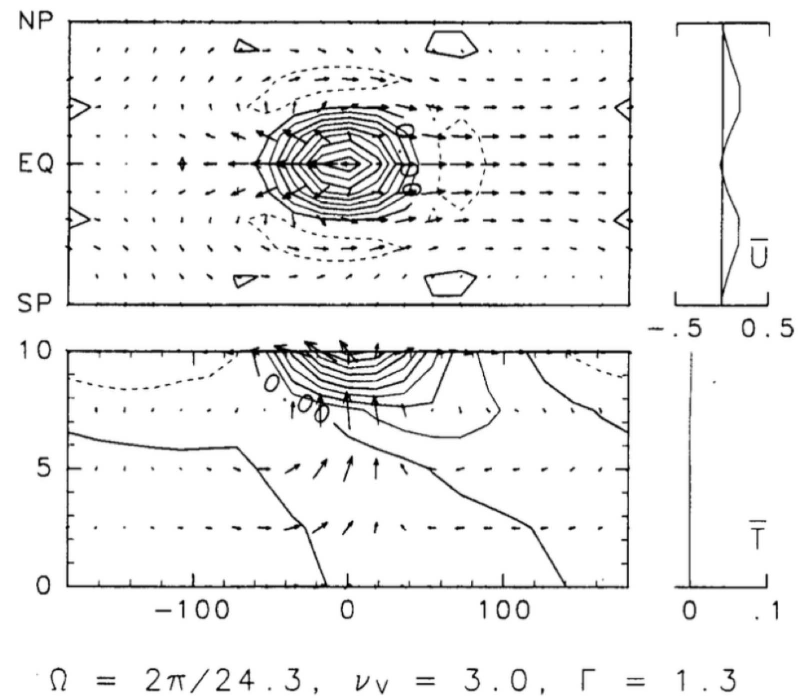

Takagi and Matsuda (2000)

熱潮汐波メカニズム

- Fels and Lindzen (1974)
- Plumb (1975)
- Pechmann and Ingersoll (1984)
- Newman and Leovy (1992)
- Takagi and Matsuda (2005, 2006, 2007)
- Lebonnois et al. (2010, 2016 in revision)

熱潮汐波メカニズム

- 鉛直伝播する波の運動量輸送で平均流生成

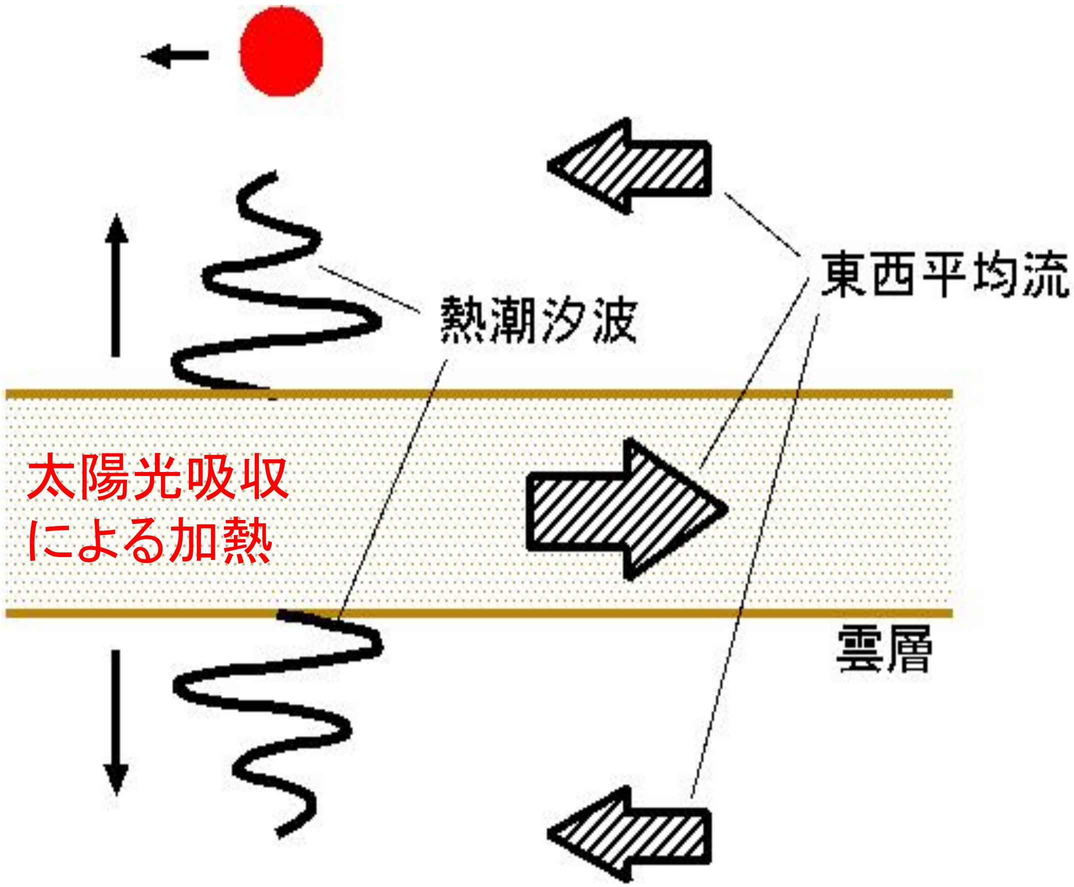

金星大気中の太陽光吸収

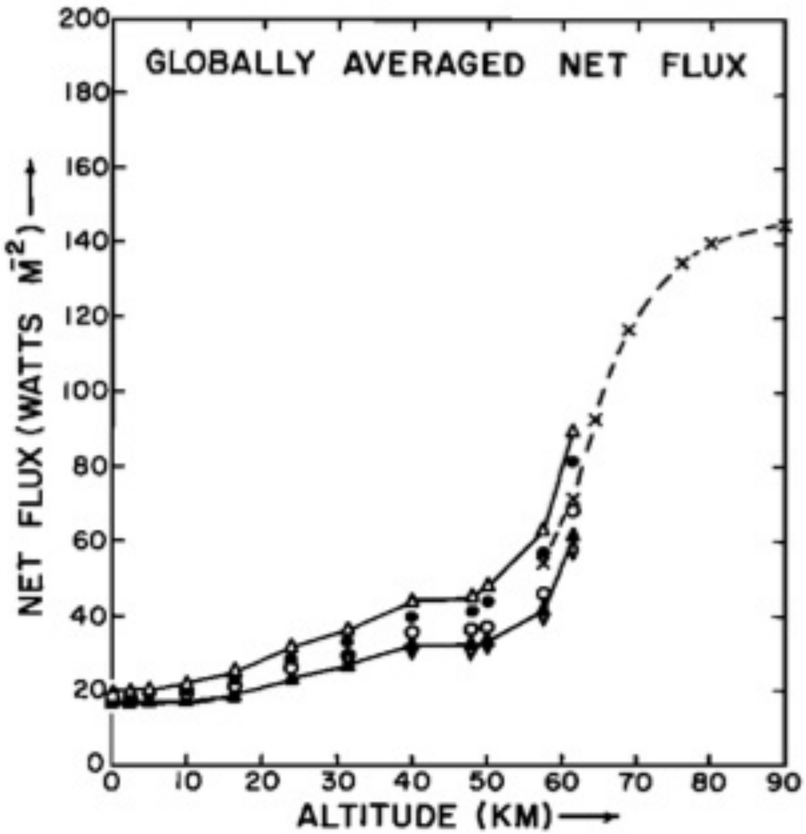

Fig. 17. The total (bolometric) net flux averaged over the entire planet using the scale factors of Table 7. Symbols are the same as for Figure 16.

Tomasko et al. (1980)

熱潮汐波による平均流

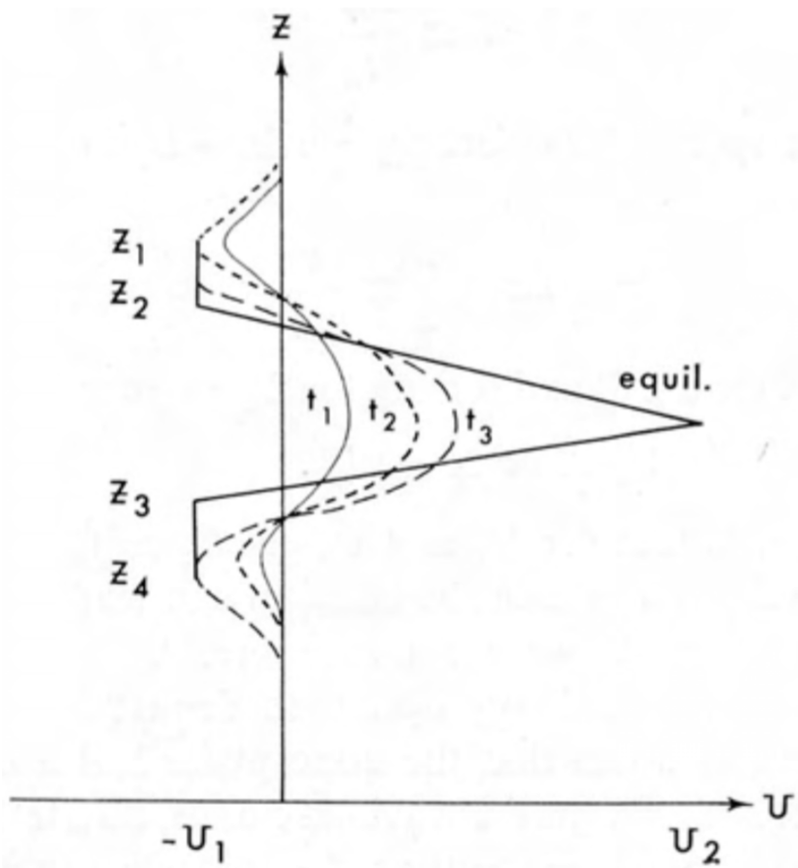

Fels and Lindzen (1974)

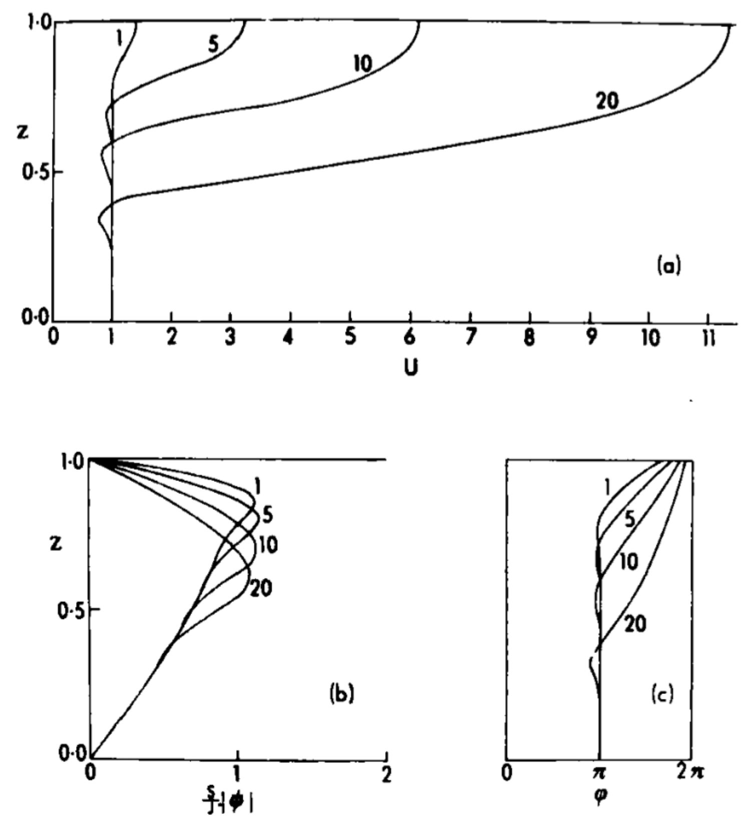

Plumb (1975)

熱潮汐波の空間構造

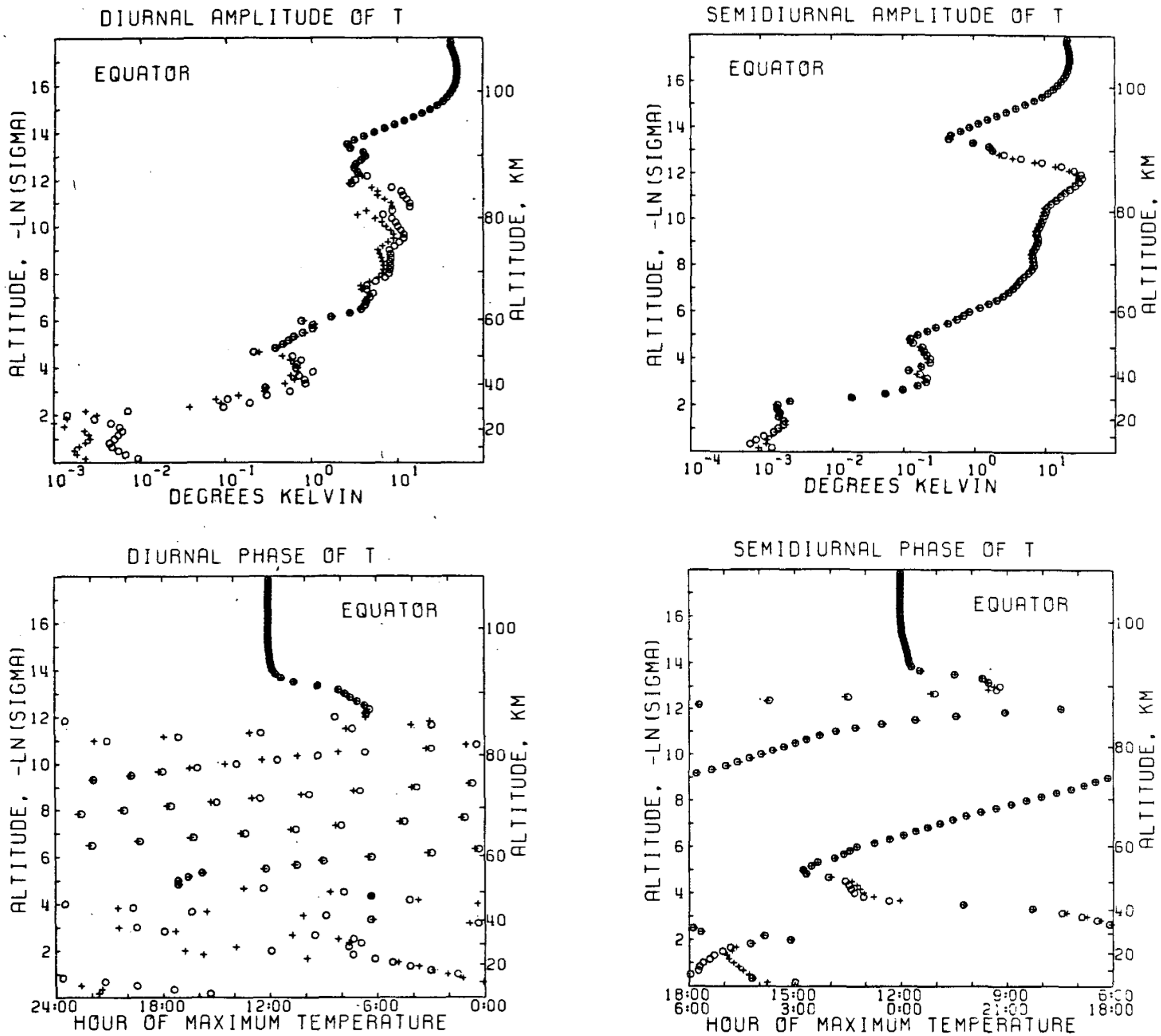

Pechmann and Ingersoll (1984)

弱非線型モデルによる検証

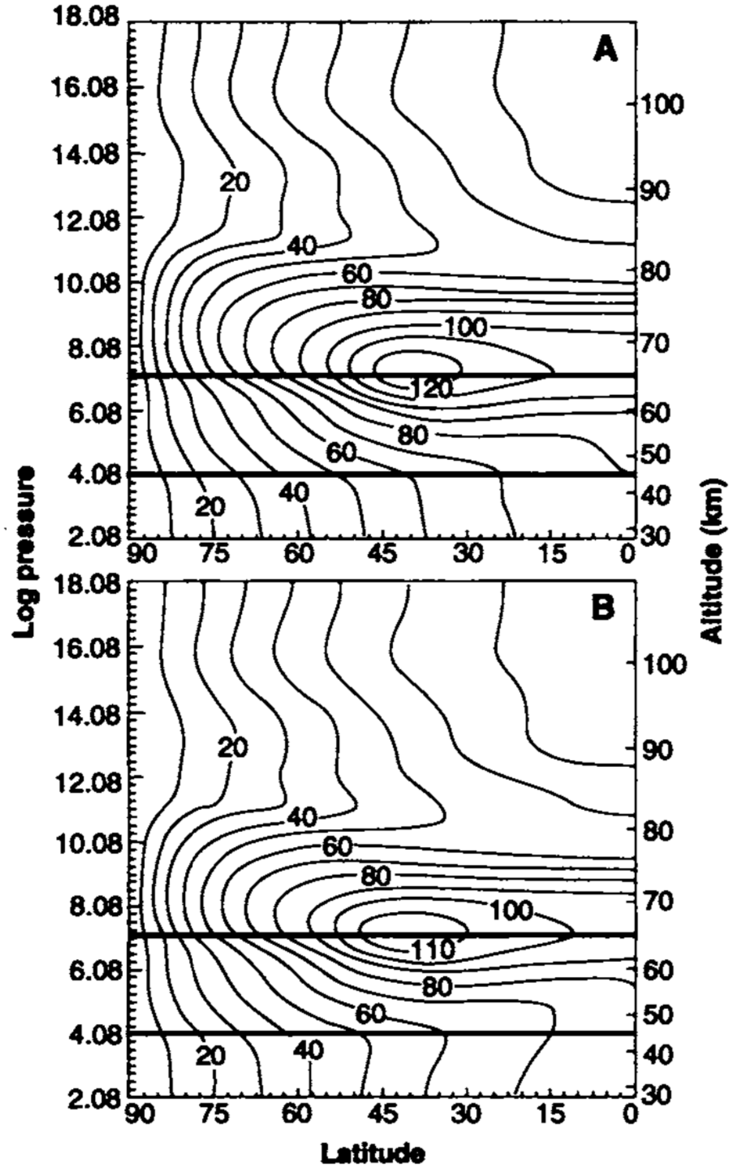

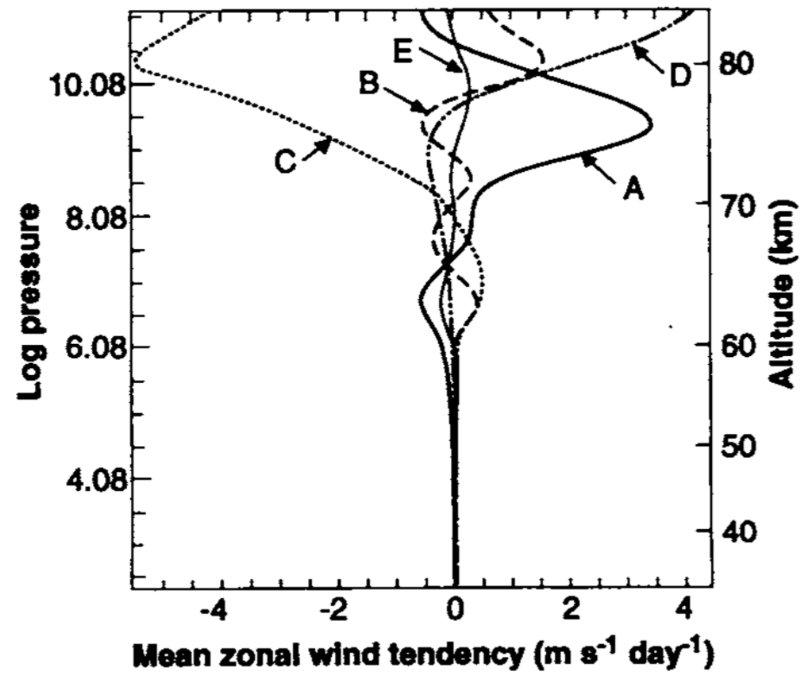

Fig. 2. Contributions to mean zonal flow acceleration on the equator from: (A) advection by zonal mean vertical velocity, (B) momentum flux convergence of the semidiurnal tide, (C) momentum flux convergence of the diurnal tide, (D) Rayleigh friction, (E) vertical diffusion. Averages are for the last 40 days of the 300-day simulation with initial sheared angular velocity.

Newman and Leovy (1992)

熱潮汐波に伴う水平風速

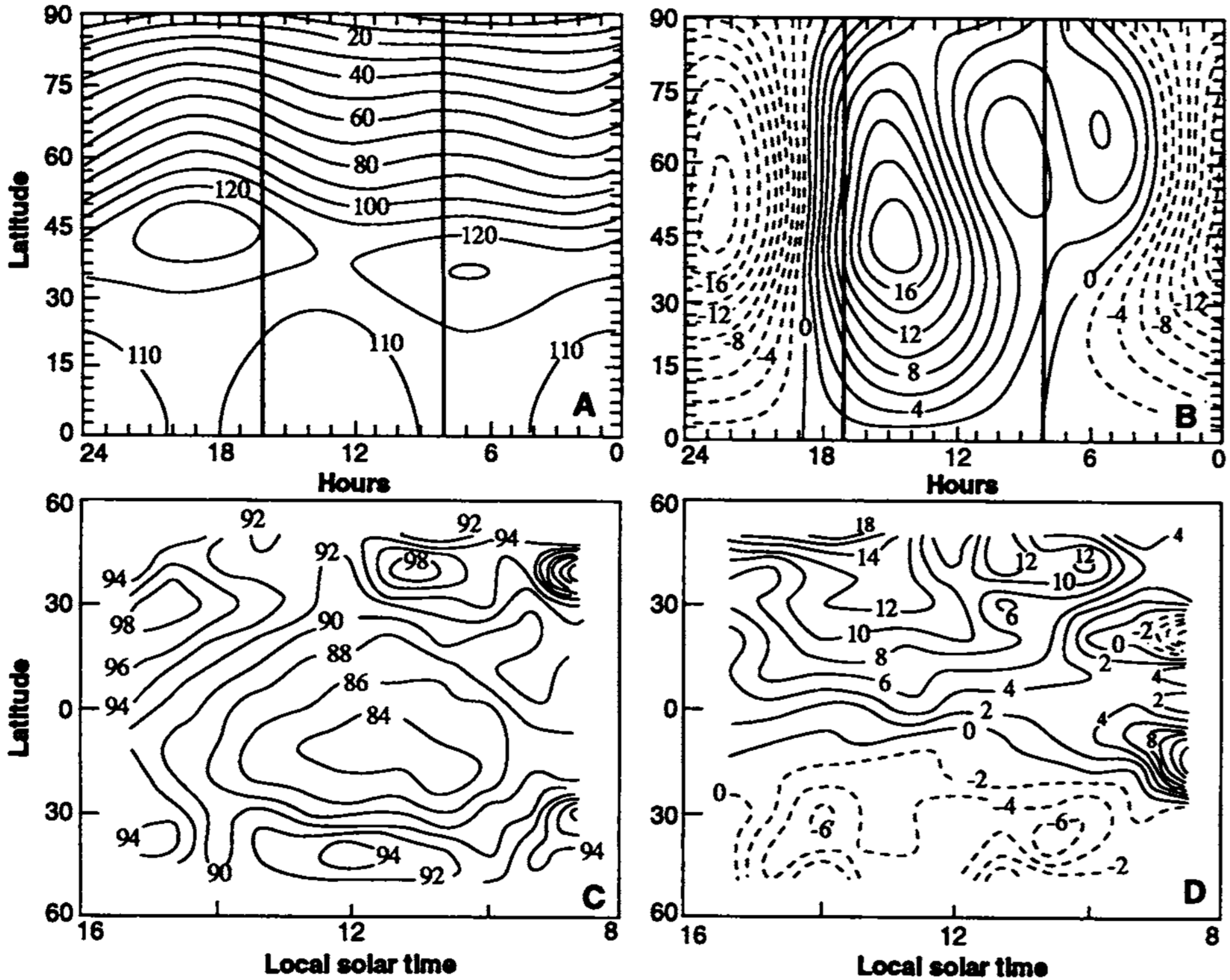

Newman and Leovy (1992)

熱潮汐波の鉛直構造

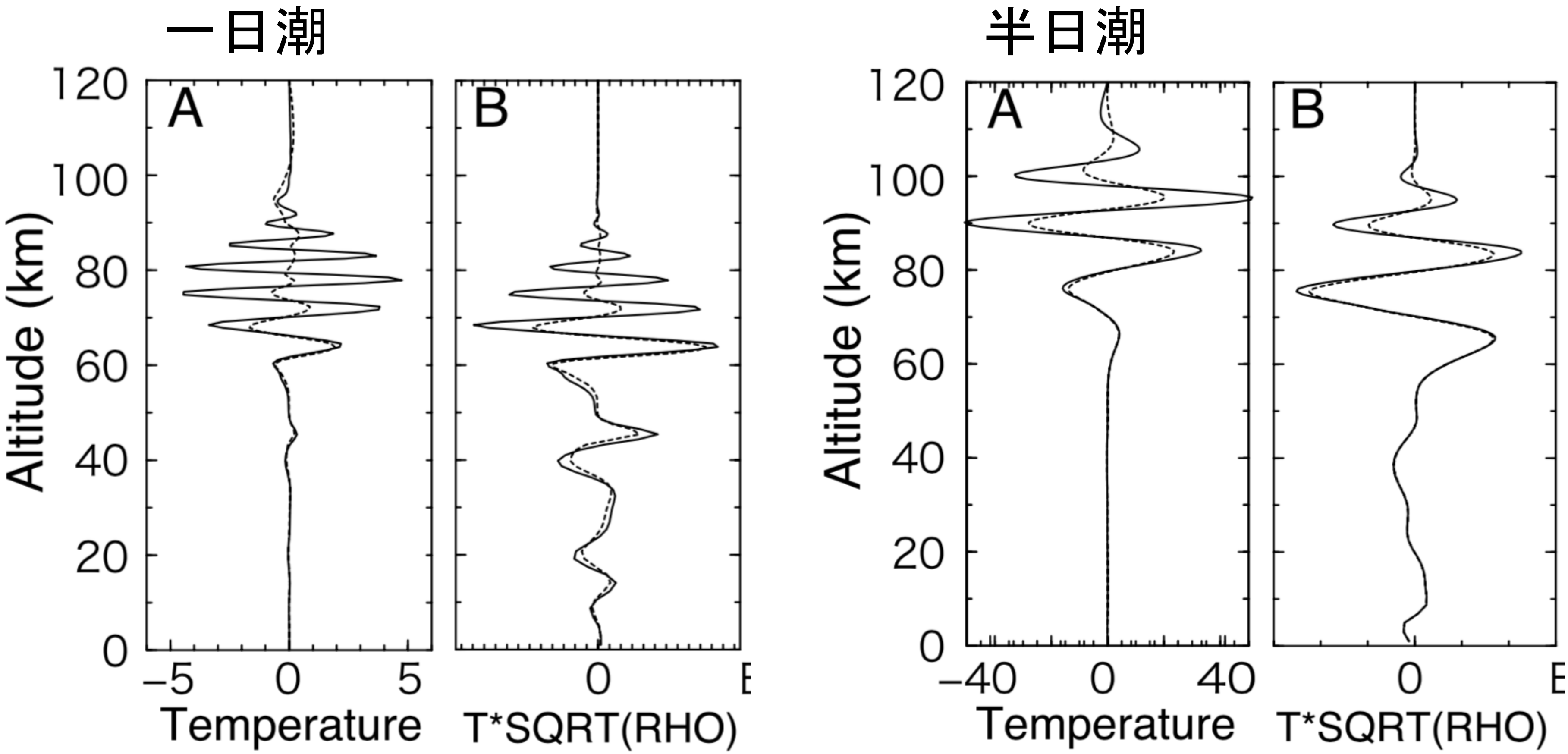

Takagi and Matsuda (2005)

熱潮汐波に伴う水平風速 (2)

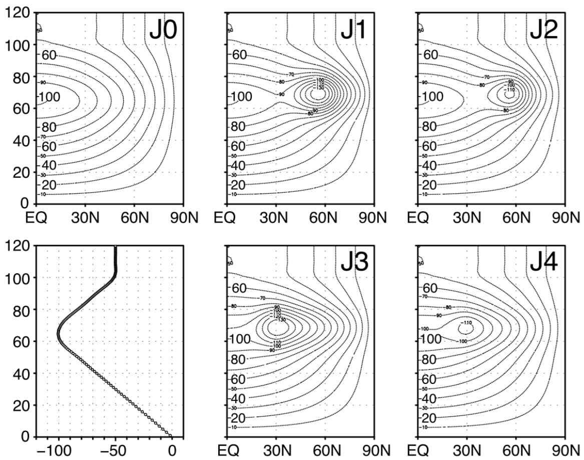

U+u’ at 70 km

v’ at 70 km

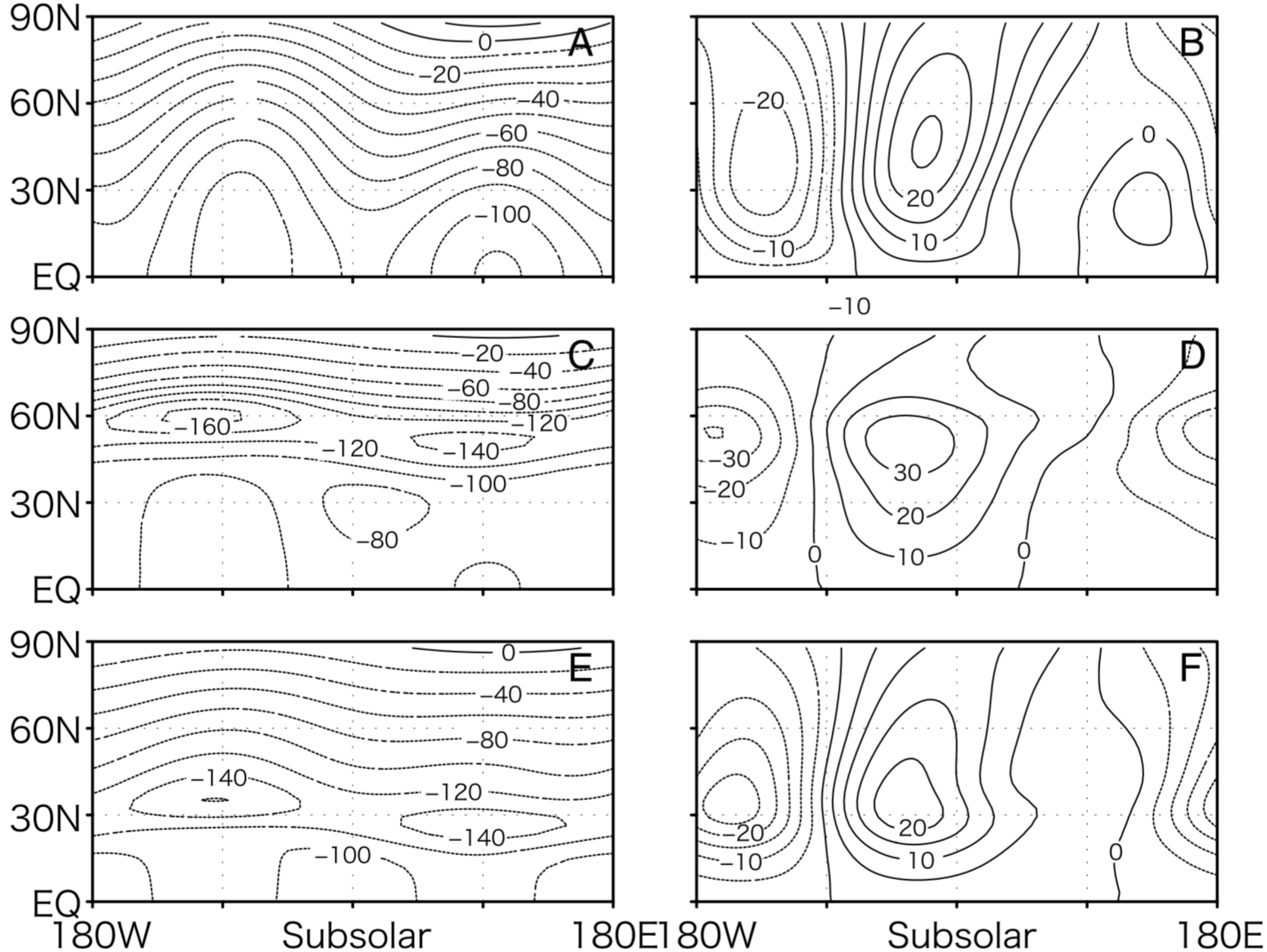

Takagi and Matsuda (2005)

熱潮汐波の鉛直伝播と運動量輸送

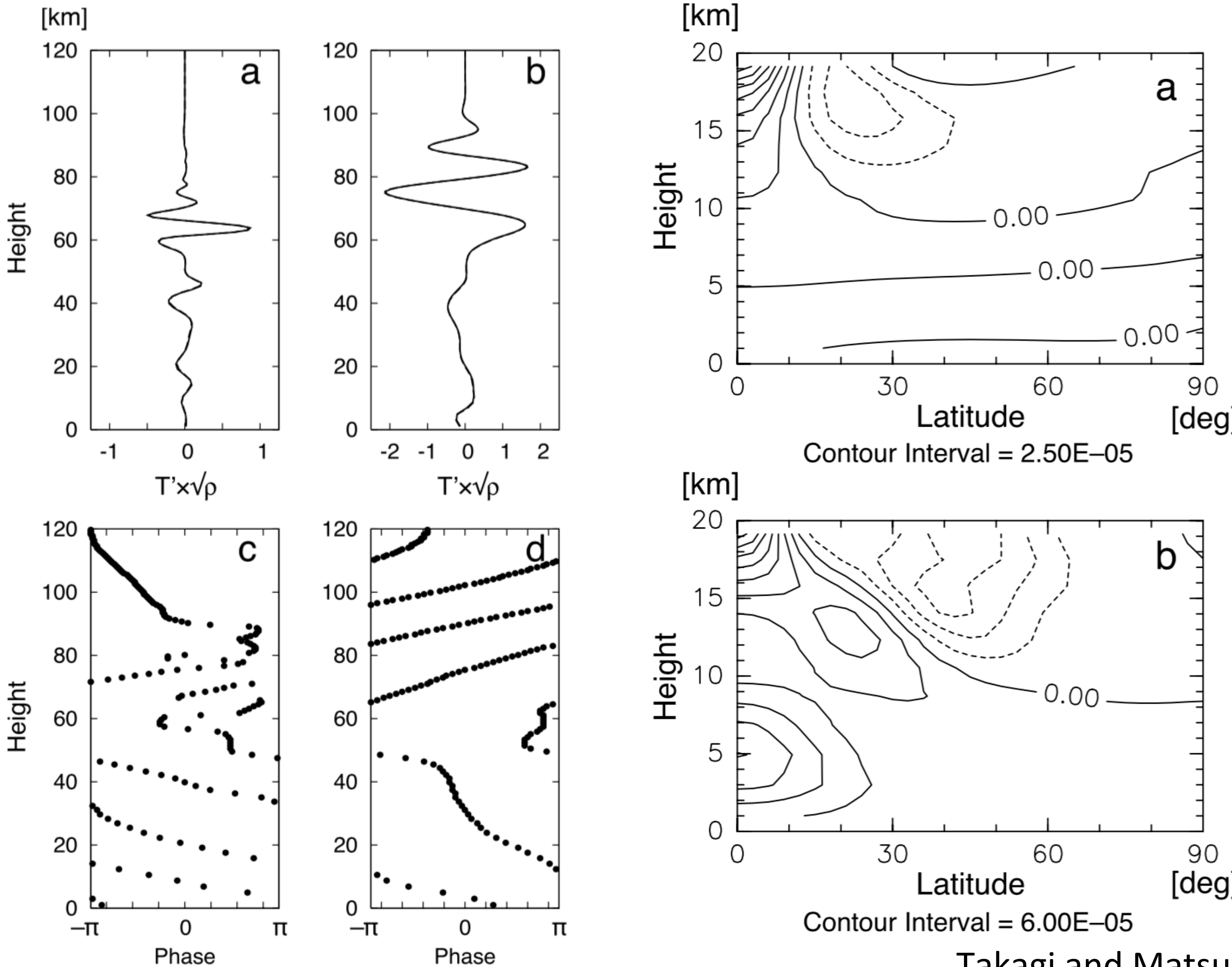

Takagi and Matsuda (2006)

重力波メカニズム

- Hou and Farrel (1987)
- 池田 (2007, 2011)

重力波メカニズム

- 下層から上方伝播する重力波の臨界高度吸収により 0–45 km の平均流を生成･維持

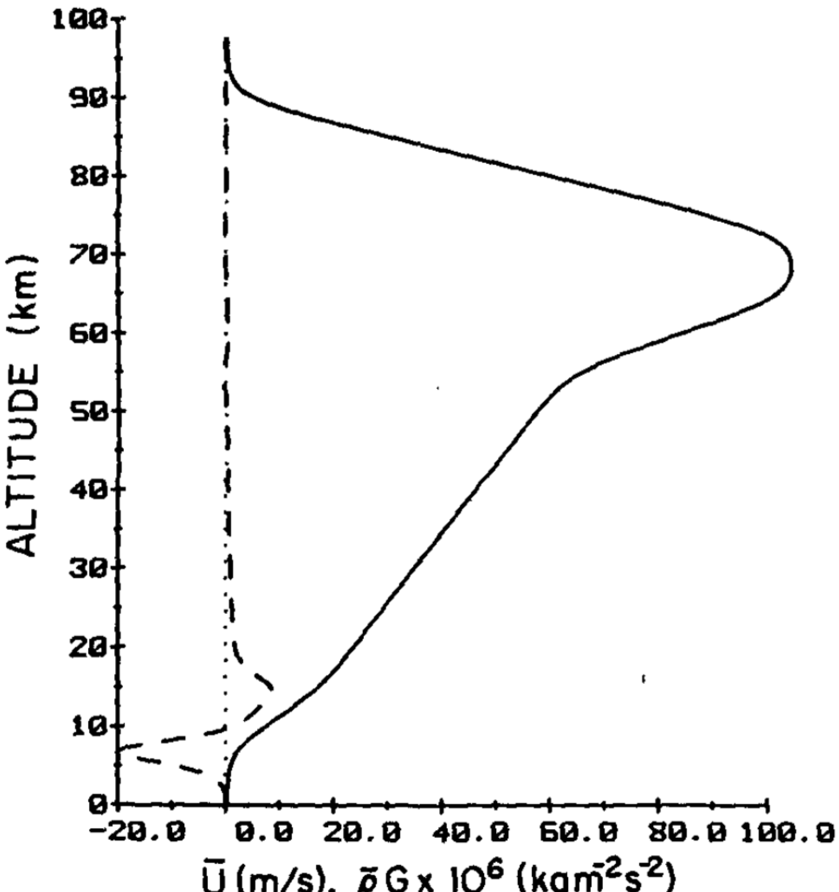

Hou and Farrel (1987)

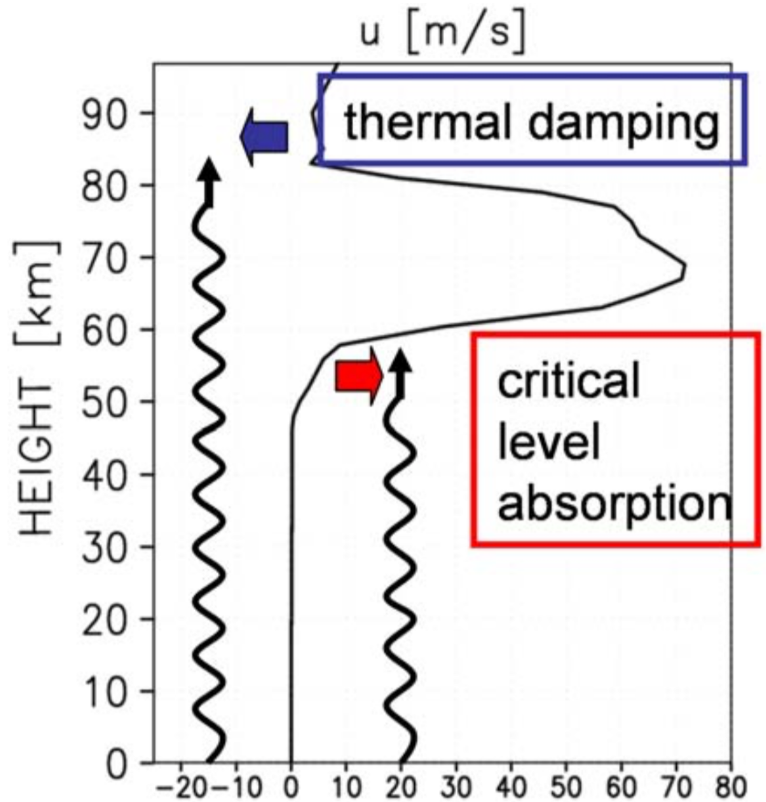

池田 (2007)

重力波メカニズムの数値実験

重力波パラメタリゼーションなし

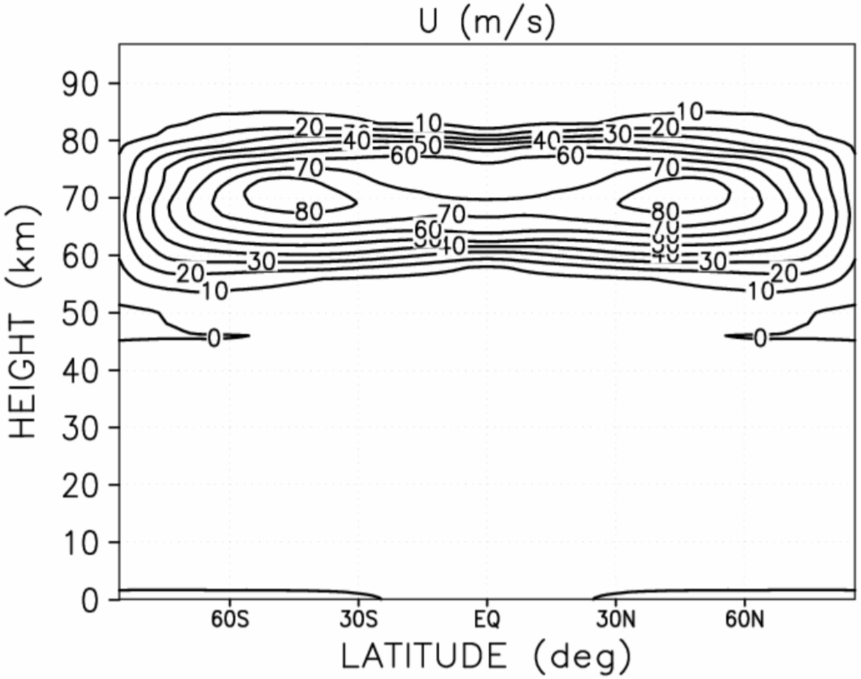

重力波パラメタリゼーションあり

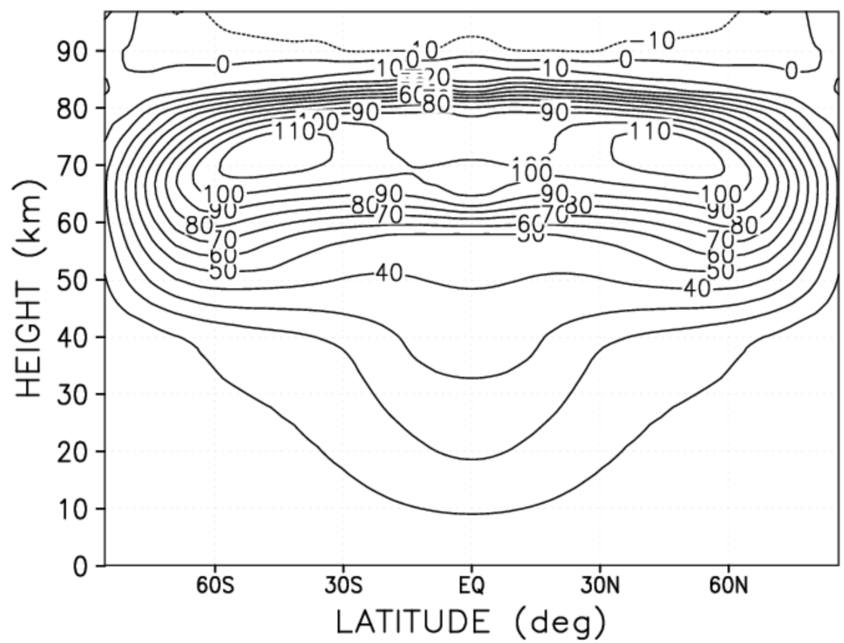

池田 (2007)

子午面循環メカニズム

- Gierasch (1975)
- Rossow and Williams (1979)
- Matsuda (1980, 1982)
- Yamamoto and Takahashi (2003a,b, 2004, …)
- Lee et al. (2005, 2007)
- Hollingsworth et al. (2007)
- Yamamoto et al. (2009), Yamamoto and Yoden (2013)
- Parish et al. (2011)
- Lebonnois et al. (2013) →モデル間比較

Gierasch mechanism

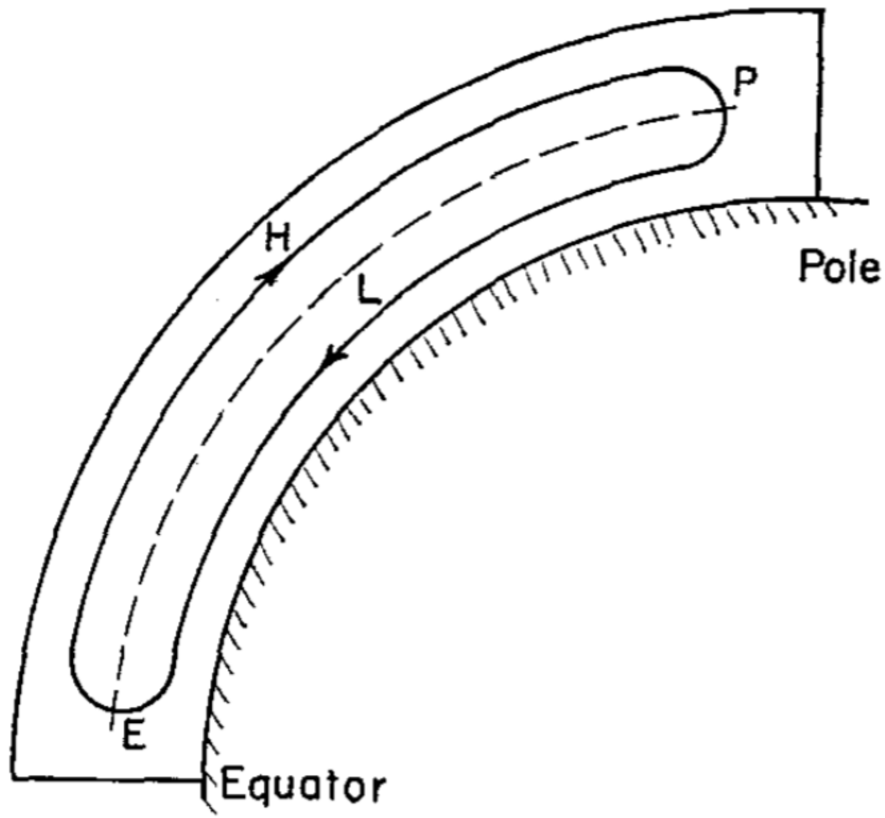

Gierasch (1975)

子午面循環による運動量の上方輸送

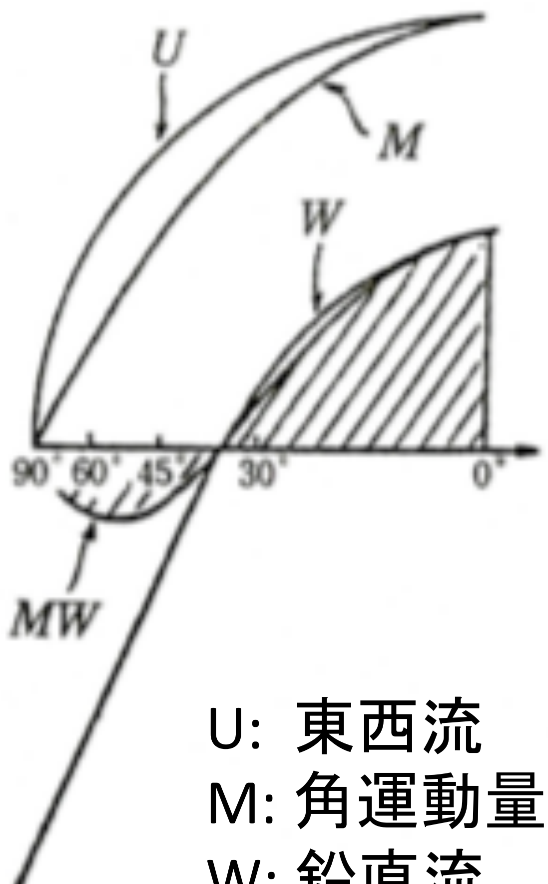

U: 東西流
M: 角運動量
W: 鉛直流

松田 (2000)

- W > 0 → MW > 0: 角運動量は低緯度で上層に輸送される。
- W < 0 → MW < 0: 角運動量は高緯度で下層に輸送される。
- M が低緯度でより大きければ <u>MW</u> > 0 → 正味の角運動量が上層に輸送される。
- Gierasch (1975) は無限大の水平渦粘性を仮定

Rossow and Williams (1979)

水平渦粘性の検証

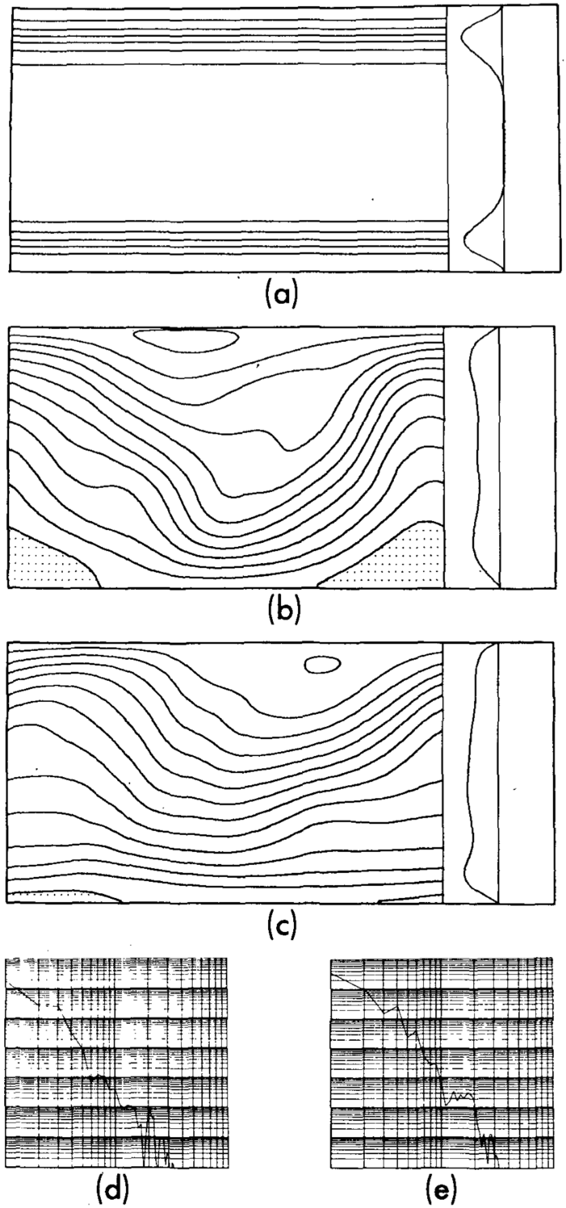

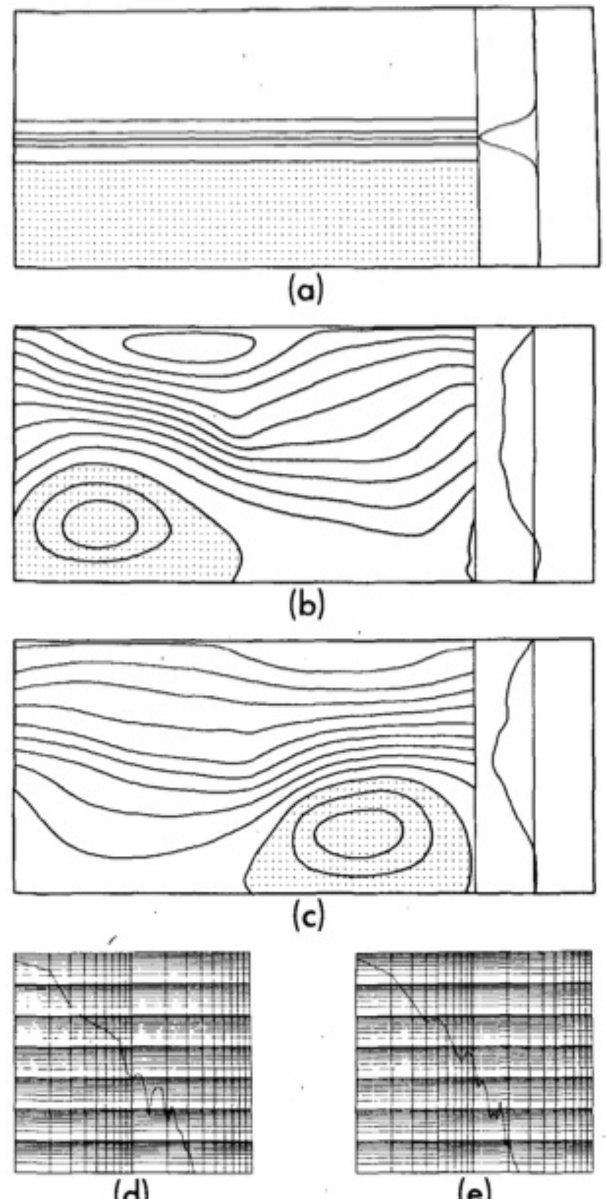

どちらも
軸対象な
強制を与
えた場合

Classification of types of planetary atmospheric circulation with finite v_H

--> large heating

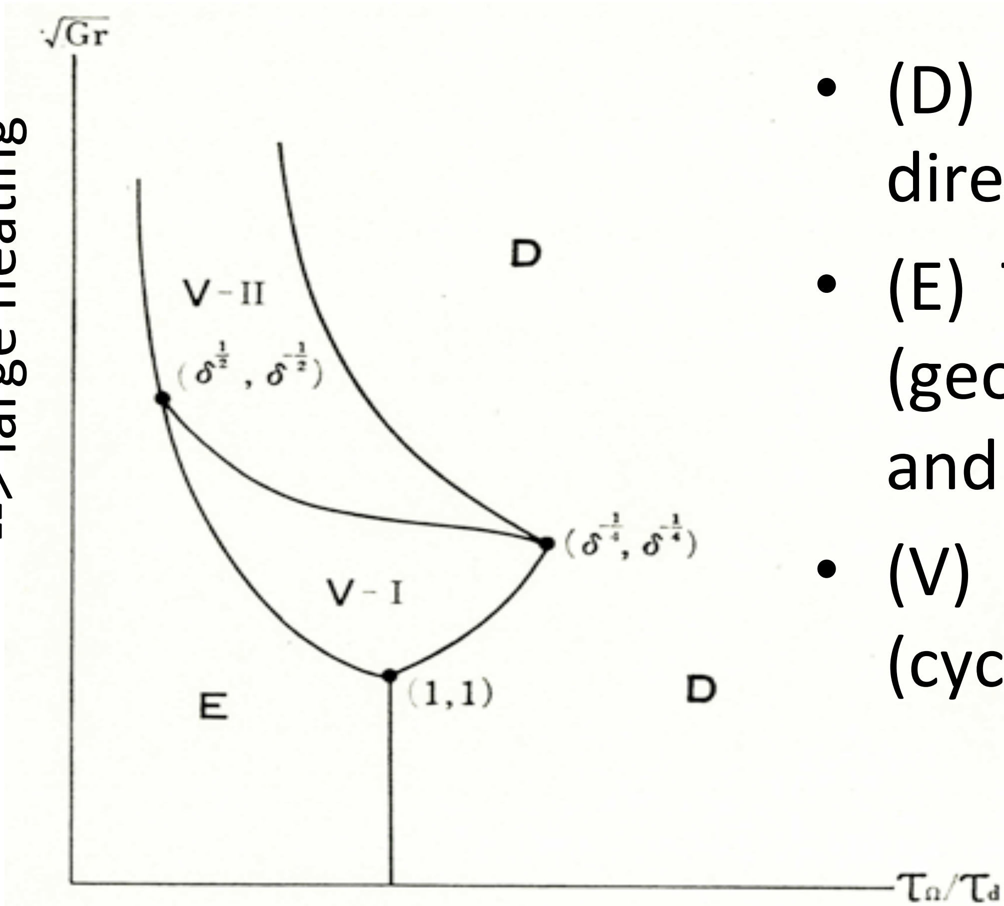

--> slow planetary rotation

- (D) Predominance of direct circulation
- (E) Thermal wind balance (geostophic) as in Earth and Mars
- (V) Thermal wind balance (cyclostrophic) as in Venus

Matsuda (1980)

水平渦粘性と子午面循環

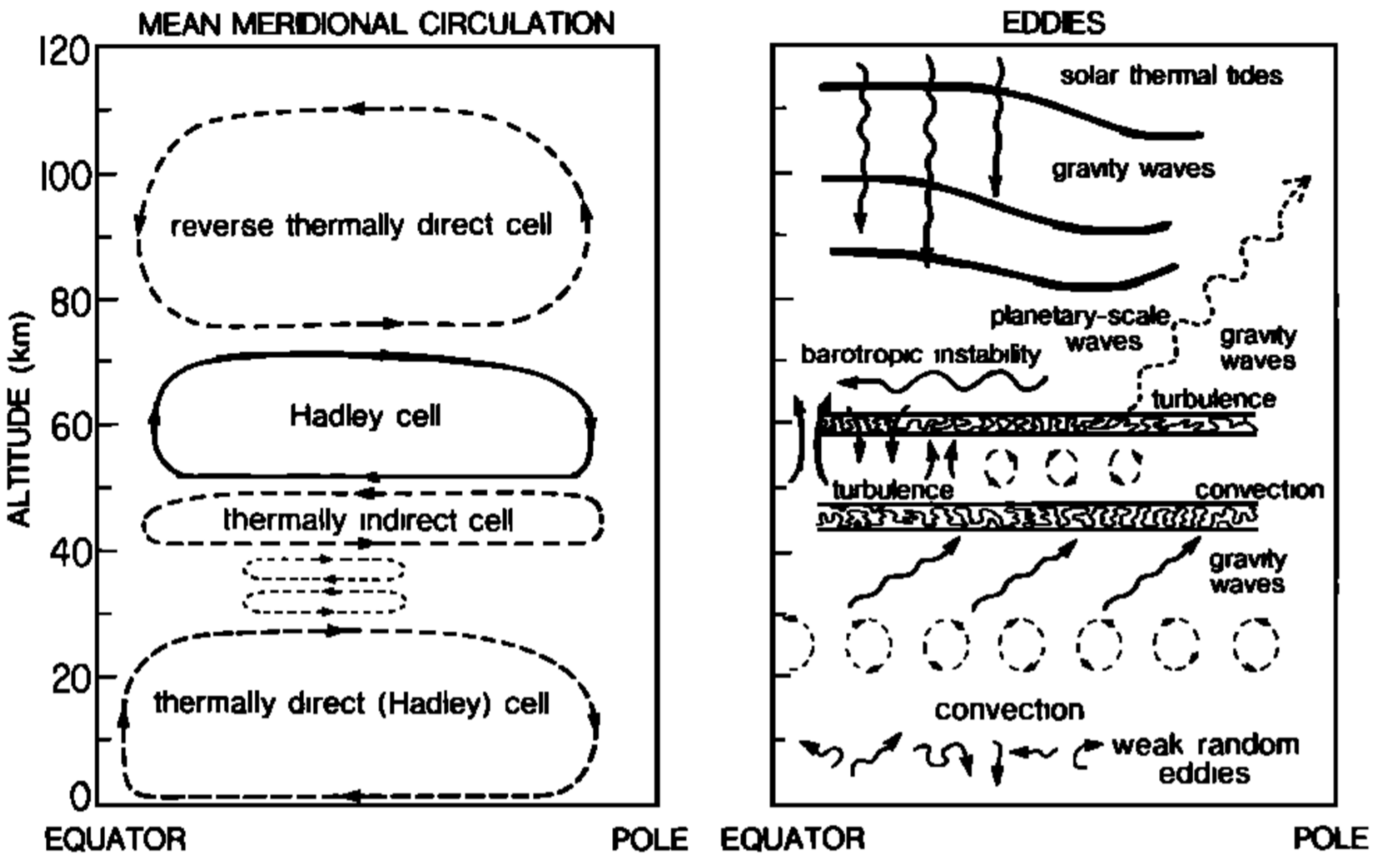

Schubert et al. (1980)

GCMによる子午面循環メカニズムの検証

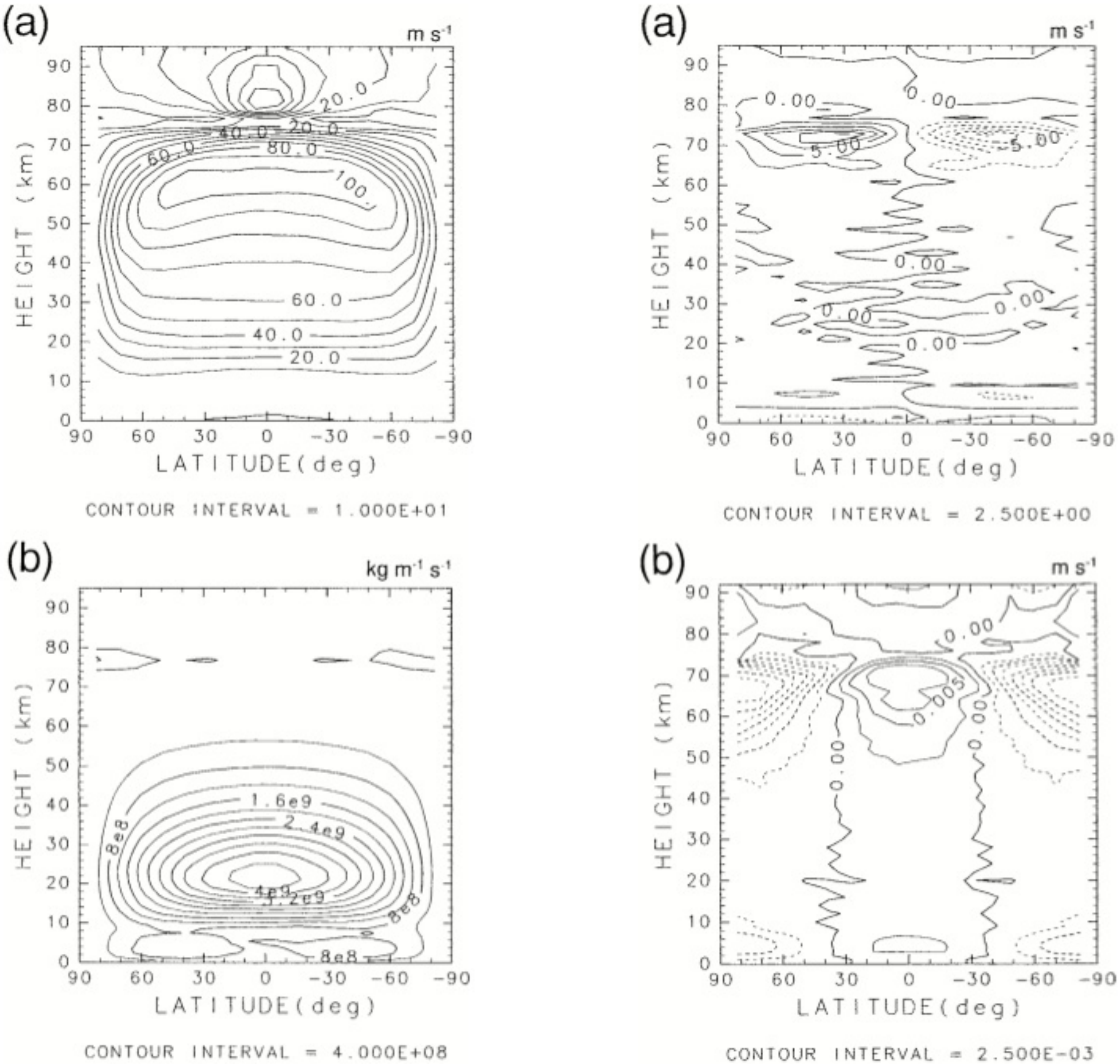

Yamamoto and Takahashi (2003b)

水平運動量輸送

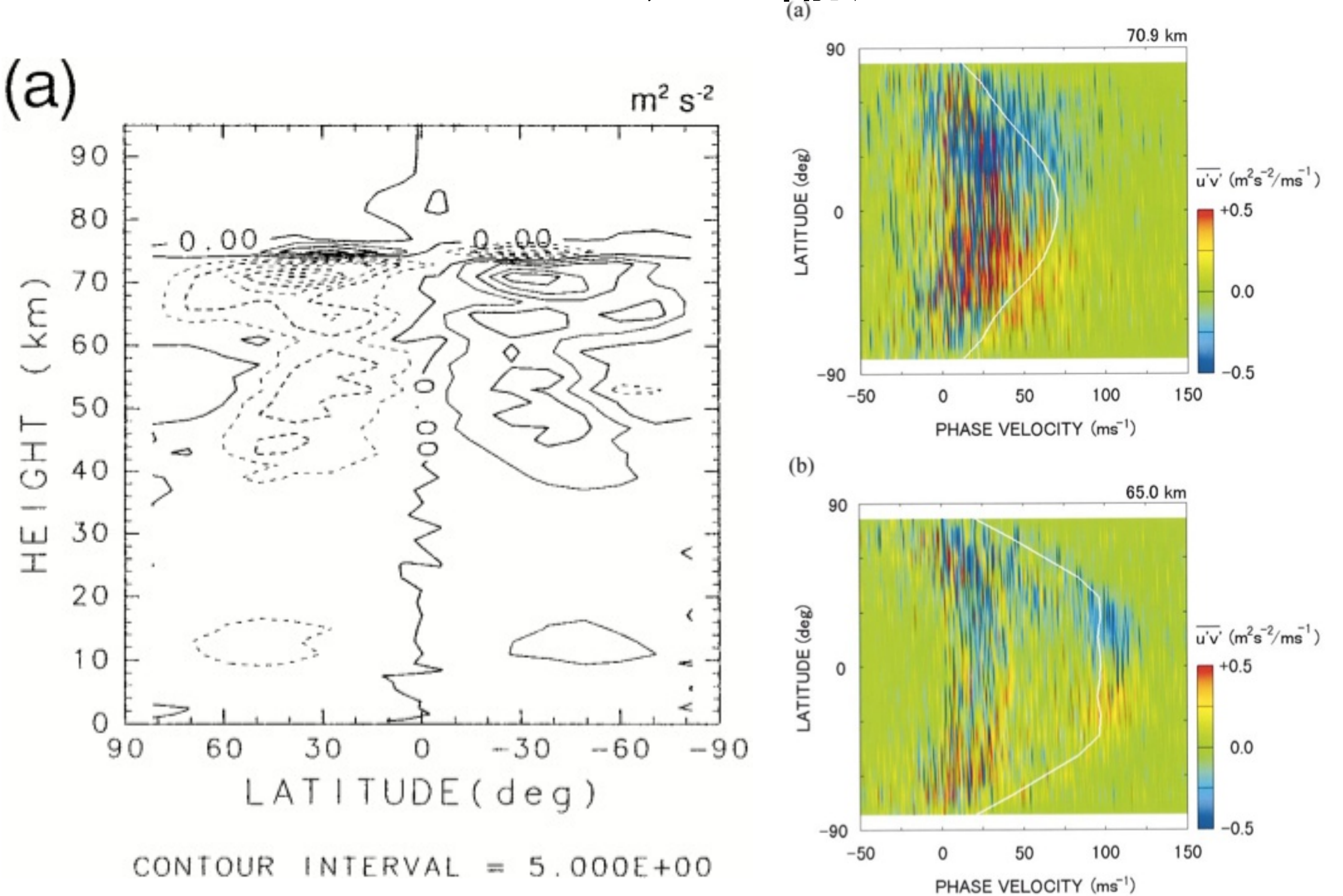

Yamamoto and Takahashi (2003b)

ニュートン冷却による強制

$$\frac{\partial T}{\partial t} = \cdots - k_{\mathrm{T}}\left[T - T_{\mathrm{eq}}(\phi, \eta)\right] \qquad (k_T = 1/25\ \mathrm{day}^{-1})$$

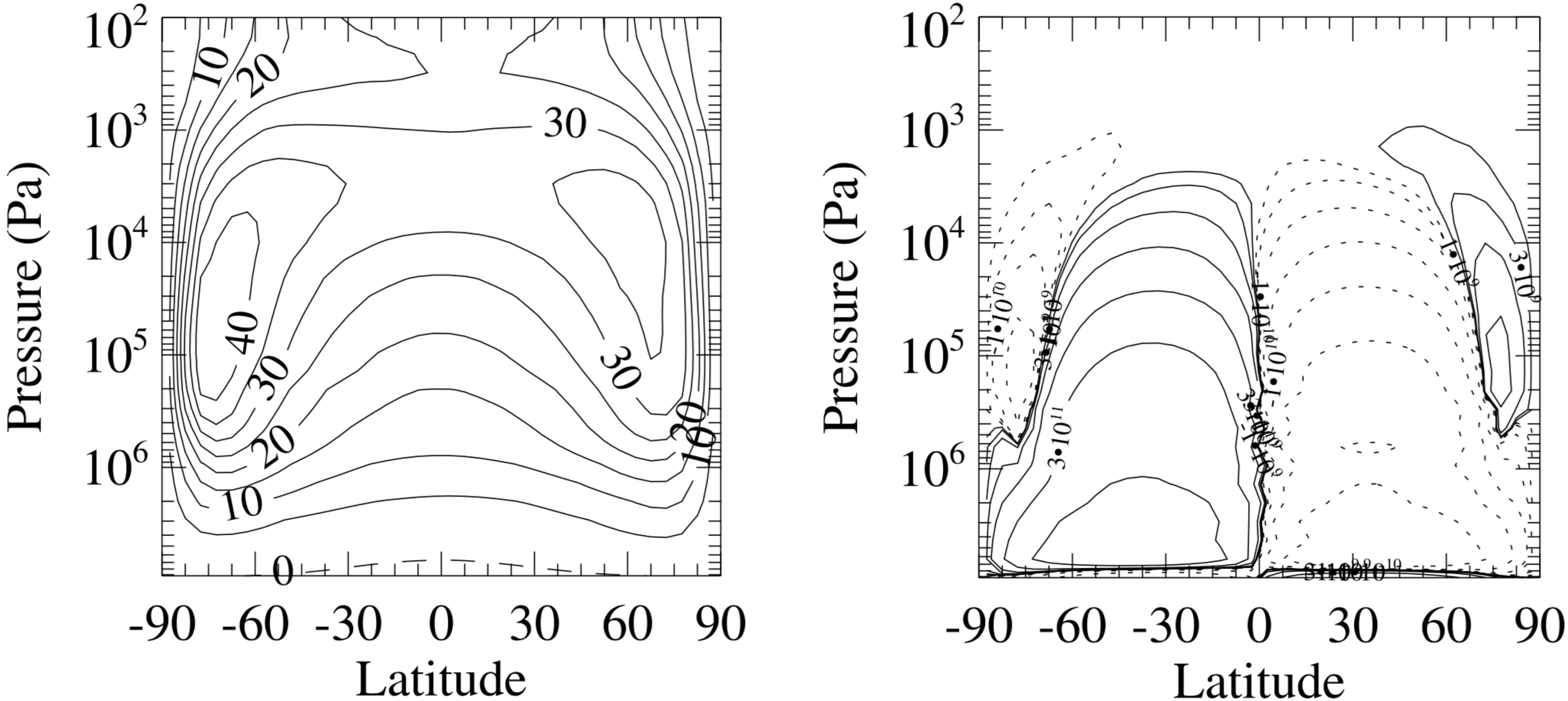

Lee et al. (2007)

加熱強度に対する依存性

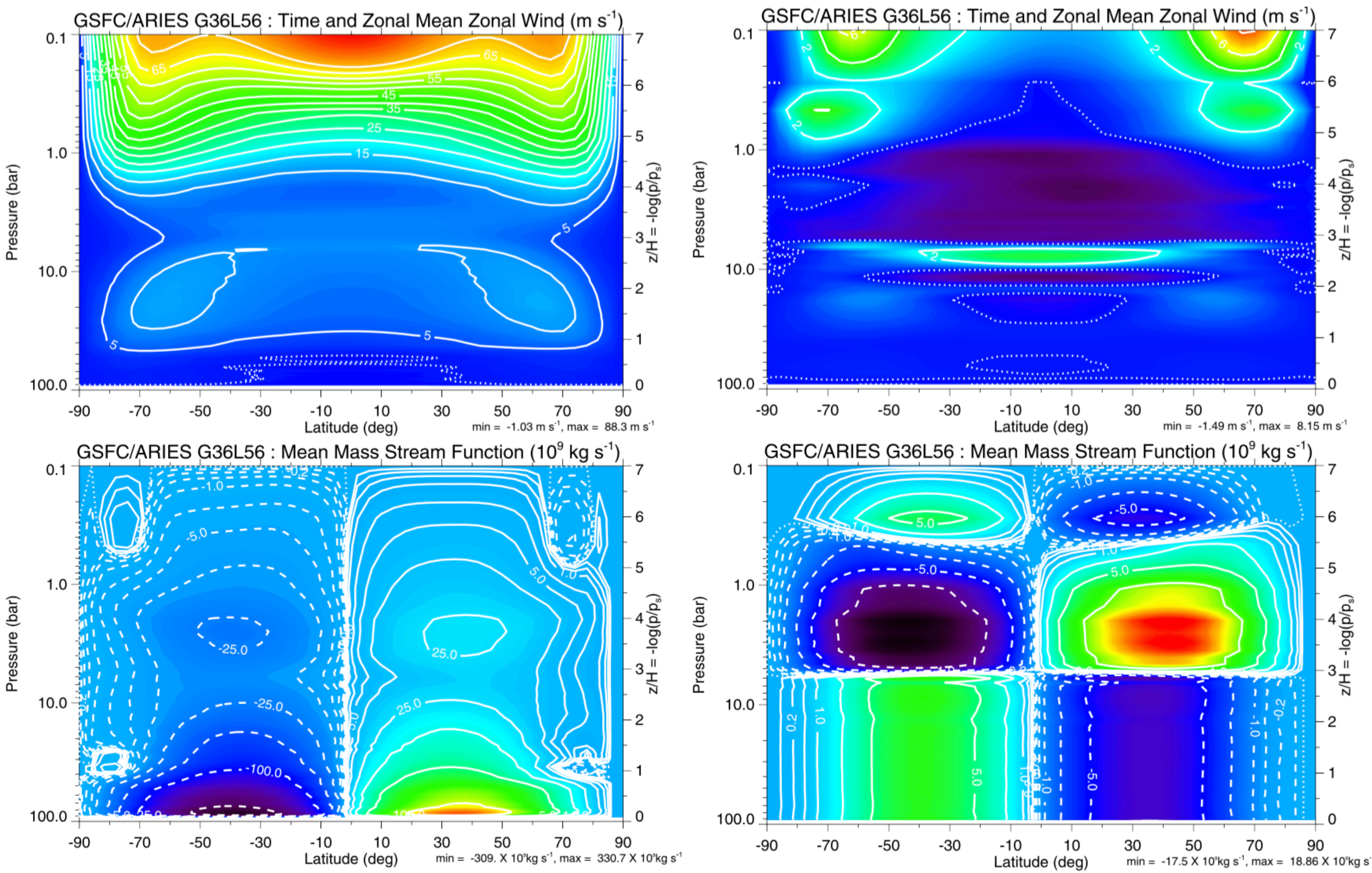

Hollingsworth et al. (2007)

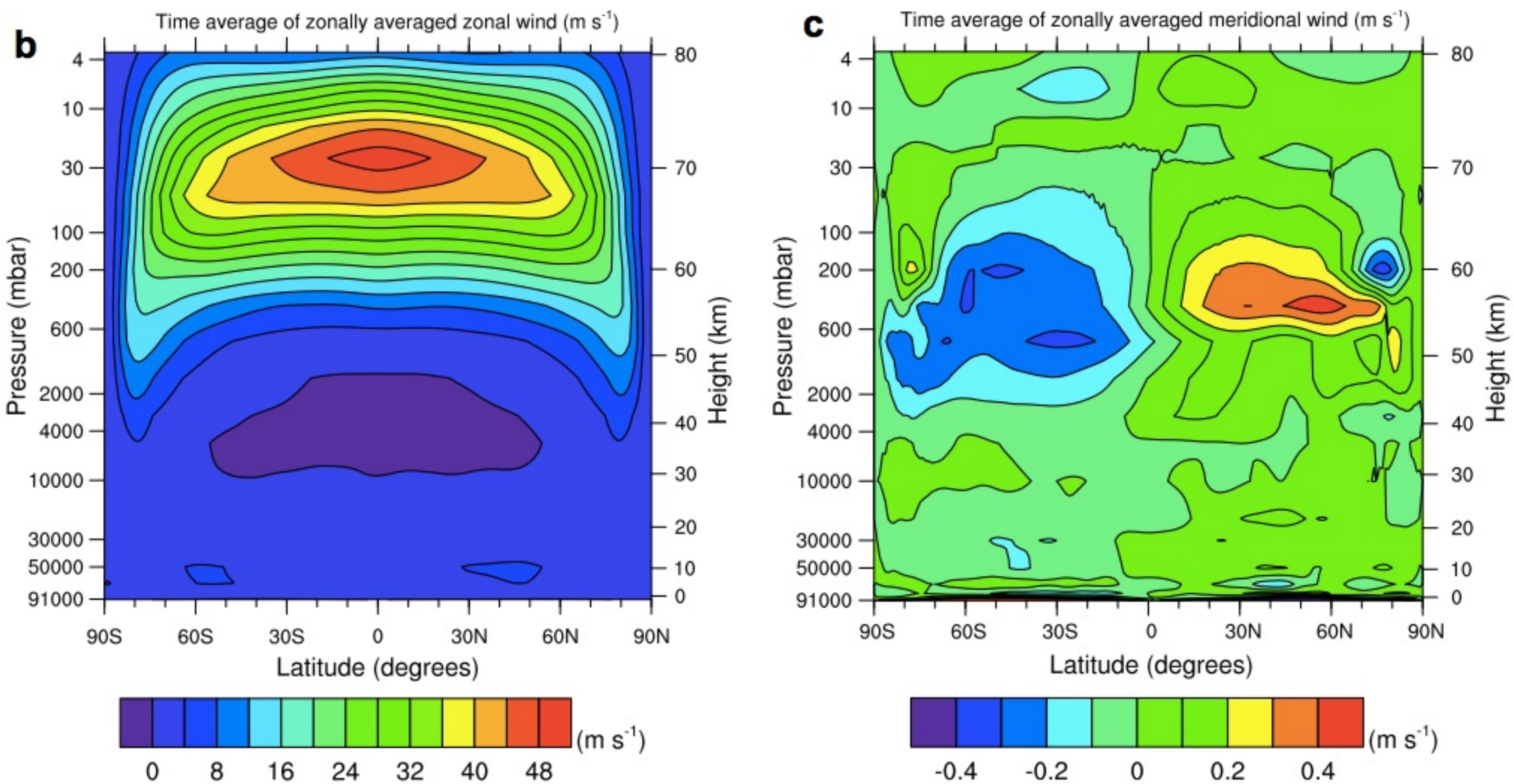

Parish et al. (2011)

10年スケールの変動

U

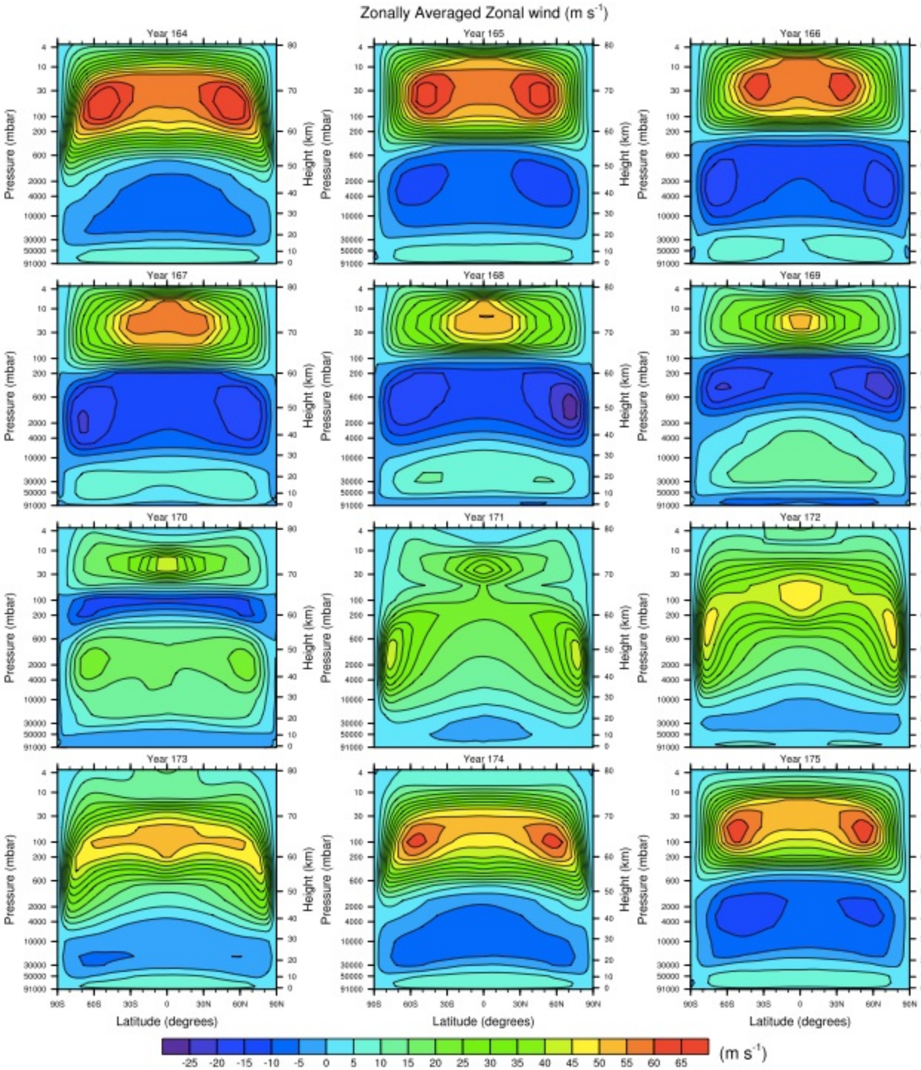

Fig. 3. Changes in zonally averaged zonal wind over the time interval 164–175 years.

V

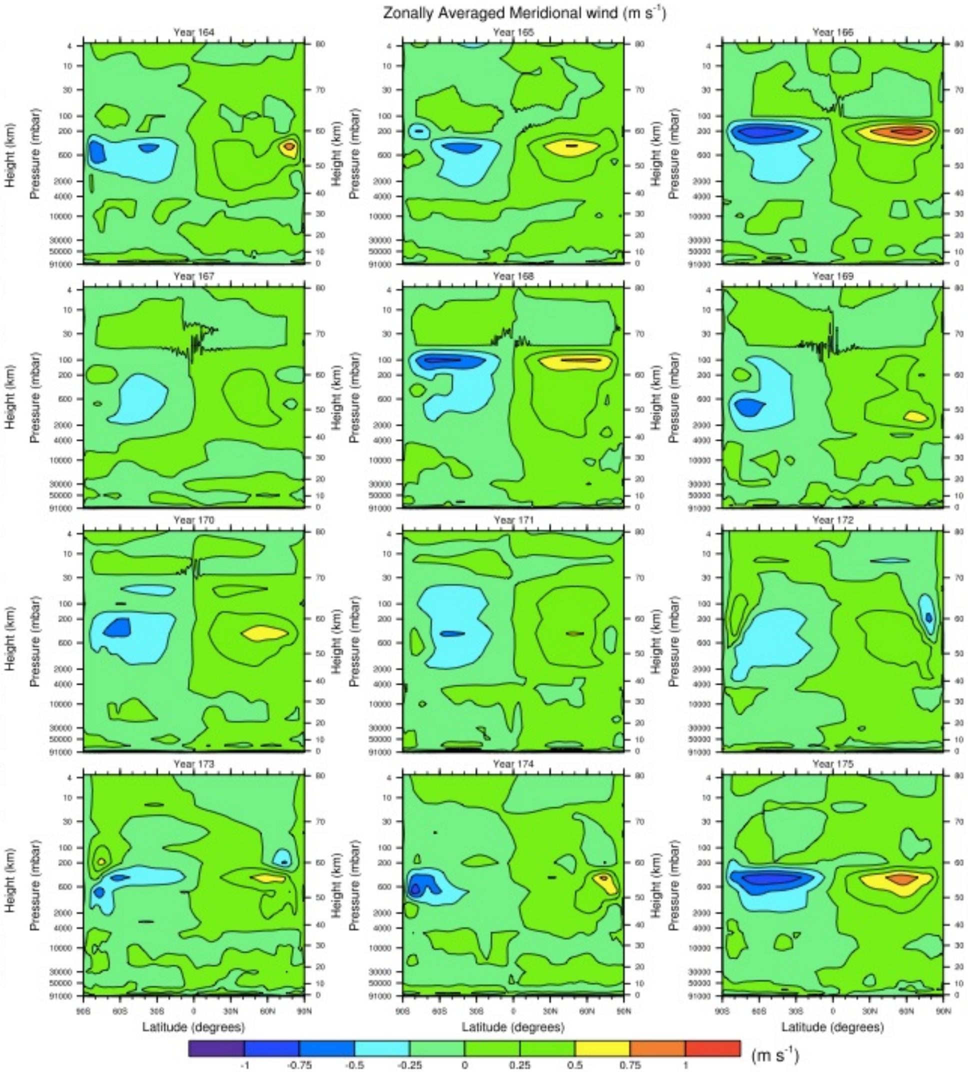

Fig. 4. Changes in zonally averaged meridional wind over the time interval 164–175 years.

Parish et al. (2011)

Numerical simulation of the MMC Williams (1988)

y-z distributions of streamfunction

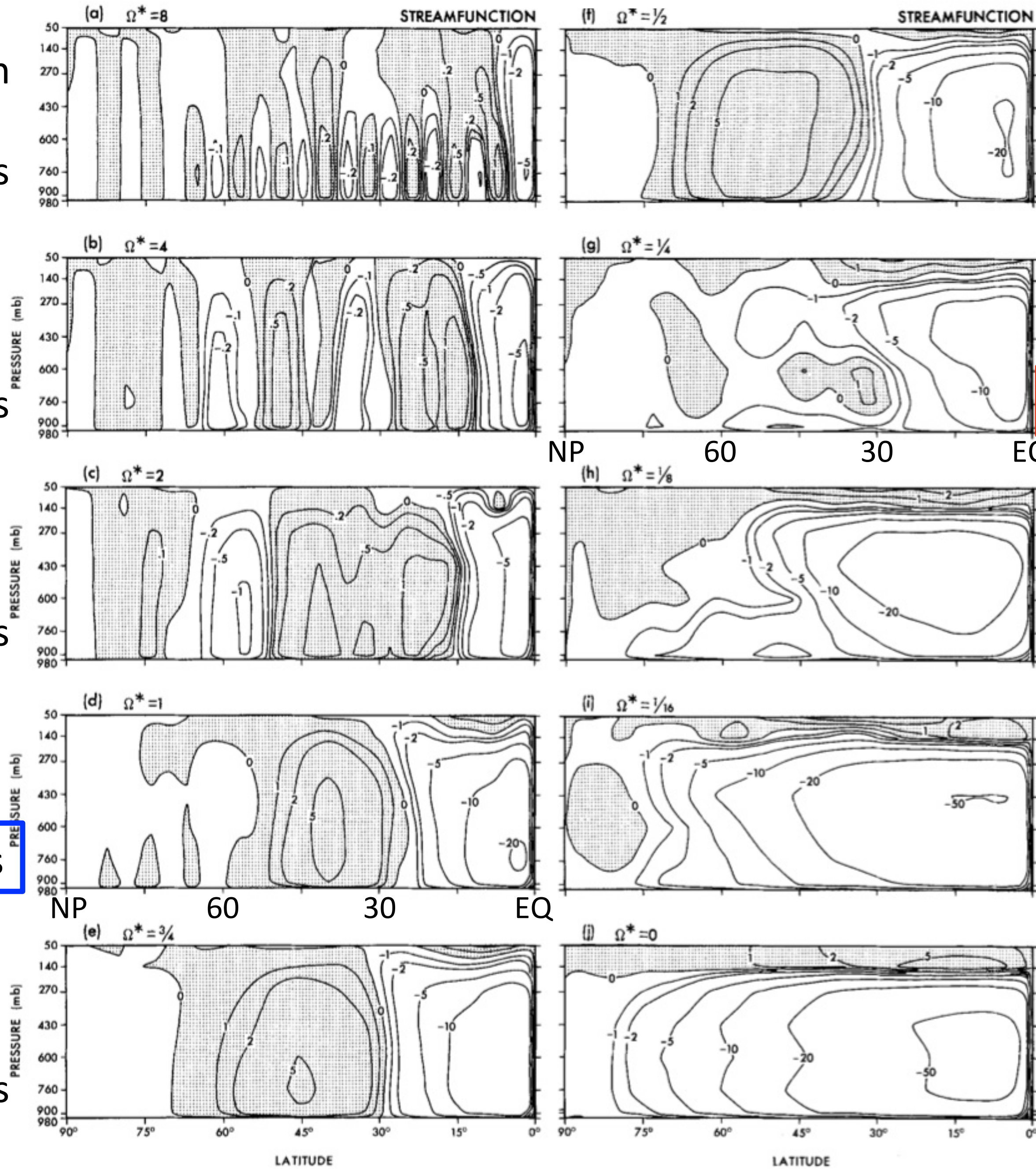

Rotation period: 1/8 days

1/4 days

1/2 days

1.0 days

4/3 days

2 days

4 days

8 days

16 days

No rotation

Fig. 3. Meridional distribution of the mean stream function for the MOIST model with $\Omega^* = 0$–8. Units: 10^{13} g s^{-1}

多重平衡状態

- Matsuda (1980, 1982)
- Kido and Wakata (2008, 2009)
- Yamamoto et al. (2009)

金星大気大循環の多重平衡状態

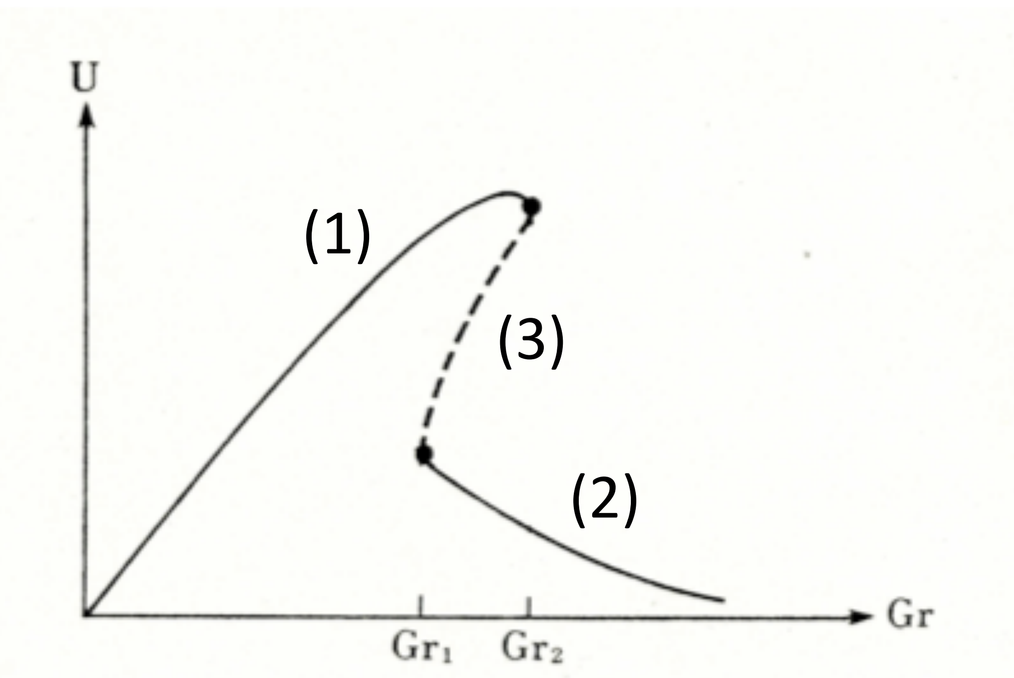

—→太陽加熱大

Matsuda (1982)

(1) 速い東西流をもつ安定定常解（スーパーローテーション）
(2) 夜昼間対流をもつ安定定常解（直接循環）
(3) 不安定定常解

(B) Multiple equilibirium states (circulation with superrotation and direct circulation)

- Kido reproduces multiple equilibria predicted by Matsuda in his GCM (Kido and Wakata(2008,09)).

Case I starts with motionless initial condition

Case II starts with fast zonal winds

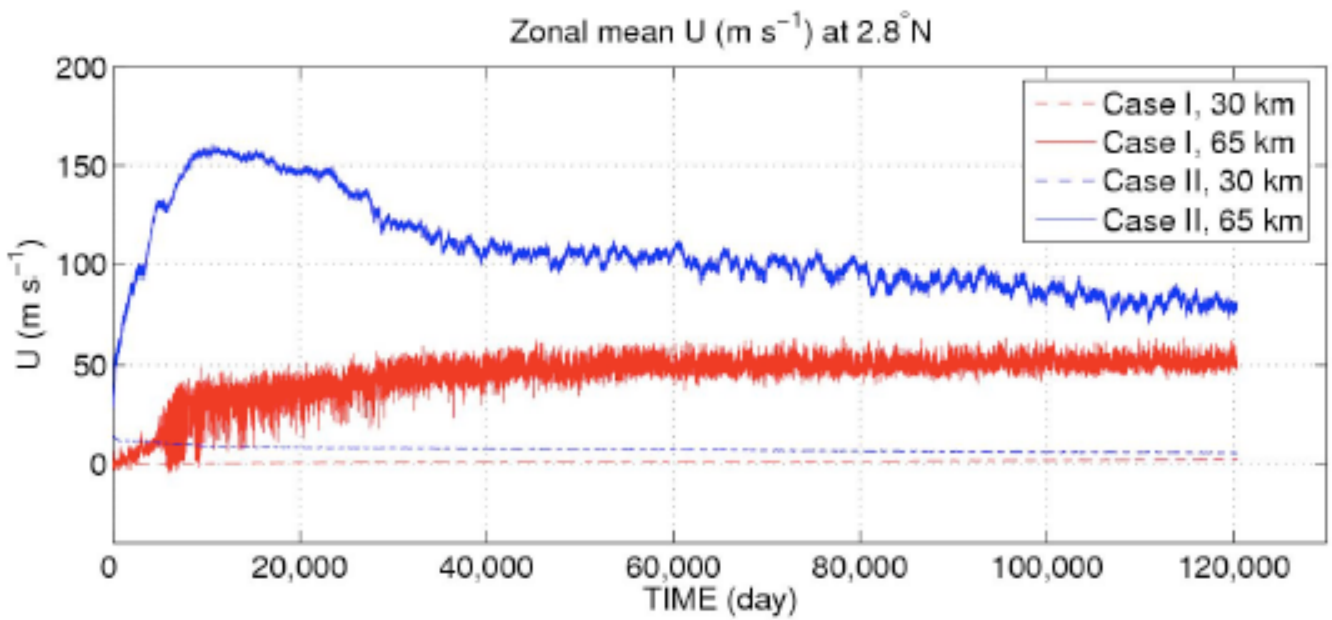

Kido and Wakata (2009)

Two different distributions of zonal wind under the same condition in Kido and Wakata (2009)

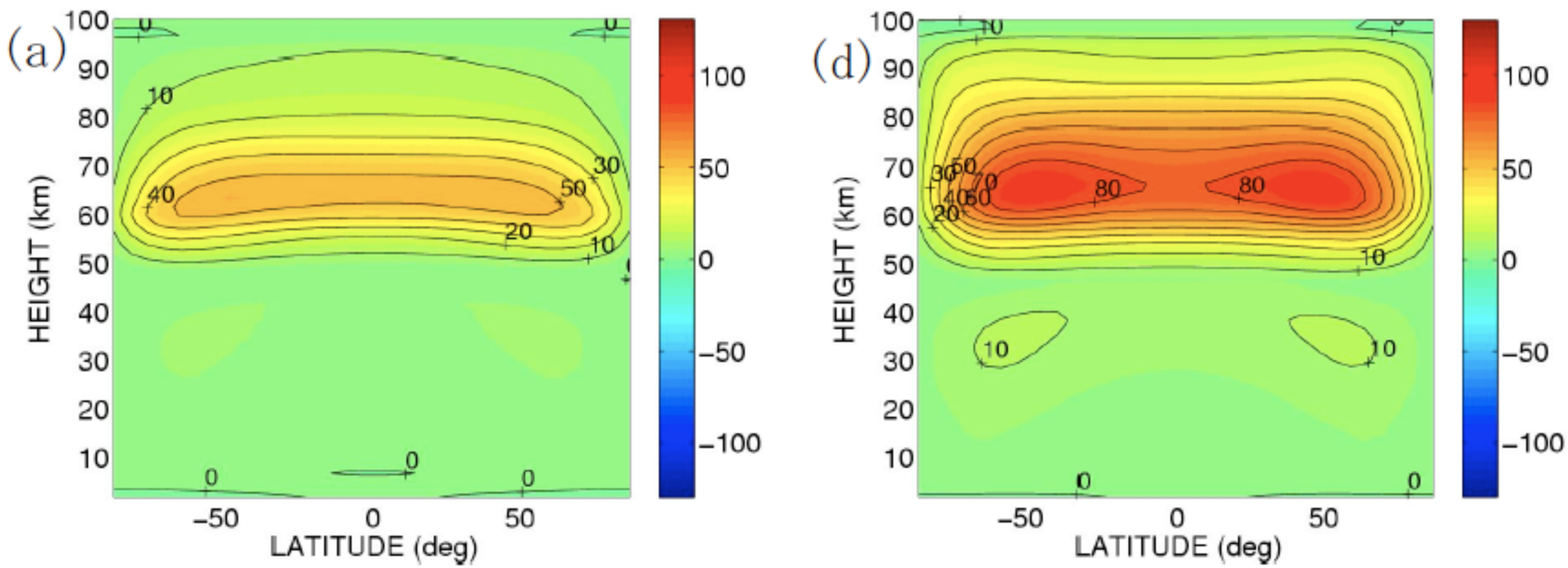

case I   case II

波に関する研究

- Covey and Schubert (1982)
- Young et al. (1984)
- Matsuda (1984)
- Young et al. (1987, 1994)
- Smith et al. (1992, 1993)
- Yamamoto and Tanaka (1997)
- Yamamoto (2001)
- Yamamoto (2003)
- Iga and Matsuda (2005)
- Takagi and Matsuda (2005b, 2006b)
- Kouyama et al. (2015)
- Yamamoto and Takahashi (2012, 2015)
- Ando et al. (2016)
- Takagi et al. (in prep)

下端（下層）での波強制に対する応答

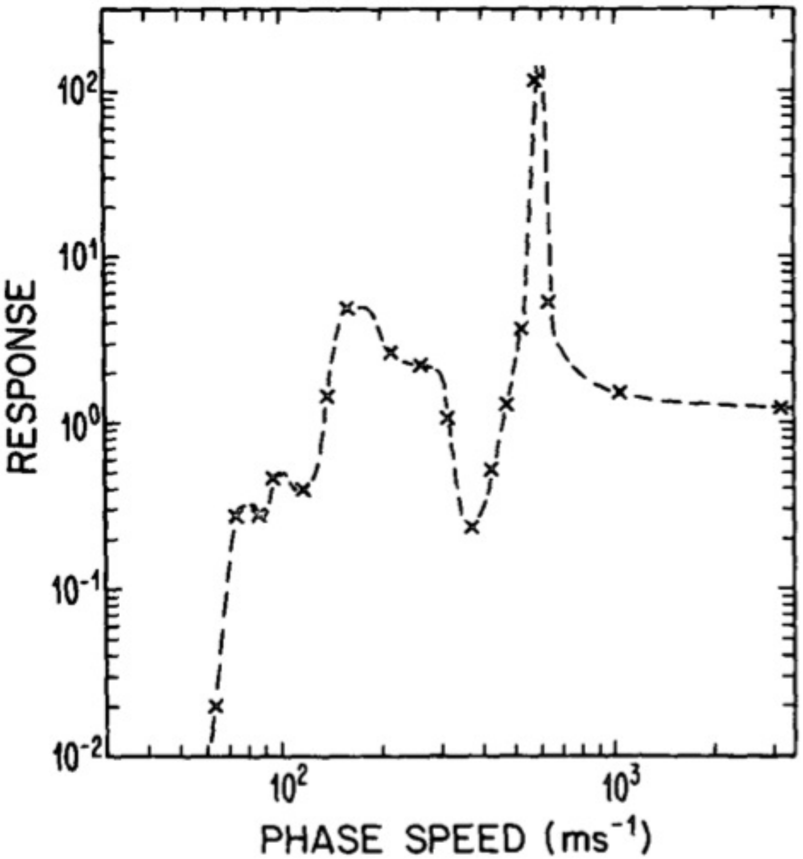

FIG. 4. Atmospheric response versus westward equatorial phase speed relative to the surface, obtained for the Venus case. The individual points are the results of the Lindzen-Kuo integration with $N = 3$ even Legendre functions, $s = 1$ and $\sigma = 10^{-2}\Omega_0$. The domain $0 < z < 10$ was divided into 1000 subintervals for the integrations.

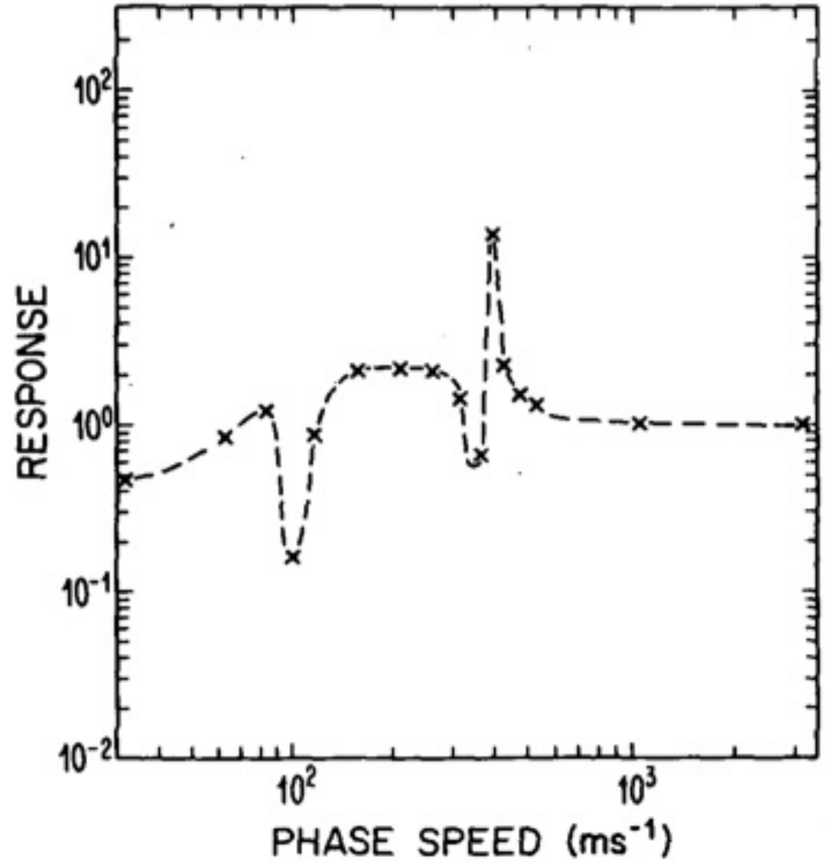

FIG. 6. As in Fig. 4, except that forcing is imposed at $z = 6.5$ and response measured over the interval $6.5 < z < 10$, as described in the text. $\Delta z = 0.01$ in the integrations.

Covey and Schubert (1982)

2つの波によるY字模様の形成

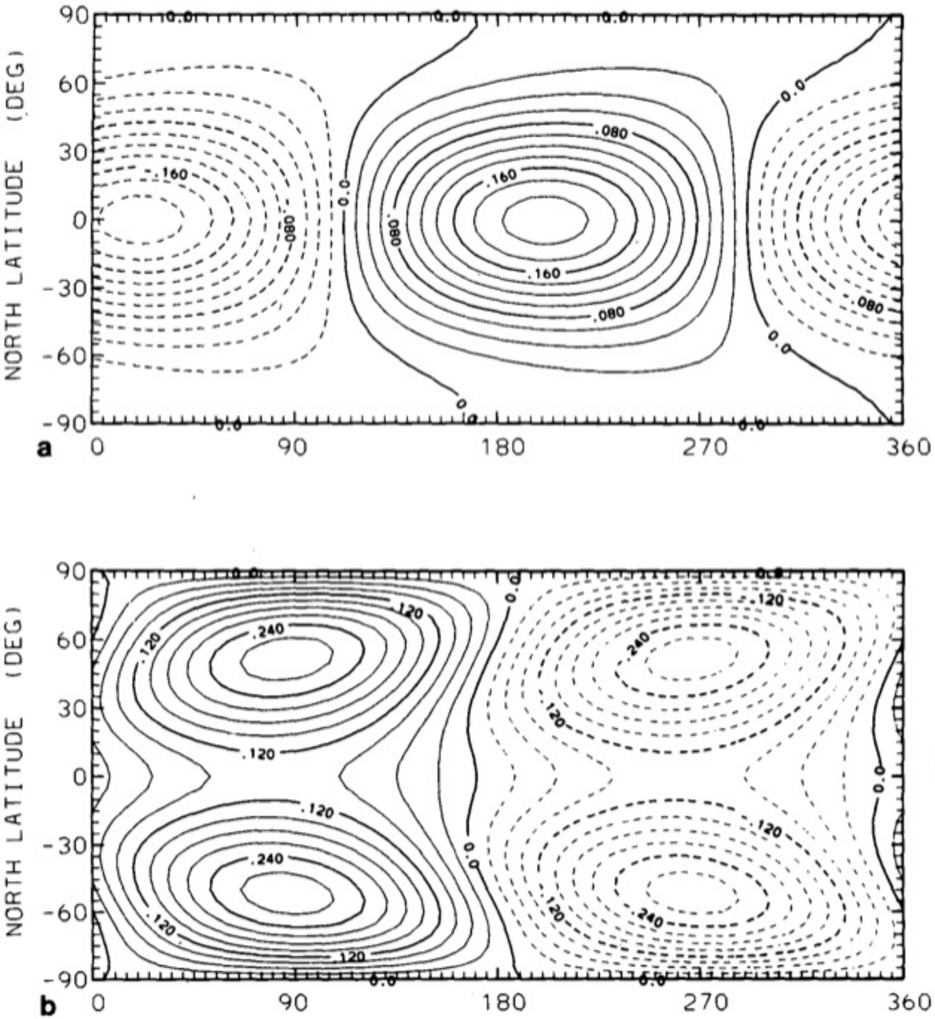

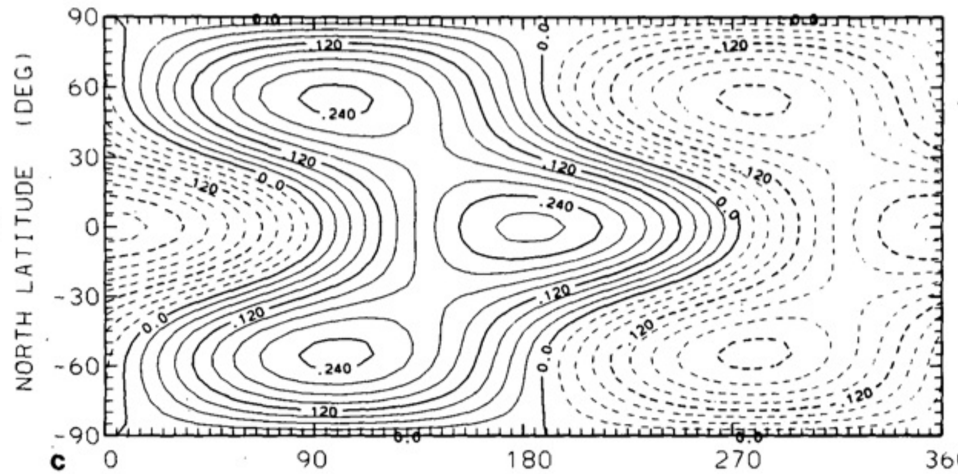

FIG. 7. Horizontal structure of wave amplitude at $z = 7.0$ for (a) the Rossby wave at $\omega = 0.8\Omega_0$, (b) the Kelvin wave at $\omega = 1.5\Omega_0$, and (c) the linear combination 1.5(a) + (b). The horizontal scale indicates east longitude (degrees).

時間とともにY字の方向が逆転する。

Covey and Schubert (1982)

CFH による波応答の強化

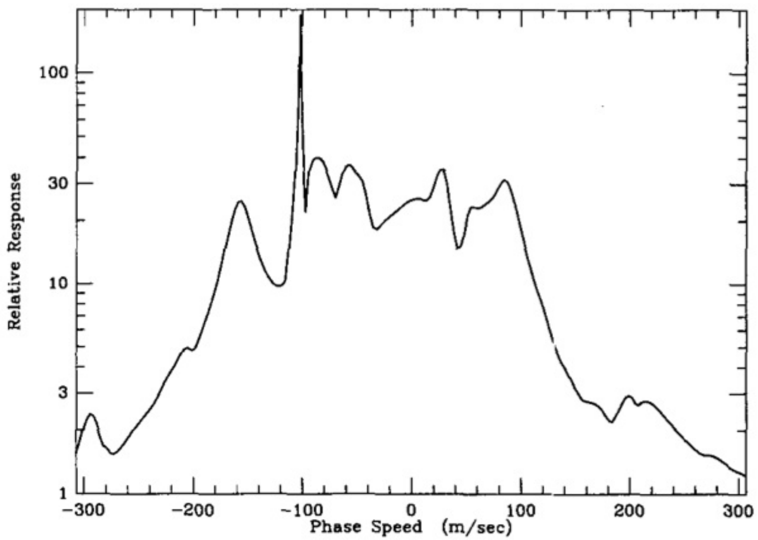

FIG. 7. Same as Fig. 5 except that a cloud feedback heating has been added with strength $\beta = \beta_{crit}$. The two spectra are nearly identical except in the region around the most unstable wave mode at −102 m s^{-1}.

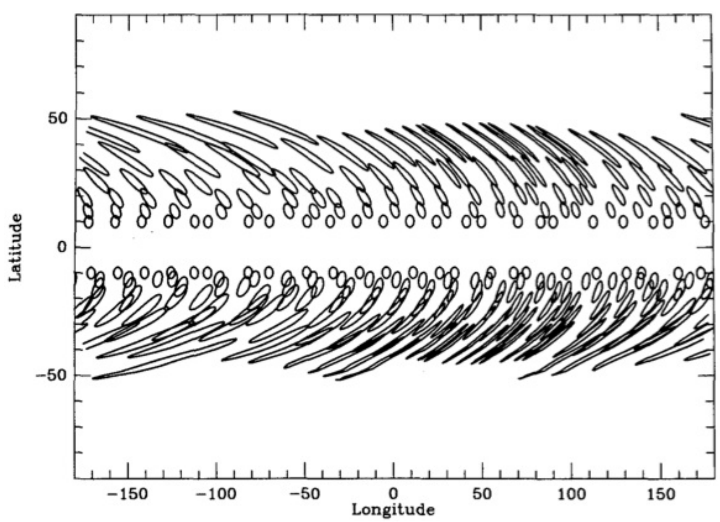

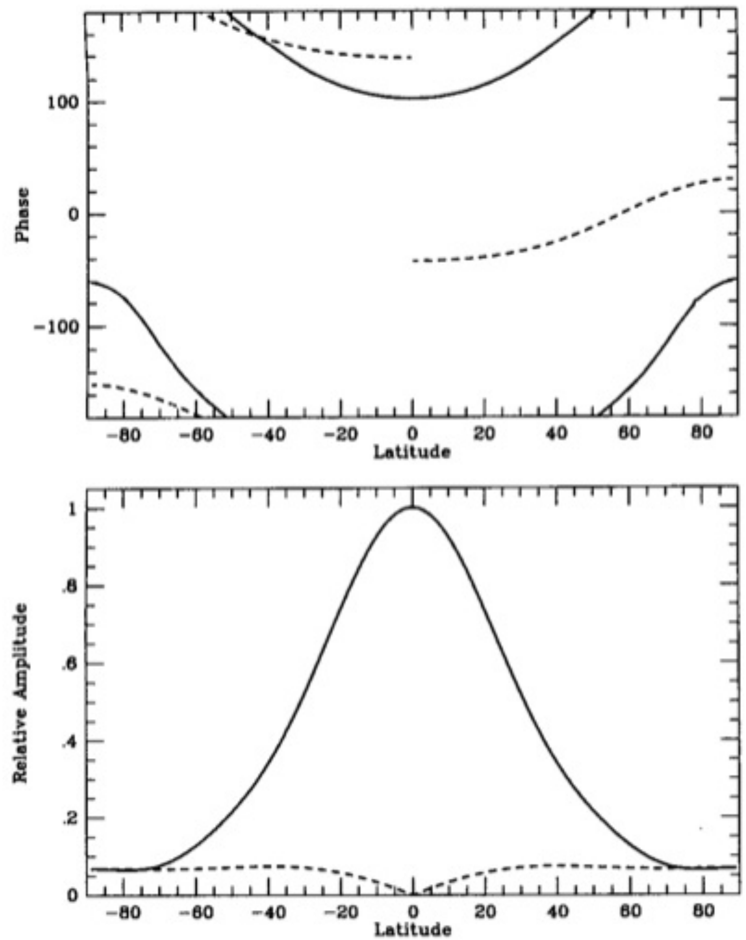

FIG. 9. Horizontal structure of the wave mode shown in Fig. 8. Again the solid line shows horizontal velocity and phase, and the dashed line shows meridional velocity and phase. The relative amplitudes between the zonal and meridional components are correct (there has been no multiplication of the meridional component), but the overall scaling is arbitrary. The horizontal structure has been taken at a pressure scale height of 6.5 (63 km). The phase of the waves has the same meaning as in Fig. 8.

Smith et al. (1993)

Cloud Feedback Heating (CFH)

We have experimented with simple models of the cloud radiative transfer and find that the width of the affected layer is typically a few optical depths, which is a few kilometers (Knollenberg and Hunten 1980). Guided by these considerations, we introduce a perturbation heating profile that is proportional to the vertical displacement, with an amplitude set by the local radiative time constant:

$$Q_{\text{cloud}} = \beta f(z) \frac{T}{t_r} \frac{\delta z}{H}, \tag{21}$$

where β is an amplitude parameter, $f(z)$ is a shape profile (maximum amplitude unity, positive below the base and negative above the base), T is the full temperature, t_r is the radiative time constant based on a length of a scale height, δz is the vertical displacement,

Smith et al. (1993)

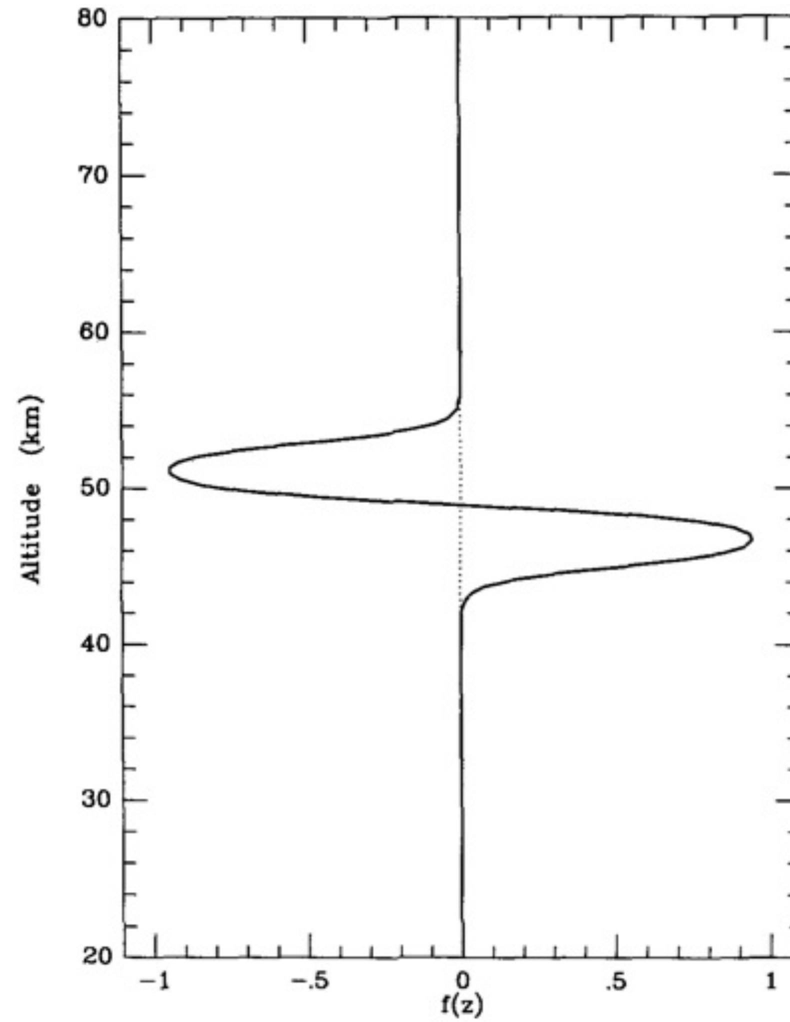

FIG. 4. Vertical profile of $f(z)$ function for the case with cloud feedback heating.

波と子午面循環による超回転の維持

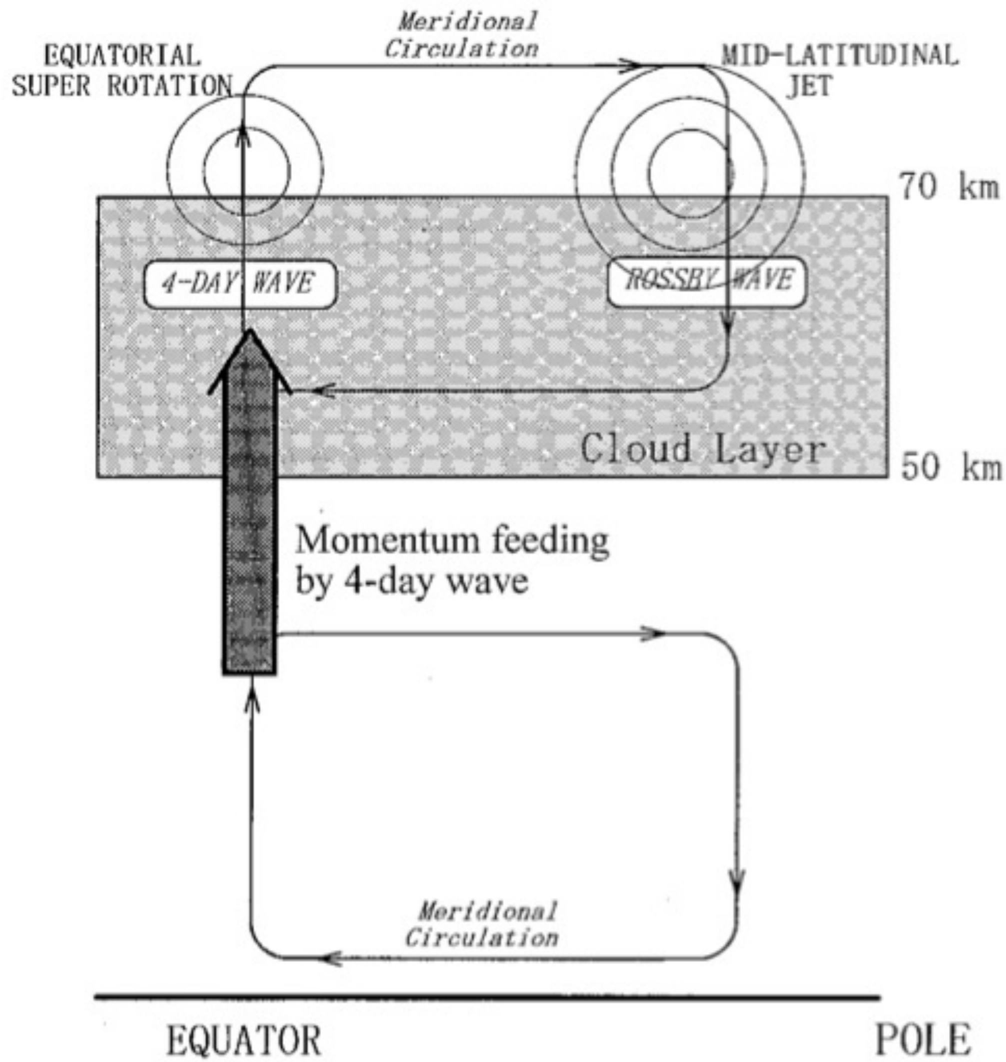

FIG. 1. Schematic illustration of a meridional section of the general circulation in the Venus atmosphere.

Yamamoto and Tanaka (1997)

下層から伝播する4日波による赤道加速

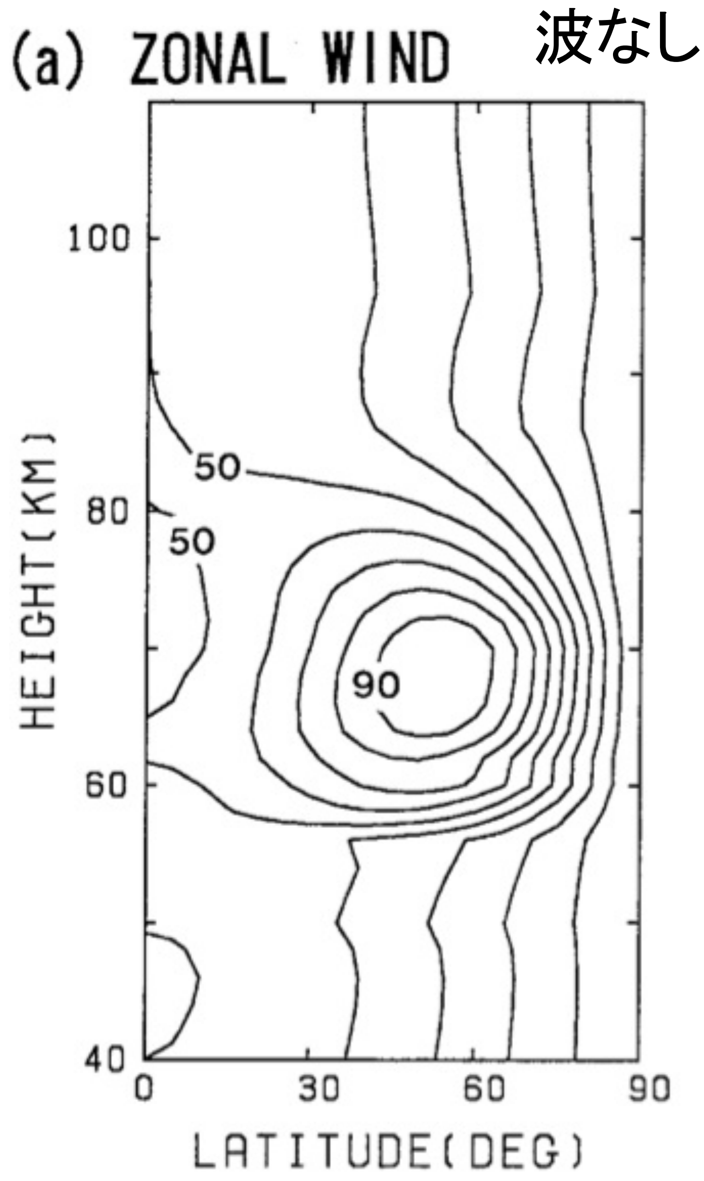

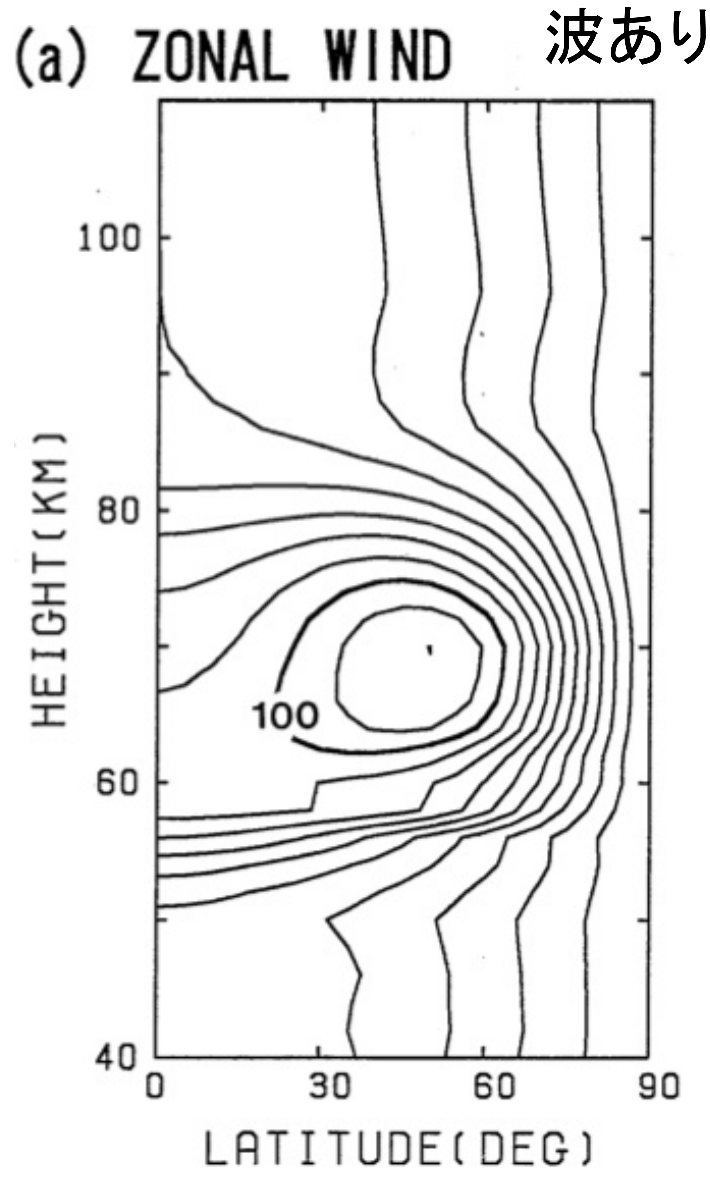

Yamamoto and Tanaka (1997)

4日波と5日波によるY字模様の形成

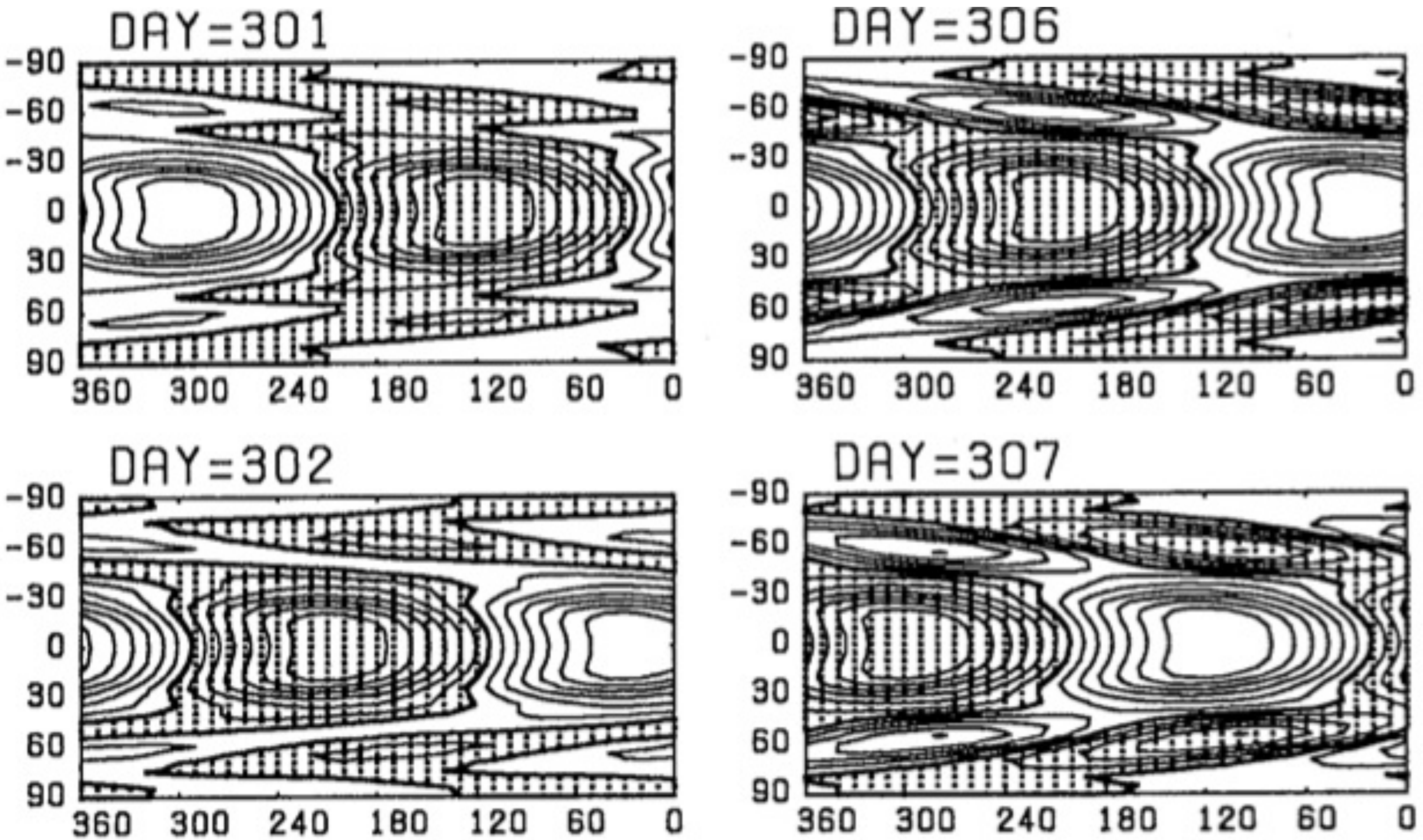

Yamamoto and Tanaka (1997)

下端での波強制に対する応答

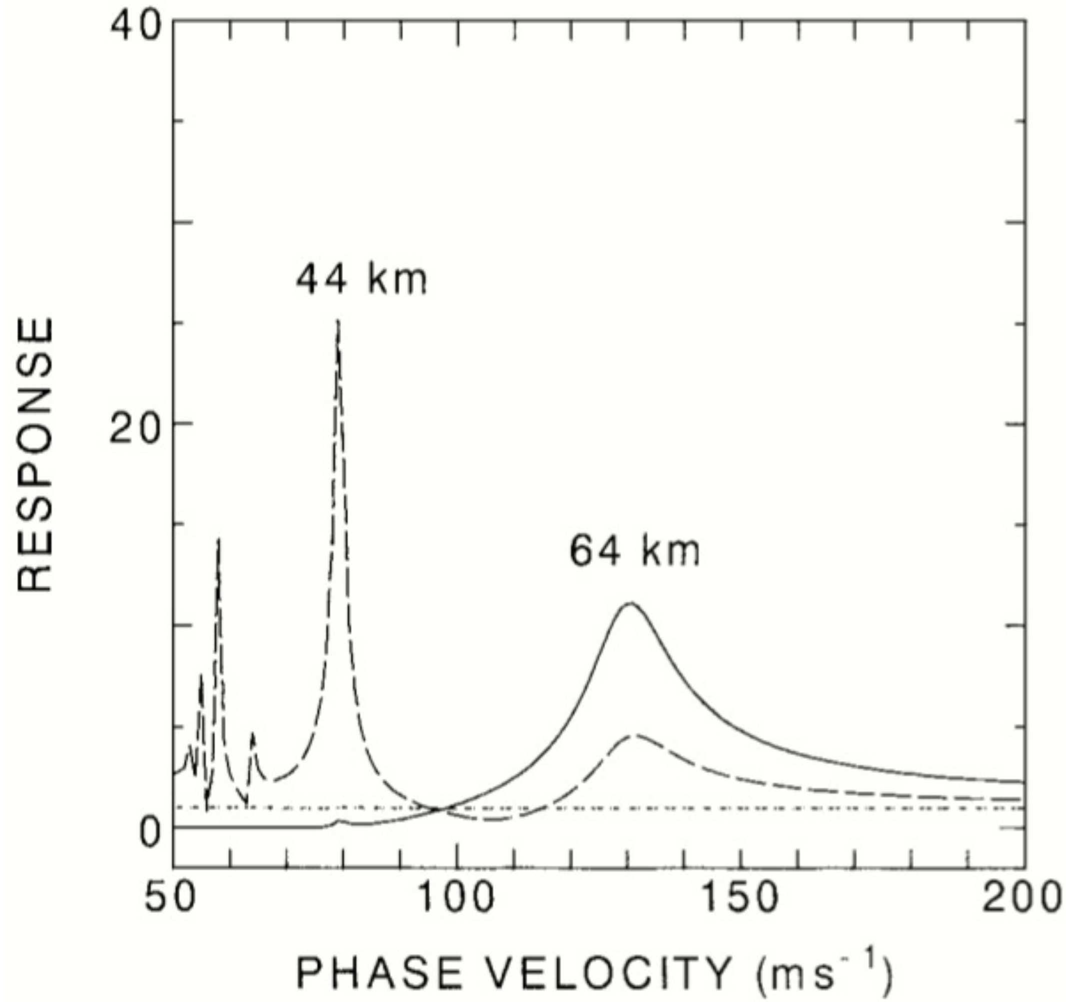

FIG. 3. Linear responses of the zonal wave 1 gravity waves to the bottom-boundary forcing. The responses at the 44-km (dashed curve) and 64-km (solid curve) altitudes represent the geopotentials divided by the bottom value at 0.25 km (dotted line).

Yamamoto (2001)

臨界高度付近での非線型効果

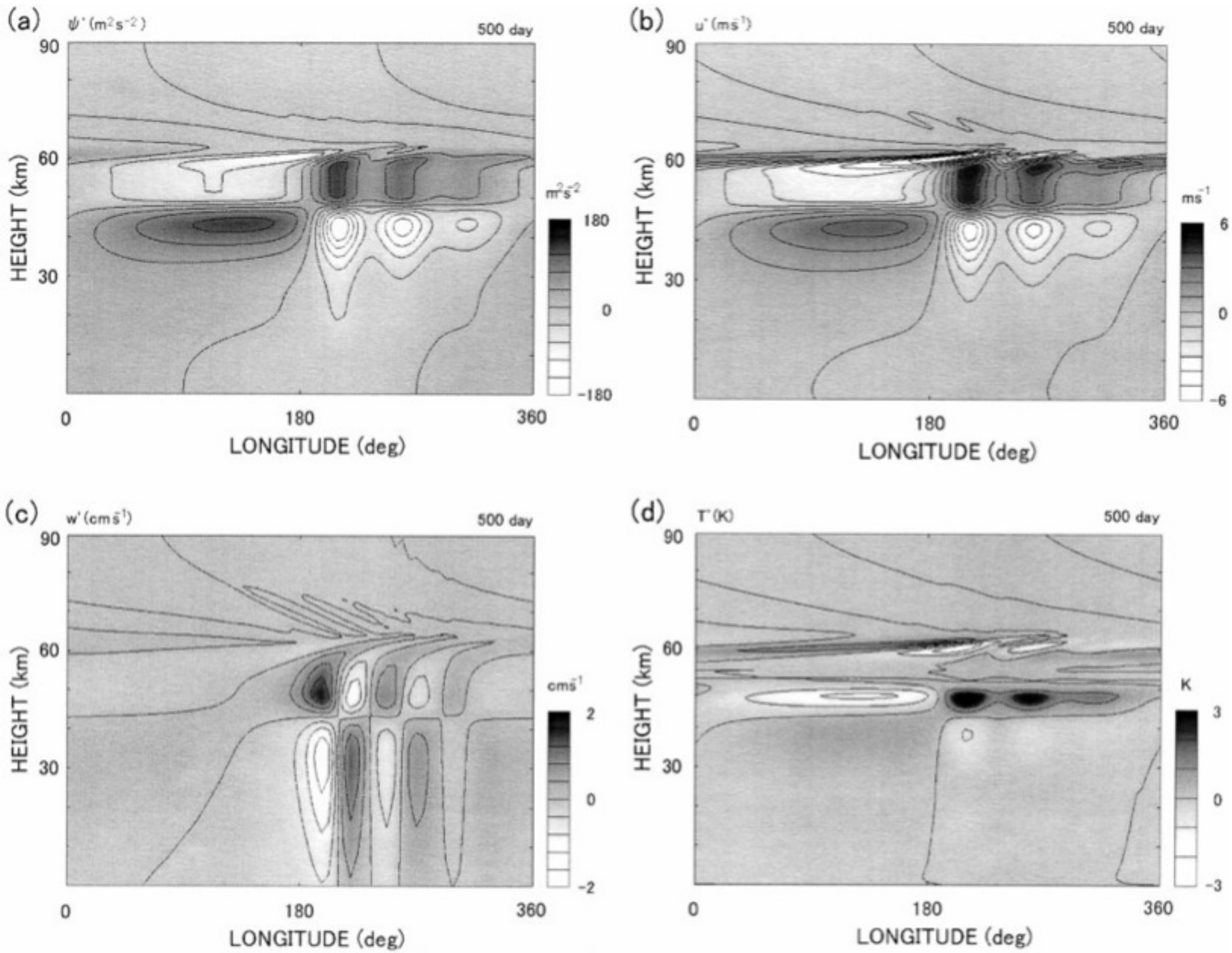

FIG. 6. As in Fig. 4, except for the case of $s = 1$, $c = 79$ m s^{-1}, and $h_{\text{bottom}} = 1$ m.

Yamamoto (2001)

CFH による対流からの重力波の強化

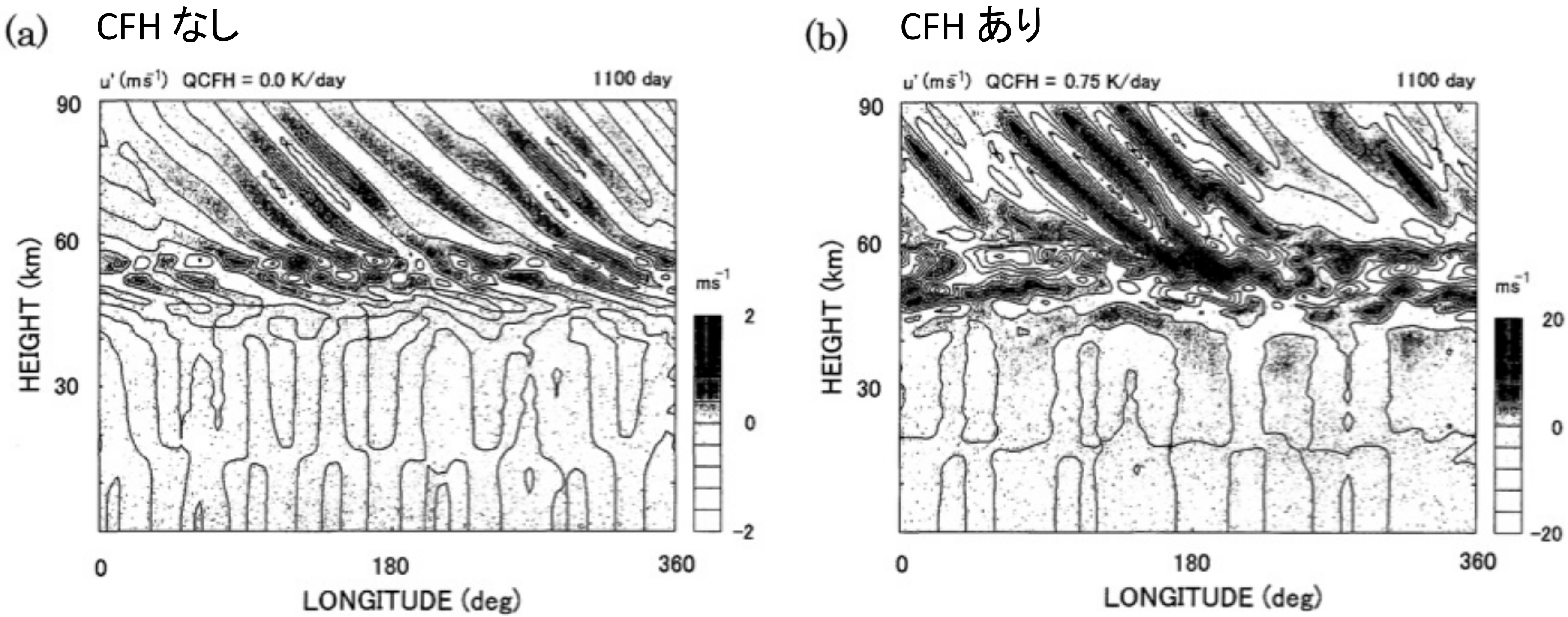

Yamamoto (2003)

球面浅水系の不安定モード

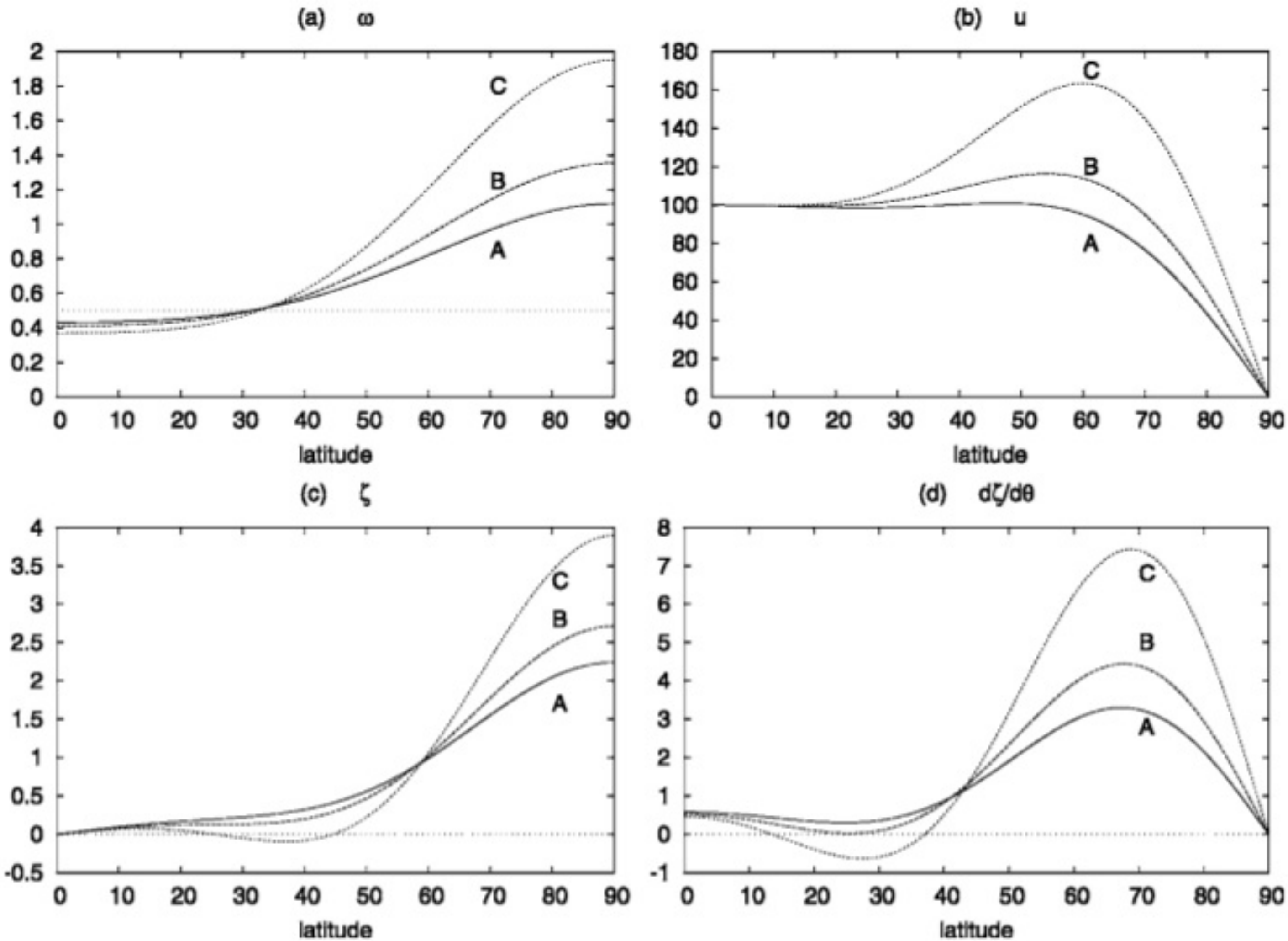

FIG. 2. Meridional distributions of the basic zonal wind (A–C) investigated in this study. (a) The nondimensionalized angular velocity of the basic winds observed from an inertial system (that from a rotating system is obtained by subtracting $\overline{\omega}$ by 0.5.), (b) velocity in an inertial system, dimensionalized with $\overline{u}$ = 100 m s^{-1} at the Venus cloud top on the equator in mind, (c) the nondimensionalized potential vorticity, and (d) the latitudinal gradient of potential vorticity.

Iga and Matsuda (2005)

不安定化した Rossby-Kelvin モード

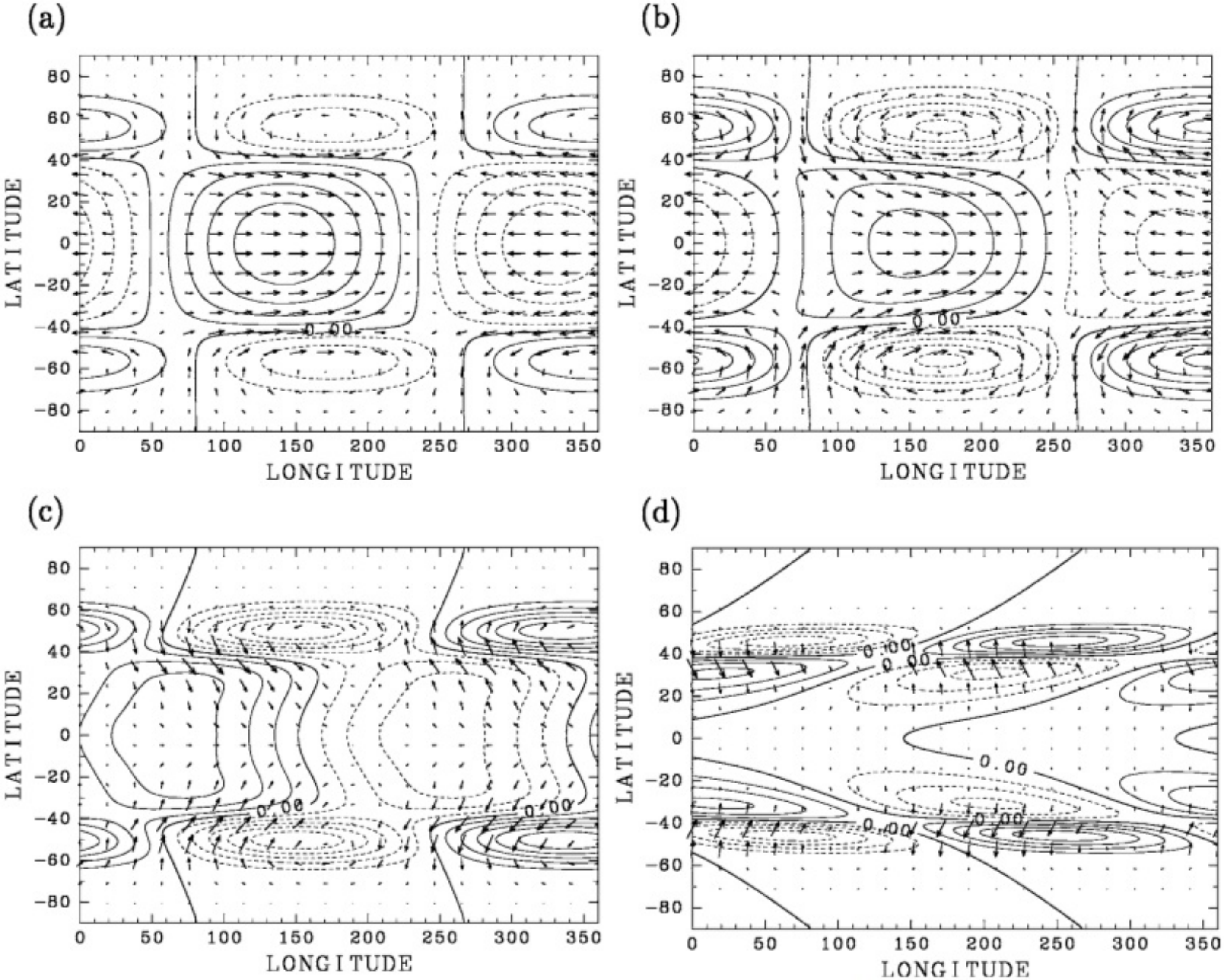

FIG. 16. As in Fig. 5c but for wind profile C: the modes designated by (a) a and (b) b with $\epsilon^{-0.5}$ = 0.2355 in Fig. 15a, and the modes designated by c with (c) $\epsilon^{-0.5}$ = 0.1 and (d) $\epsilon^{-0.5}$ = 0.0315; (c) and (d) are referred to as C-rk1 and C-rk2 in the text, respectively.

Iga and Matsuda (2005)

波の検出: VMC/Venus Expressデータの解析

- スーパーローテーションが
  遅いとき → 赤道ケルビン波
  速いとき → 中緯度ロスビー波

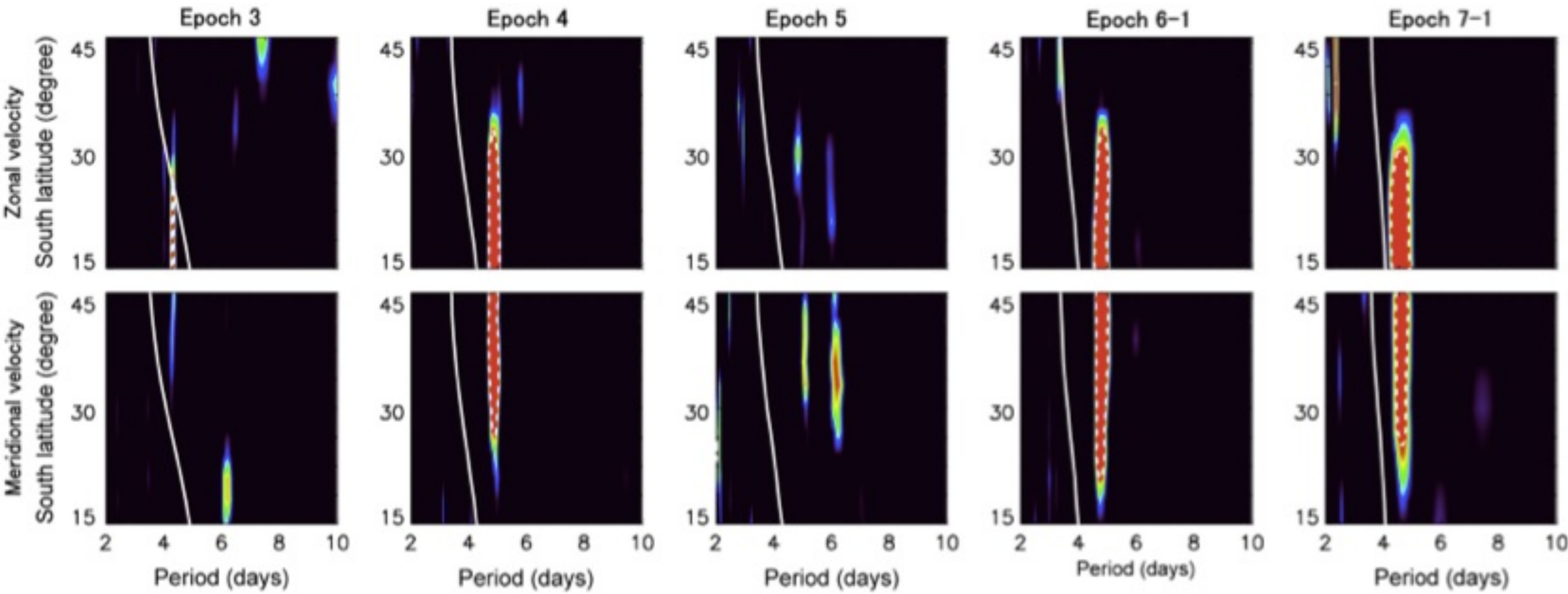

Kouyama et al. (2015)

金星版 QBO

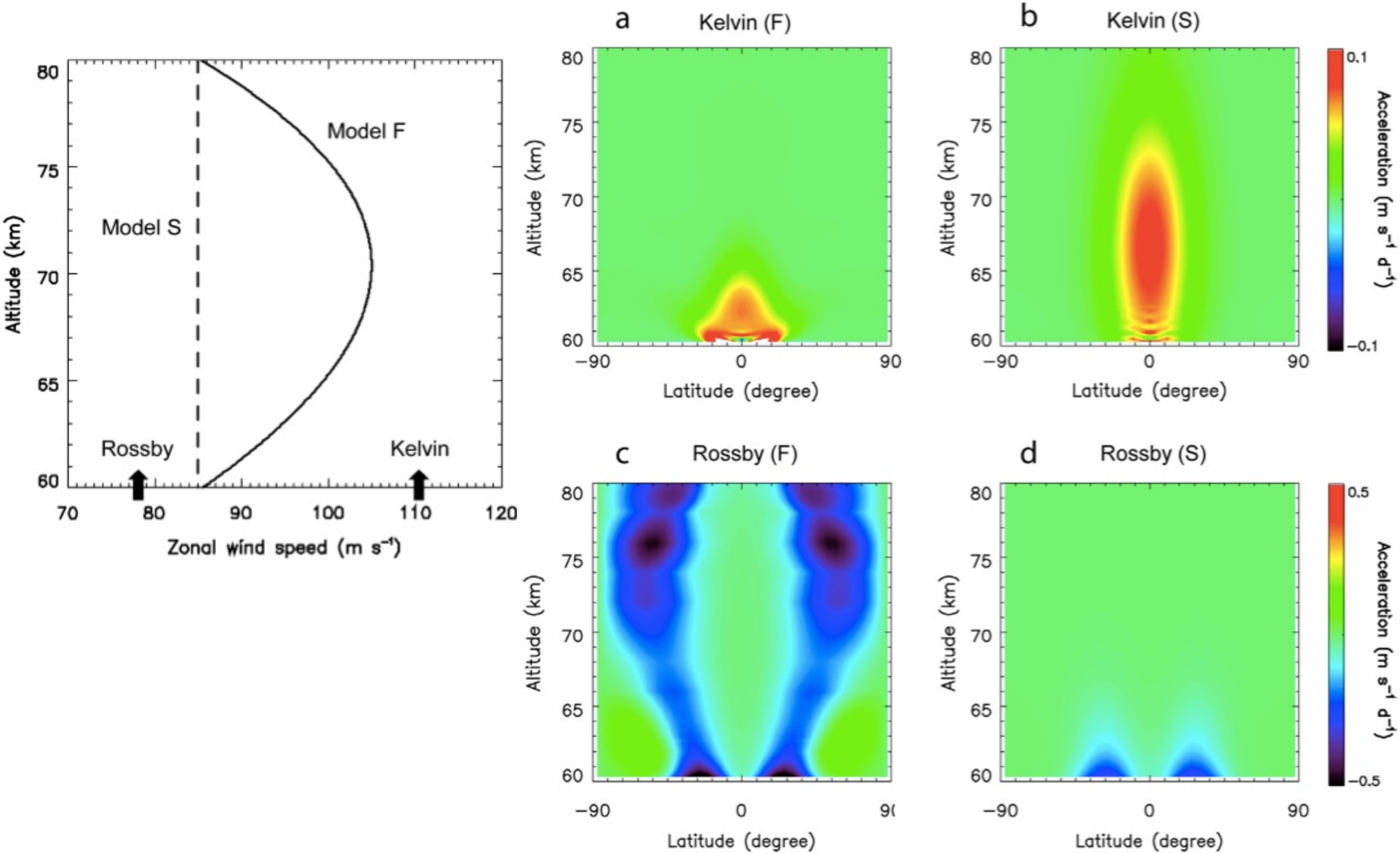

Kouyama et al. (2015)

地形性重力波の鉛直伝播

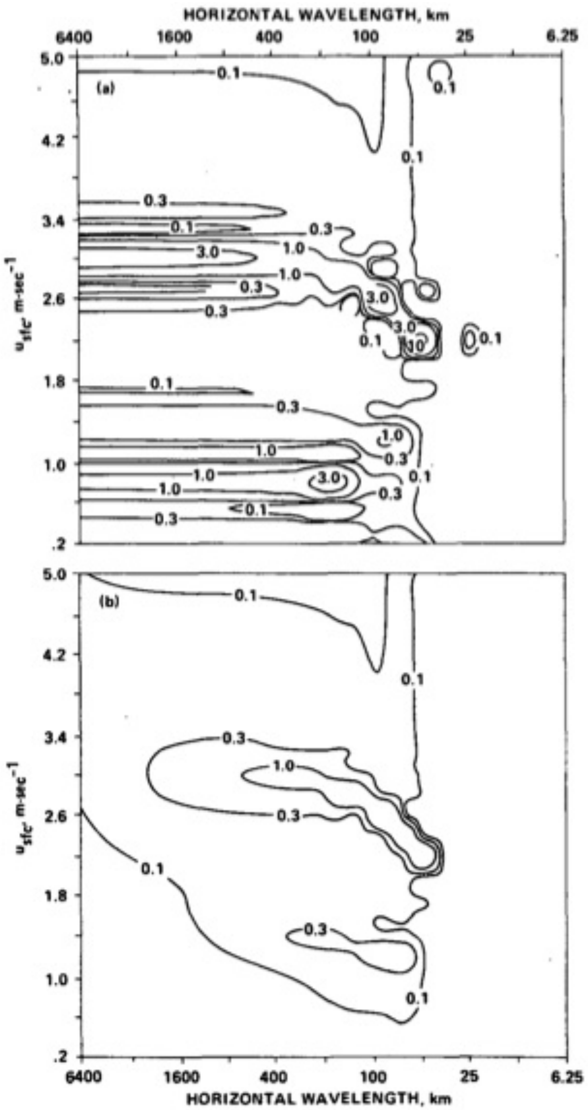

FIG. 2. Contours of wave amplification factor WA in a surface wind and horizontal wavelength diagram. $z_0 = 0$, $k_y = 0$. (a) inviscid; (b) $K = 0.7\ m^2\ s^{-1}$.

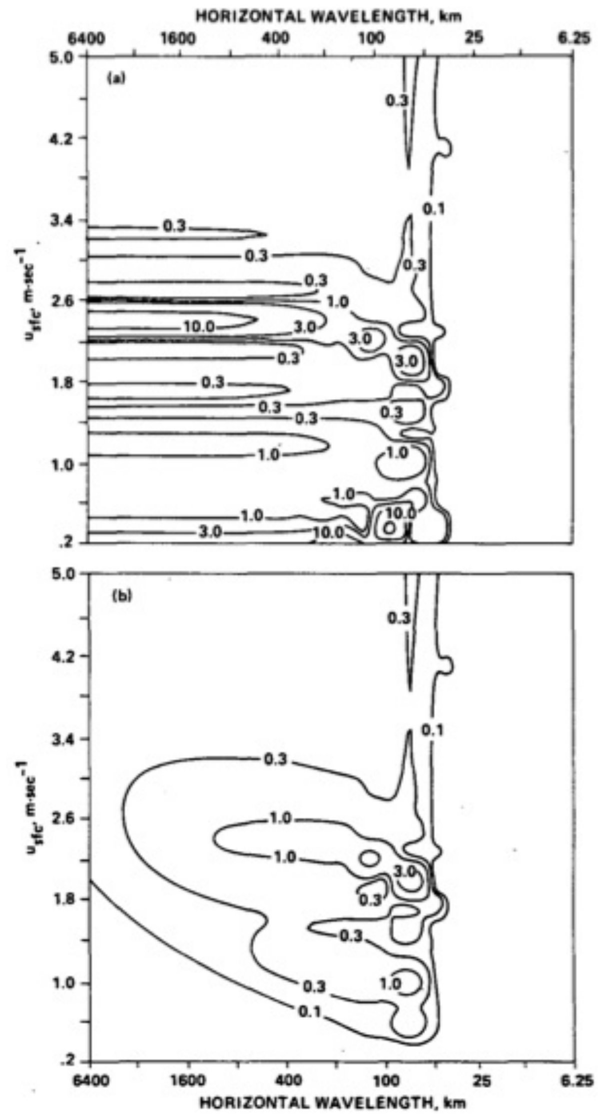

FIG. 3. As in Fig. 2 except $z_0 = 4$ km.

Young et al. (1987)

金星大気の傾圧不安定

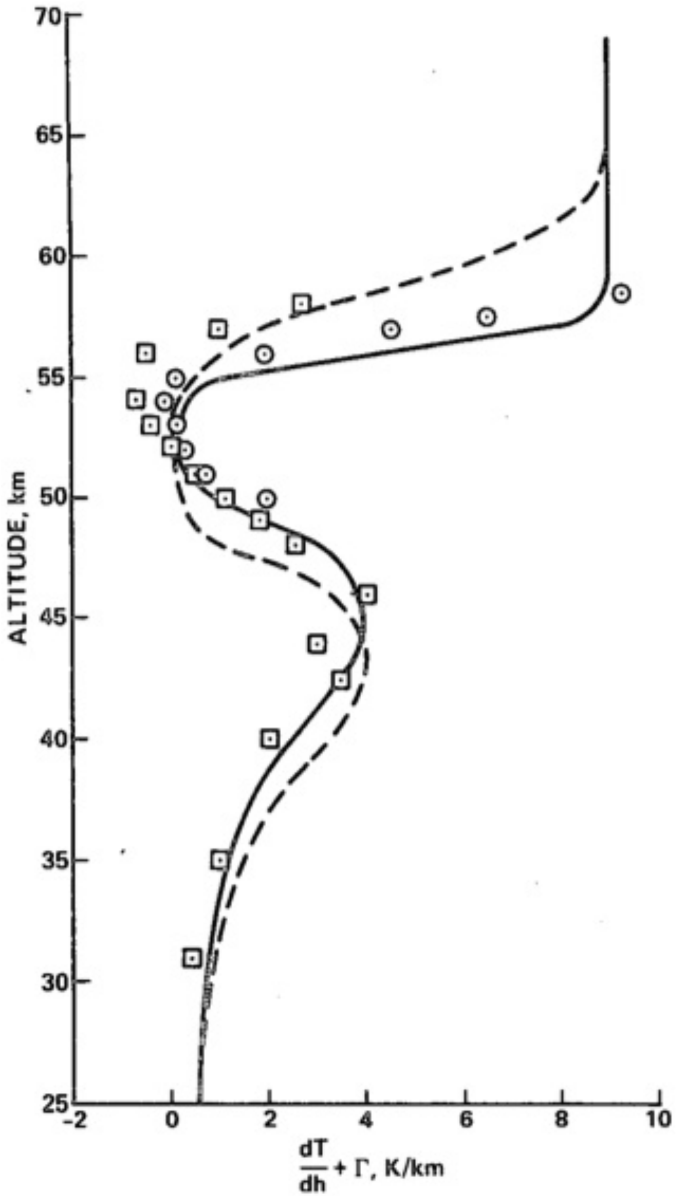

$$\bar{u}(z, \theta) = f(z)g(\theta), \qquad (3.1)$$

$$g_1(\theta) = \cos\theta \qquad (3.2a)$$

$$g_2(\theta) = \begin{cases} 1, & 0 \leqslant |\theta| \leqslant 40^\circ \\ \dfrac{3}{2}\dfrac{\cos\theta}{\cos 40^\circ} - \dfrac{1}{2}\dfrac{\cos^3\theta}{\cos^3 40^\circ}, & 40^\circ \leqslant |\theta|. \end{cases} \qquad (3.2b)$$

$$f_1 = 40\ \mathrm{m\ s^{-1}} + (0.86\ \mathrm{m\ s^{-1}\ km^{-1}})(z - \text{[illegible]}5)\ \mathrm{km}; \qquad (3.3)$$

f2: Day probe at 30N

Young et al. (1984)

傾圧不安定波の成長率

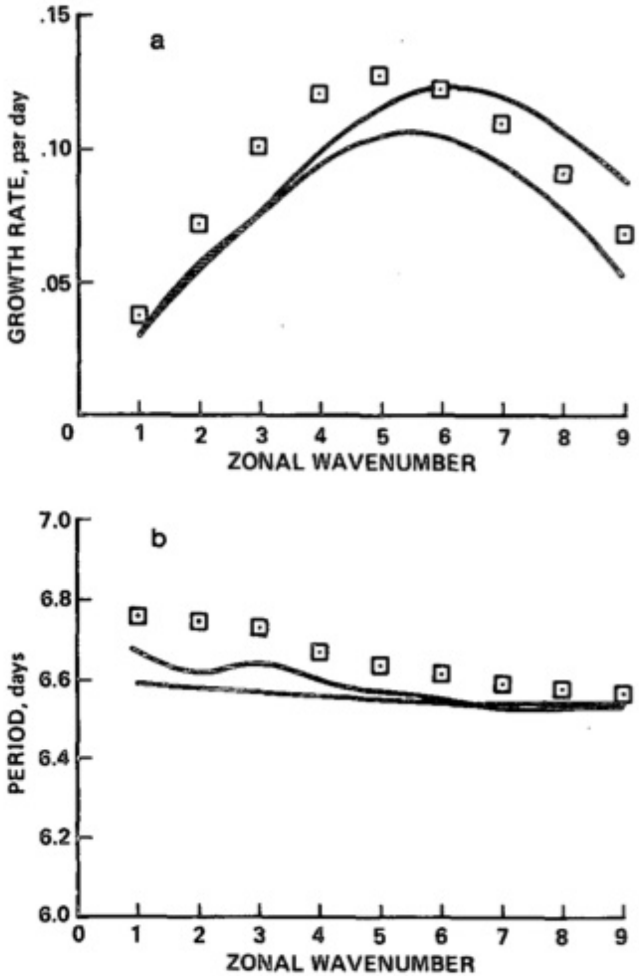

FIG. 3. (a) Growth rate spectrum for $\bar{u} = f_1 g_1$, $So_{\min} = 0.2$ K km^{-1}. Both first and second fastest growing modes are shown. Also included are the "quasi-cyclostrophic" values for growth rates denoted by squares. (b) Period as function of wavenumber. Quasi-cyclostrophic values denoted by squares.

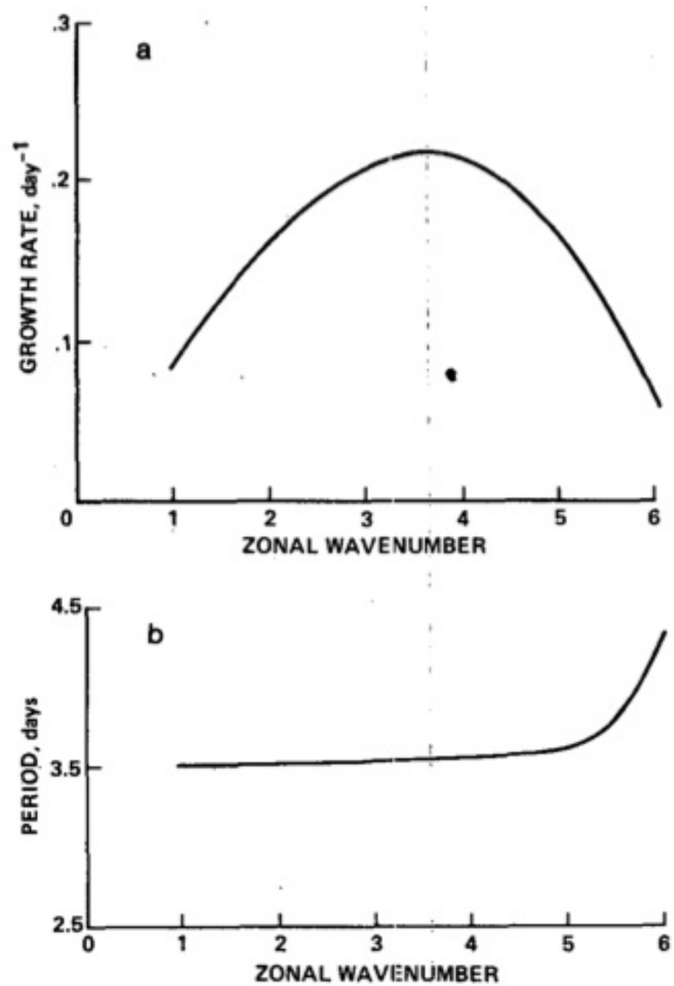

FIG. 6. (a) Growth rate spectrum for $\bar{u} = f_2 g_2$, $So_{\min} = 0.2$ K km^{-1}. (b) Period as function of zonal wavenumber.

Young et al. (1984)

傾圧不安定のパラメータ依存性

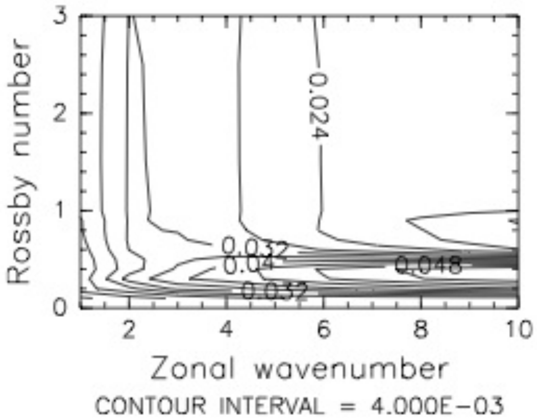

Figure 1. Distribution of dimensionless growth rate of the first unstable mode obtained for R_i = 5.0, 1 ≤ m ≤ 10 (horizontal axis), and 0.1 ≤ R_o ≤ 3.0 (vertical axis).

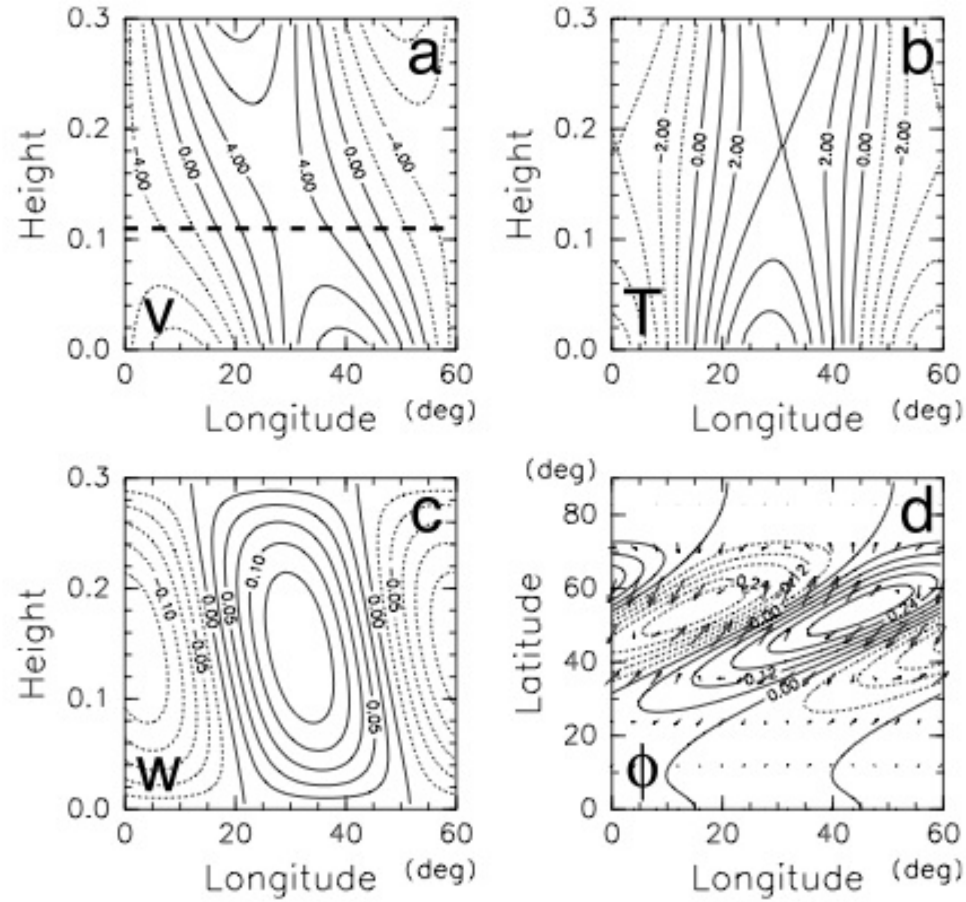

Figure 2. Structure of the first unstable mode obtained for R_i = 5.0, R_o = 0.3 and m = 6: (a) meridional velocity, (b) temperature deviation, and (c) vertical velocity on the zonal-vertical section at 55° latitude, where amplitude of geopotential deviation takes its maximum value. Horizontal

Takagi and Matsuda (2006b)

GCM による傾圧不安定の数値実験

剛体回転の場合

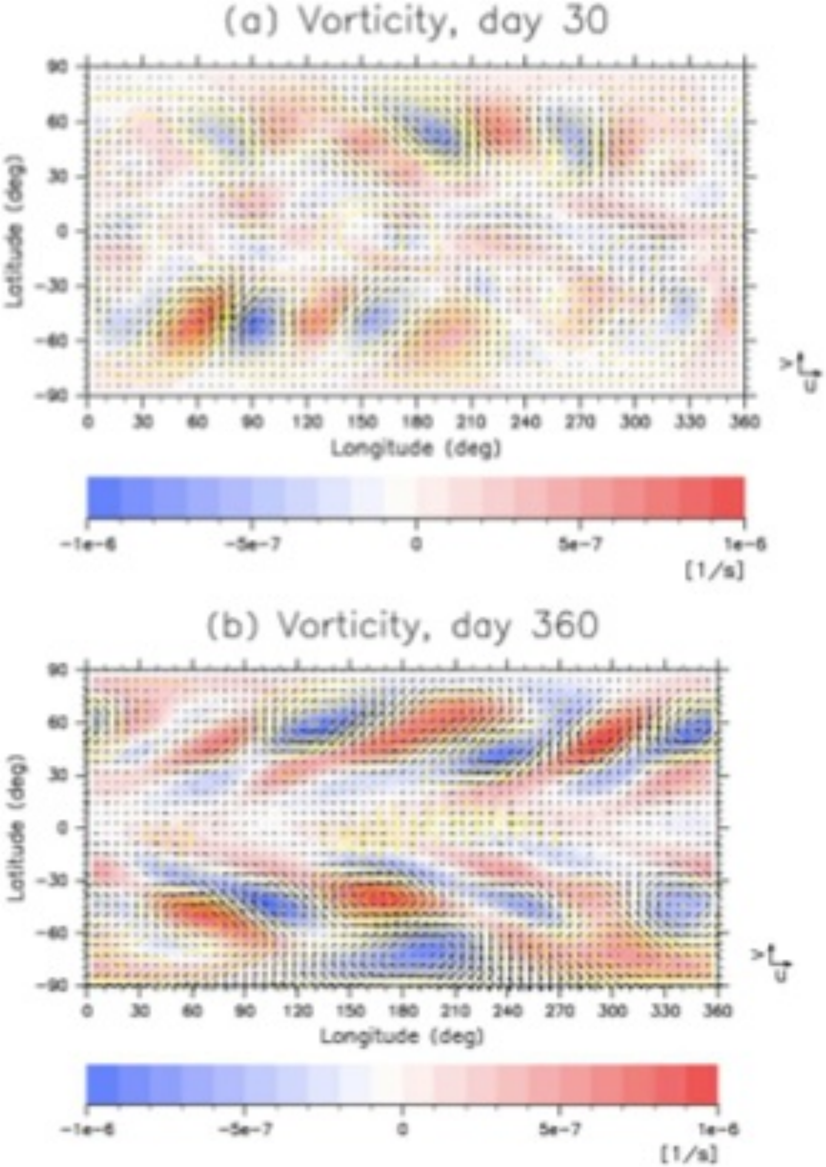

弱い中緯度ジェットの場合

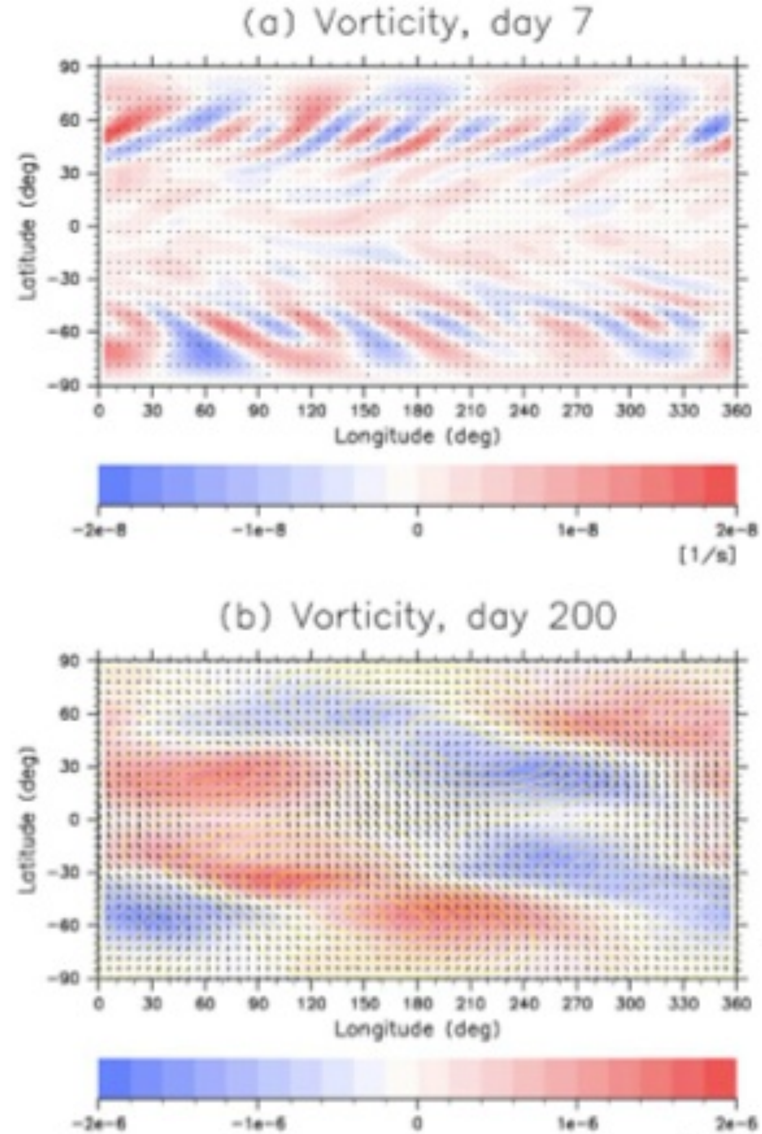

Sugimoto et al. (2014a)

GCM 実験にみられる波活動

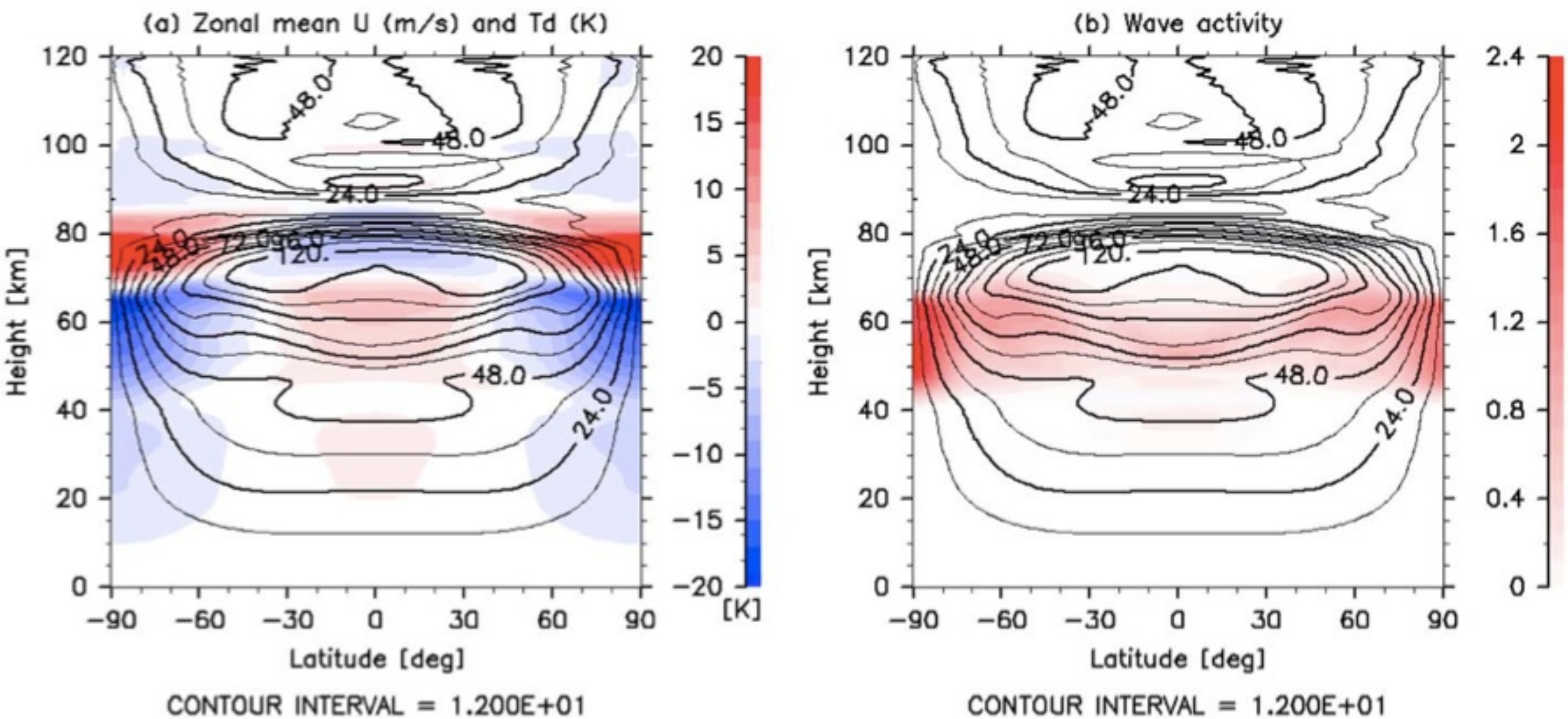

Figure 1. Latitude-height cross sections of zonal-mean zonal flow (black contours, m s^{-1}), (a) temperature deviations from the horizontally averaged temperature (color shades, K) and (b) eddy kinetic wave activity defined by $(\overline{u'^2} + \overline{v'^2})/2$ averaged over 90 Earth days (color shades). Eddy components are extracted by a high-pass filter periods shorter than 10 Earth days. For Figure 1b, amplitude is weighted by the sigma.

Sugimoto et al. (2014b)

傾圧不安定波の鉛直構造

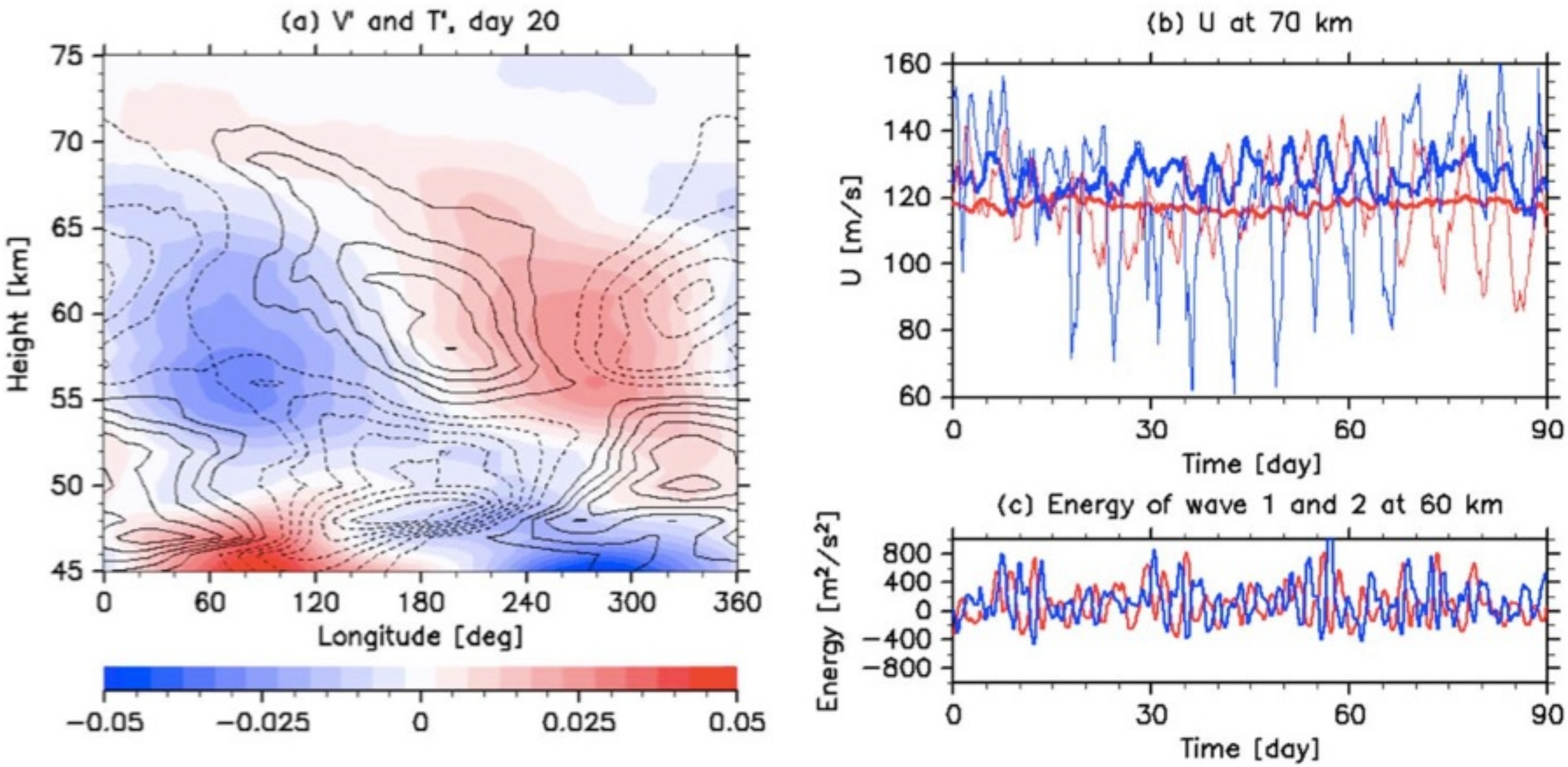

Figure 2. (a) Vertical distributions of meridional flow (black contours; intervals are 0.02 m s^{-1}) and temperature deviations (color shades) at 45°N at day 20. (b) Time evolution of zonal flow (thin lines) and zonal-mean zonal flow (thick lines) at the equator (red lines) and 45°N (blue lines) at 70 km. (c) Time evolution of eddy kinetic energy for wave numbers 1 (red line) and 2 (blue line) of the short-period disturbances averaged over latitudes from 30°N to 60°N at 60 km. For Figure 2a, amplitude is weighted by the sigma and a band-pass filter between the periods of 2 and 8 days is applied. For Figure 2c high-pass filter periods shorter than 10 days is applied.

Sugimoto et al. (2014b)

傾圧不安定波の水平構造

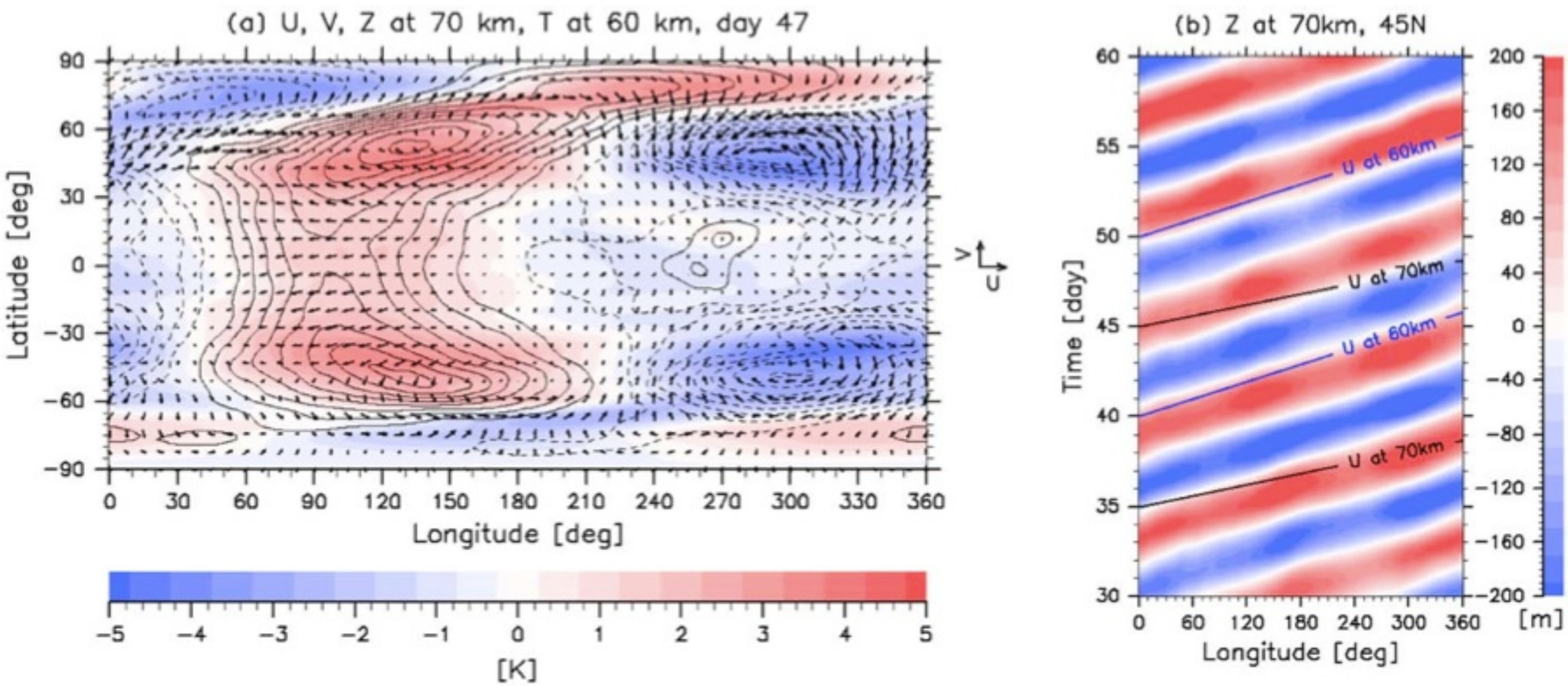

Figure 4. (a) Horizontal distributions of geopotential height (black contours; intervals are 25 m) and horizontal flow (black vectors; units 50 m s^{-1}) associated with the short-period disturbances at 70 km and temperature deviations at 60 km (color shades) at day 47. A band-pass filter between the periods of 2 and 8 Earth days is applied. (b) Hovmöller diagram of geopotential height deviations at 70 km at 45°N. Black and blue lines represent the zonal-mean zonal flow at 70 km and 60 km, respectively.

Sugimoto et al. (2014b)

極渦のGCMシミュレーション（平均場）

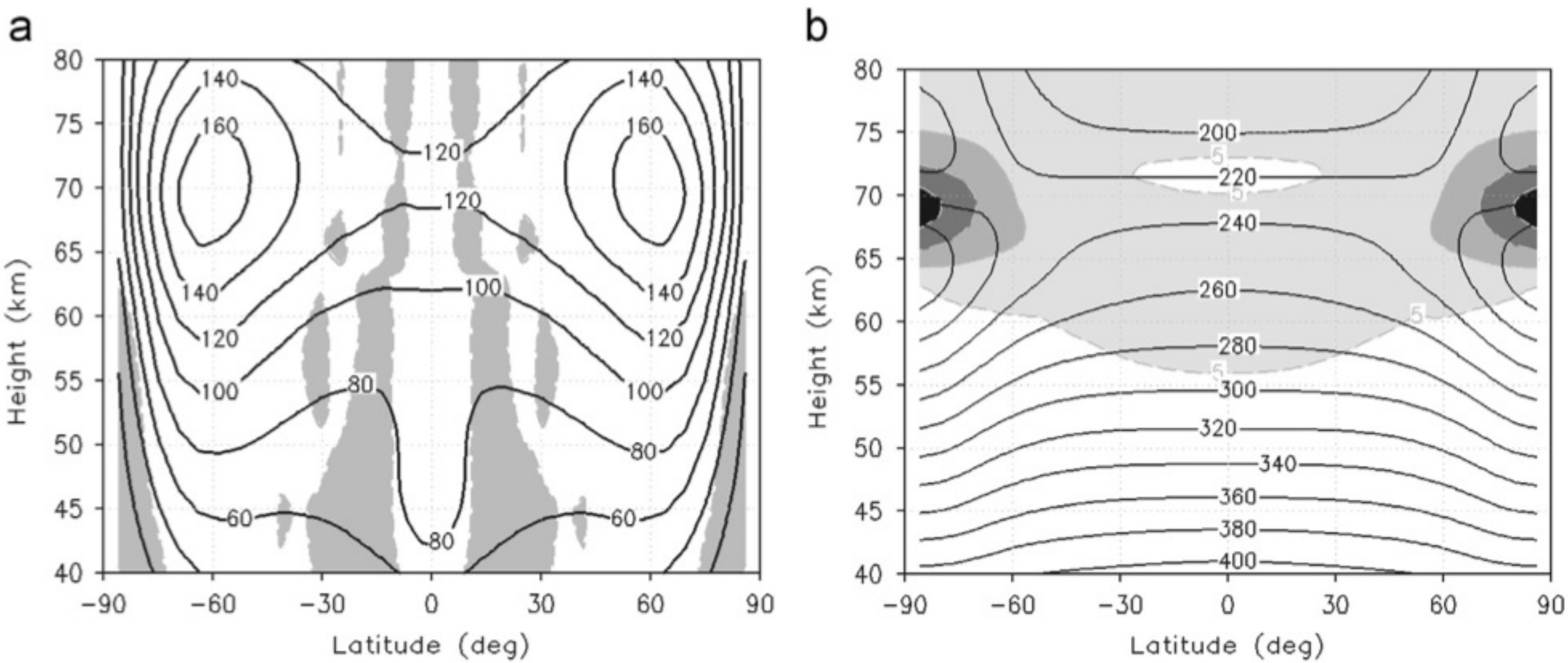

東西波数1，周期5.5日の赤道波
を下端で強制

Yamamoto and Takahashi (2015)

GCMで再現された極渦

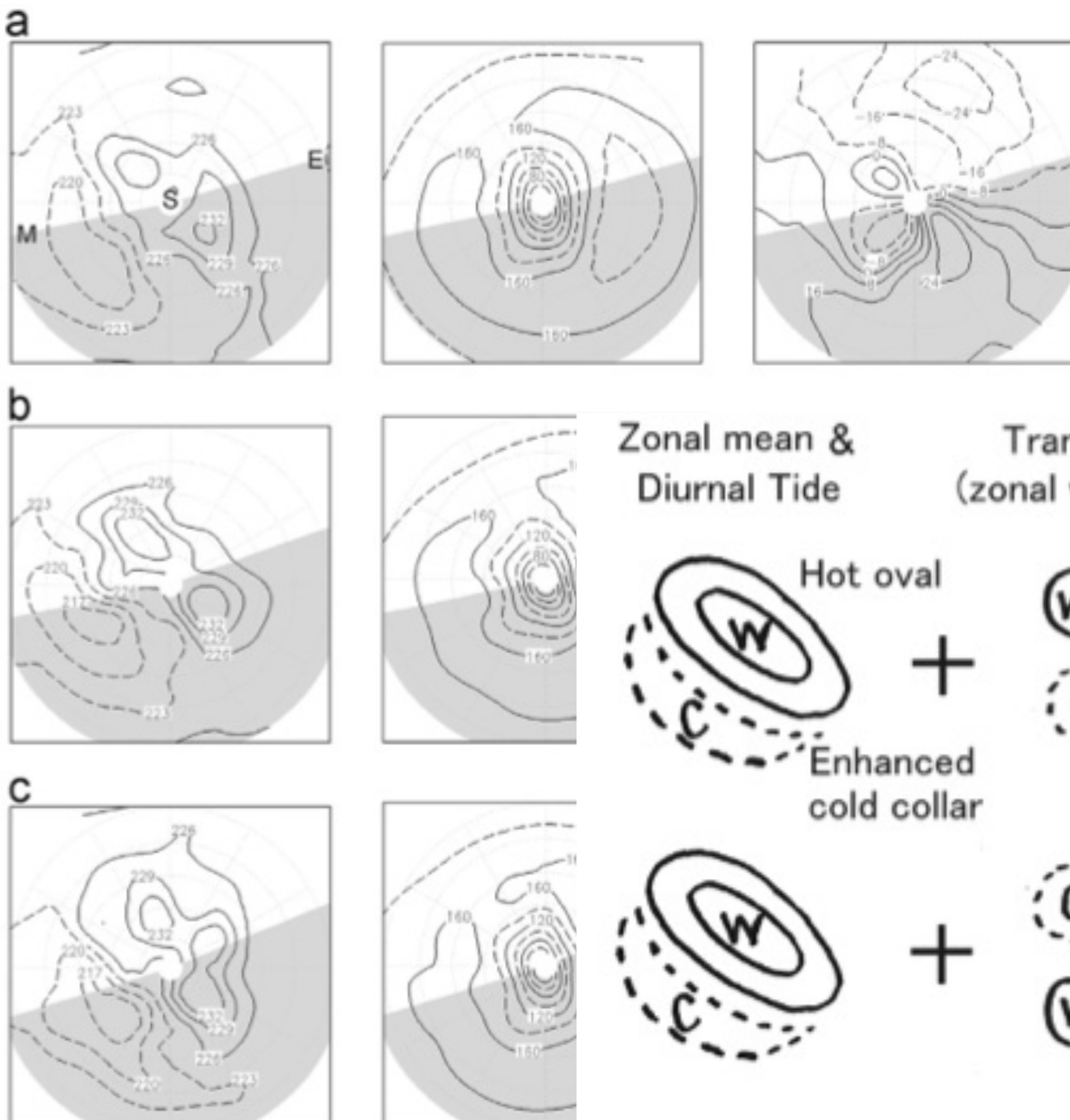

Yamamoto and Takahashi (2015)

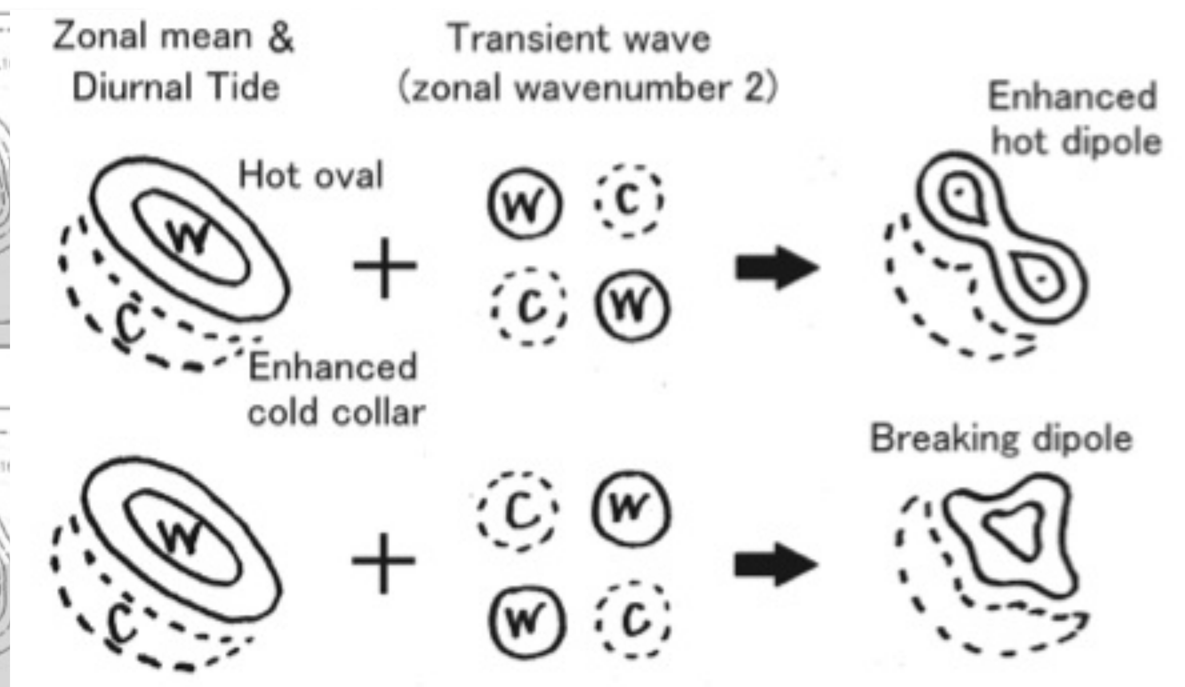

Fig. 10. Schematic showing the superposition of the slow diurnal tide and fast transient wave.

周極低温域 (cold collar) の再現

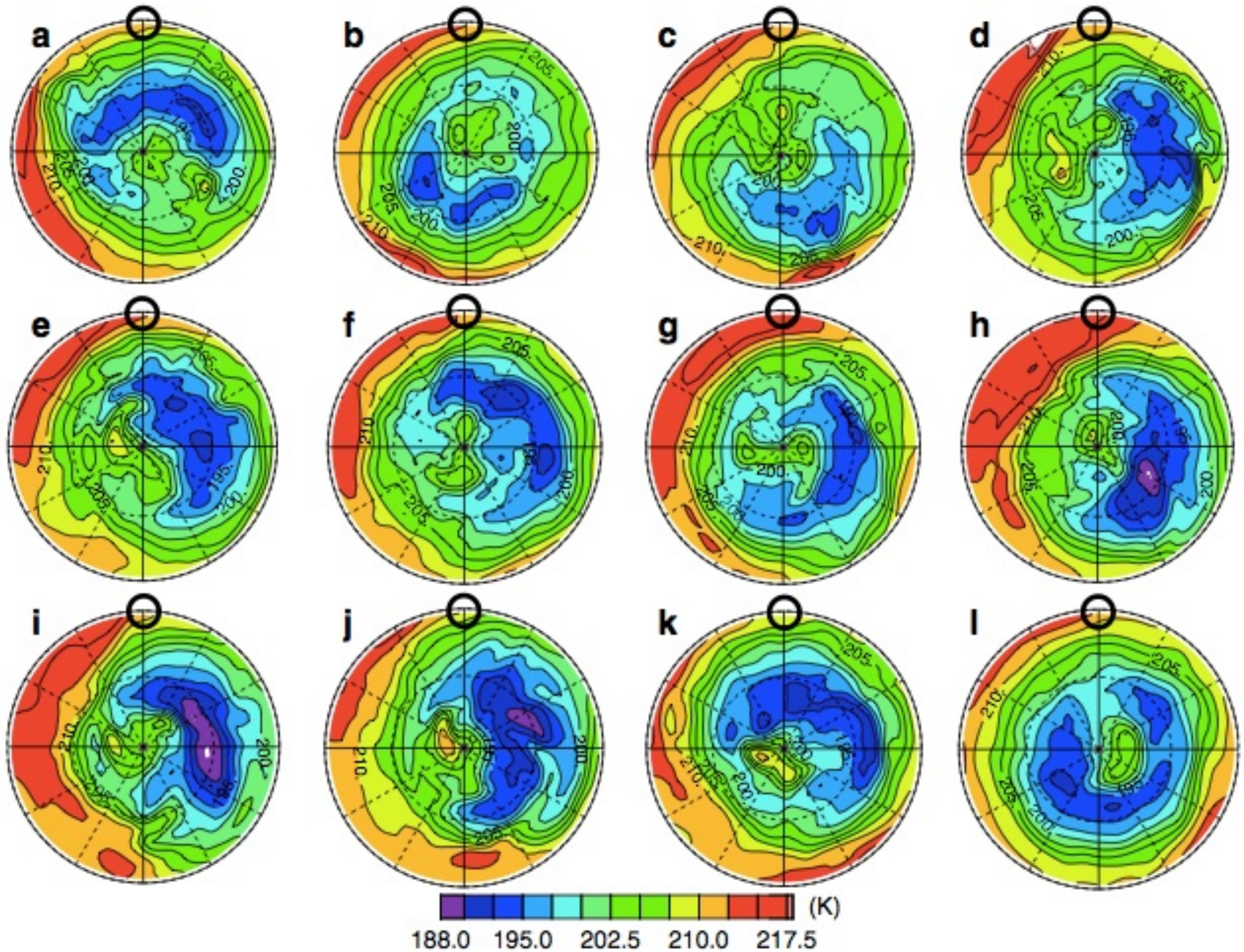

Figure 3 | Time evolution of the temperatures (K) at ~68 km (the pressure level of 4×10^3 Pa) in Case A in the polar plot. The latitude range is from 30°N to 90°N. The black circle represents the local solar noon. Each panel of (**a**) to (**l**) shows temperature distribution from 1414 to 1425 days from the start of the calculation. The time interval between the adjacent panels is one Earth day.

Ando et al. (2016)

熱潮汐波と残差子午面循環

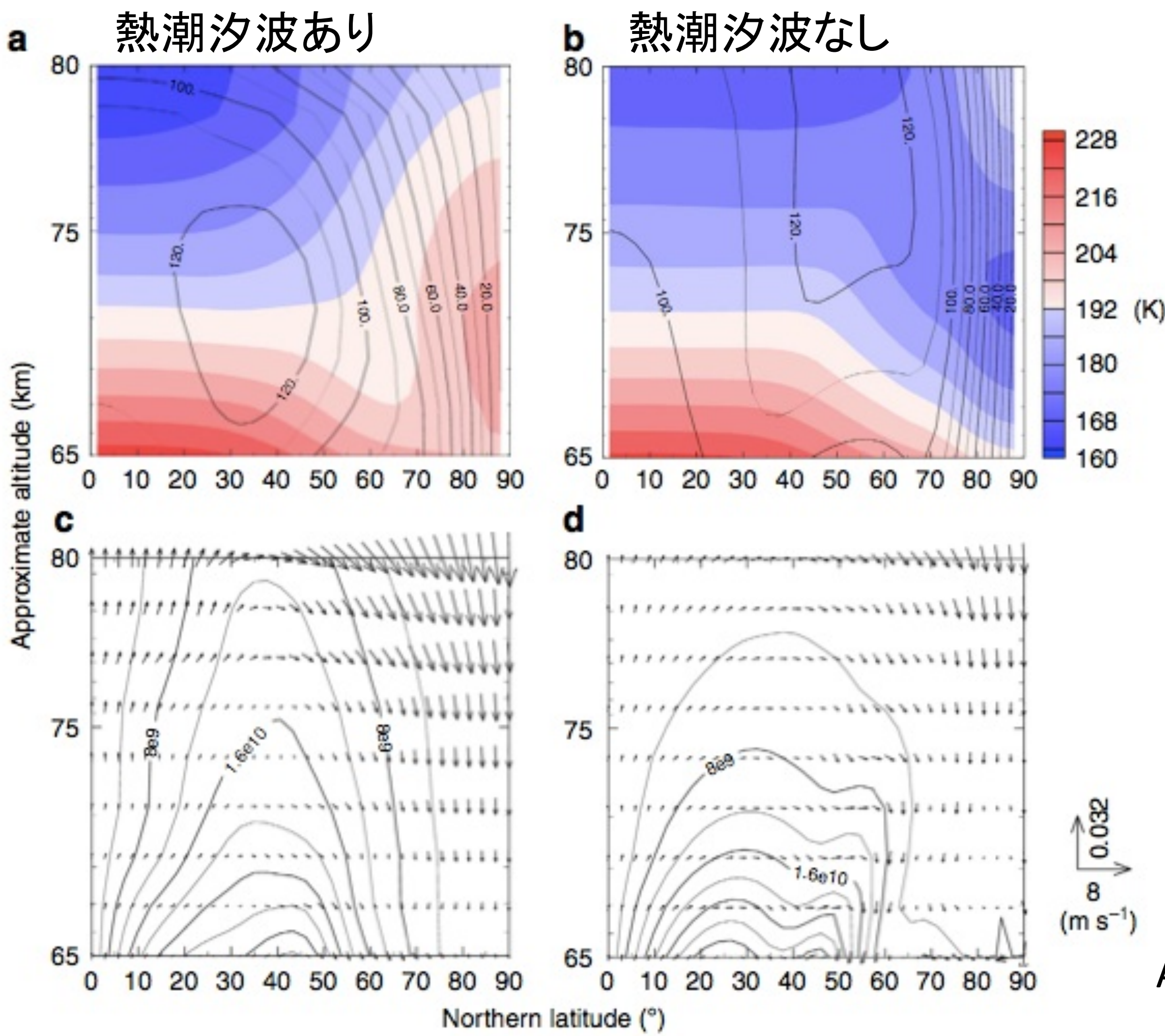

Ando et al. (2016)

Figure 6 | Meridional cross-sections of the zonally and temporally averaged zonal wind (solid line) and temperature (colour shade) and the horizontal and vertical components of the residual mean meridional circulation (vector) and mass stream fuction (contour). (**a**) Zonal wind and temperature in Case A. (**b**) Those in Case B. (**c**) Residual mean meridonal circulation vector and mass stream function in Case A. (**d**) Those in Case B. Averaged period is two Venusian solar days (234 Earth days) after settling into the quasi-steady state.

Zonal wind of the thermal tide at 70 km

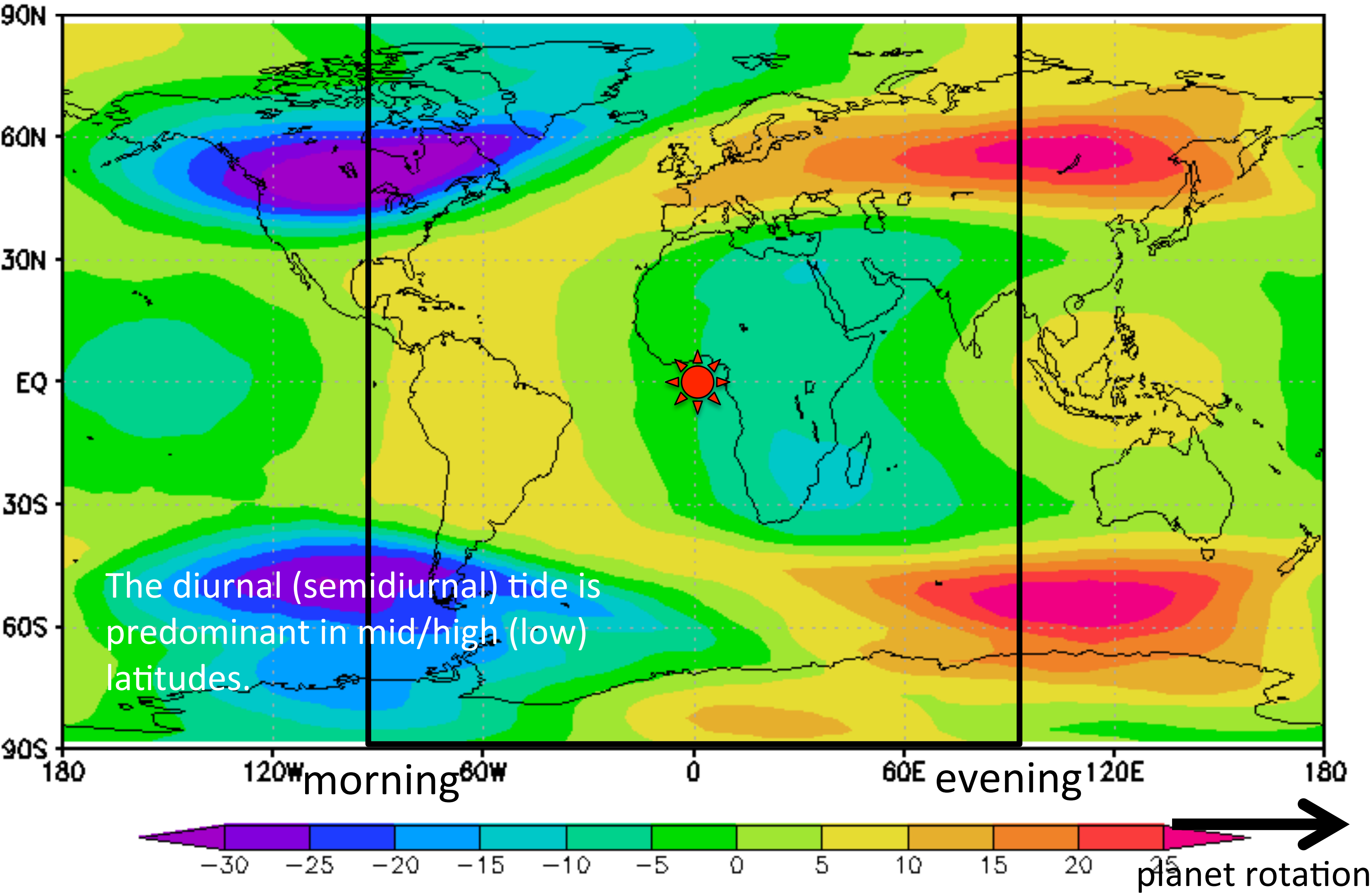

Meridional wind of the thermal tide at 70 km

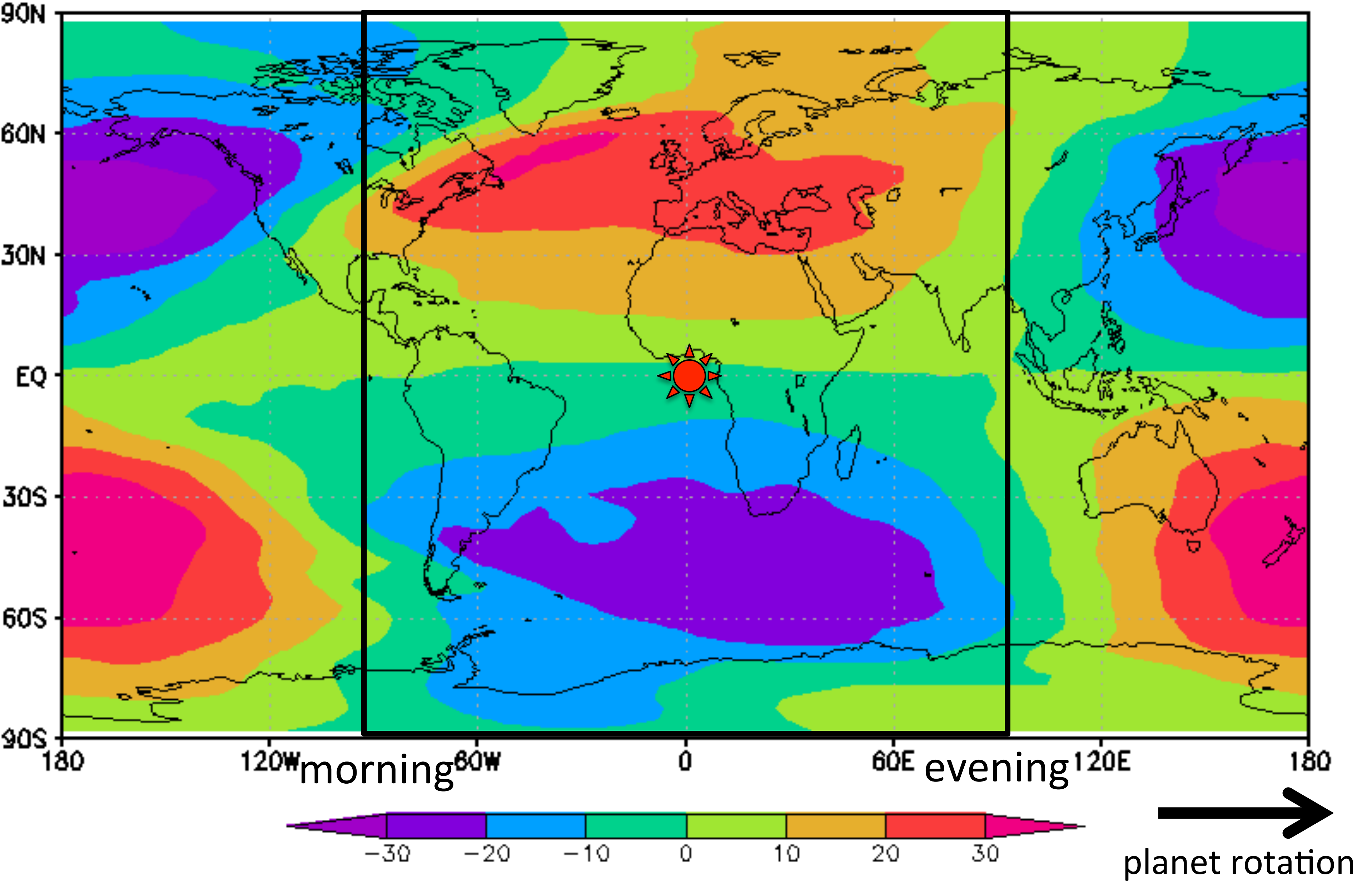

Temperature of the thermal tide at 70 km

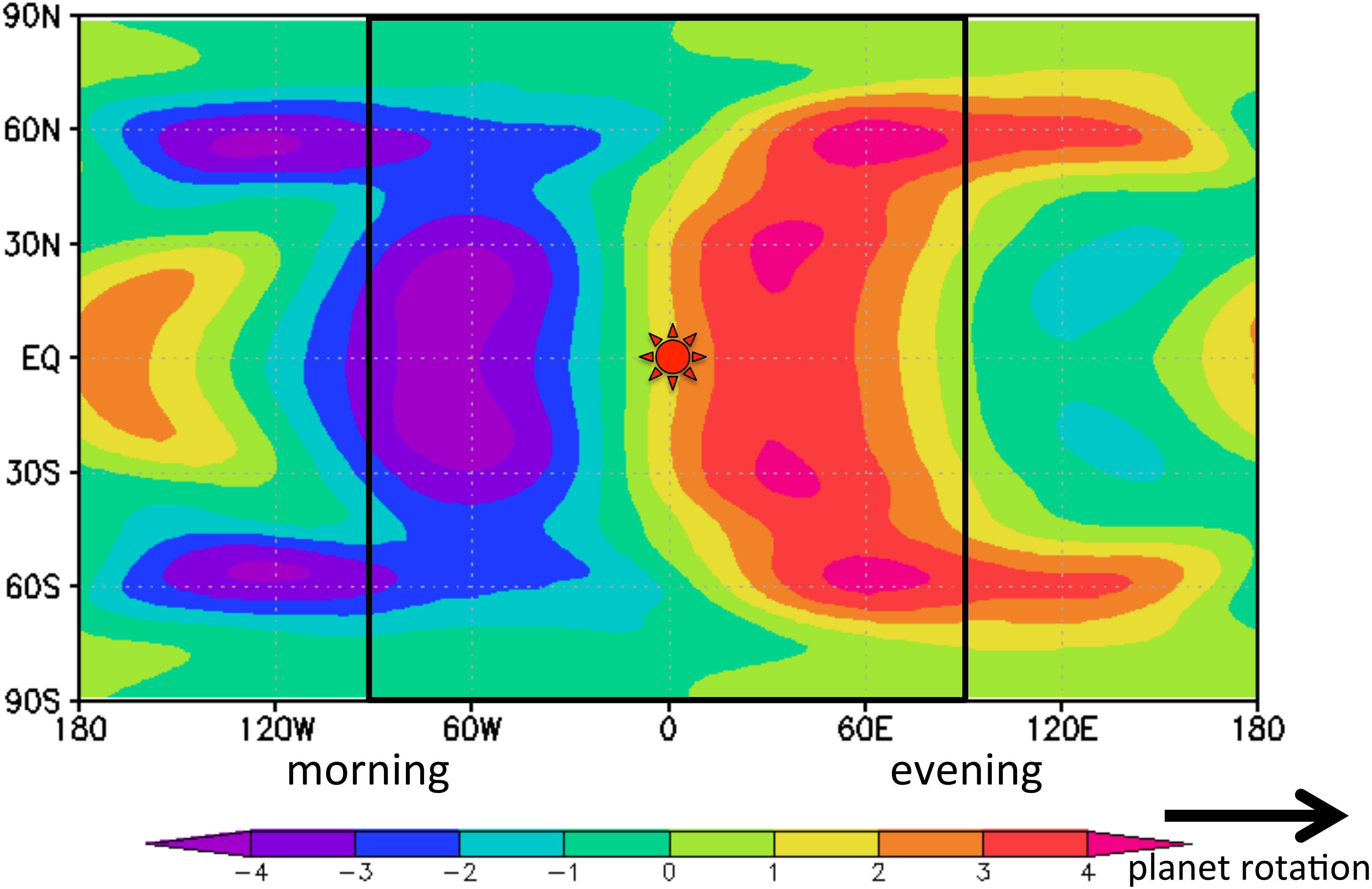

雲頂高度での風速分布（雲追跡風との比較）

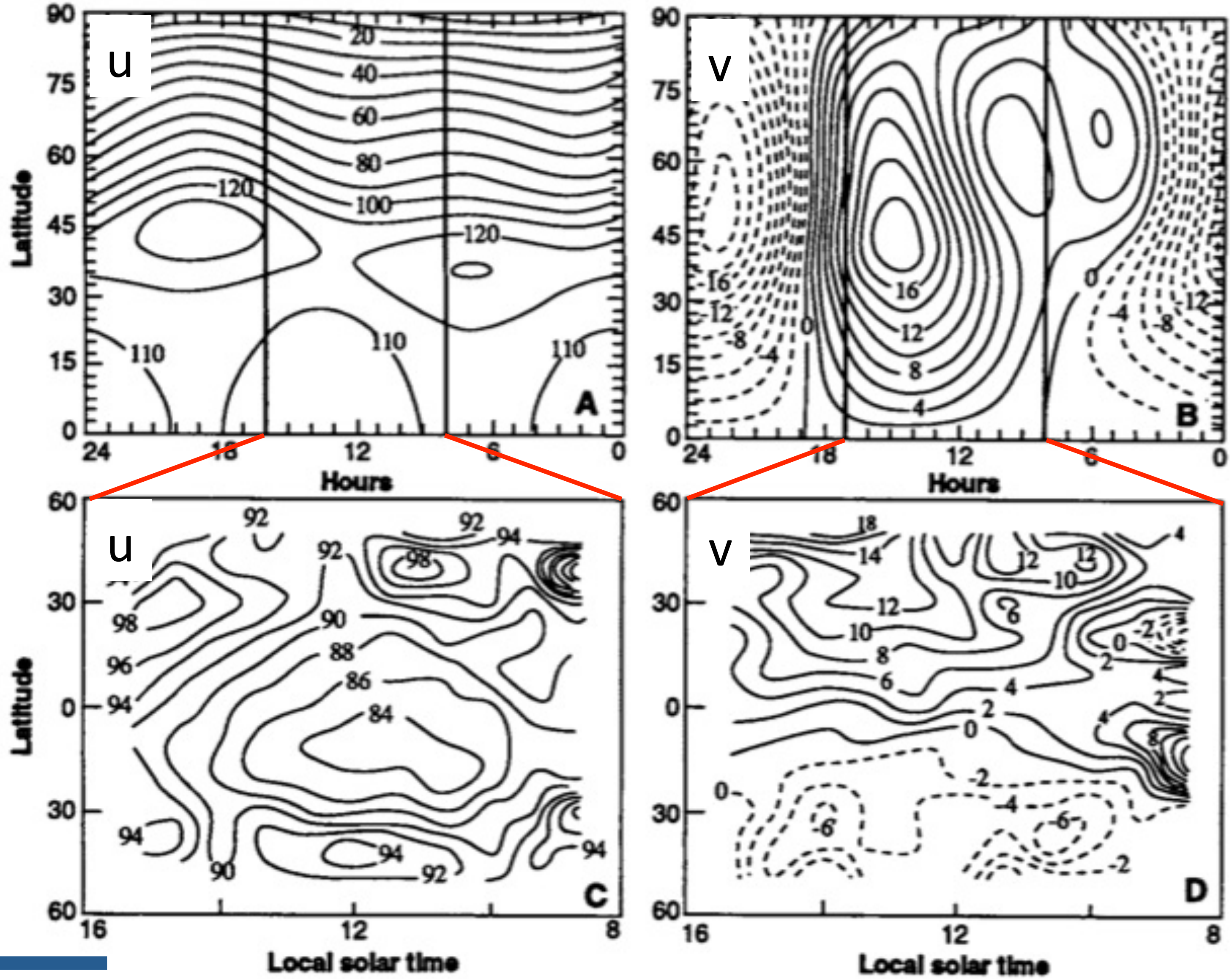

雲追跡による推定

planet rotation

Newman and Leovy (1992)

The GCM simulation results are consistent with the linear theory. (Takagi and Matsuda 2005)

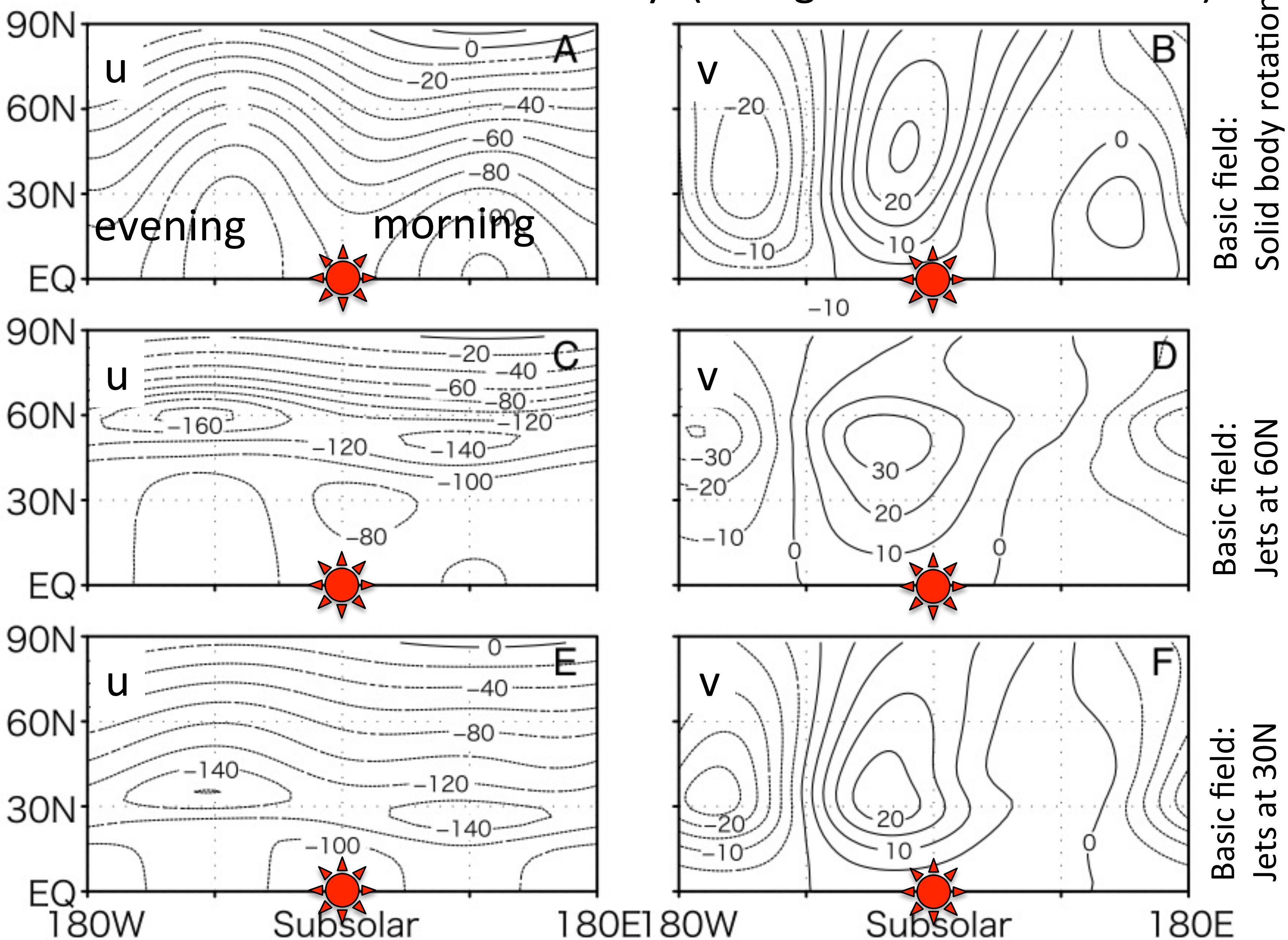

Vertical wind of the thermal tide at 70 km

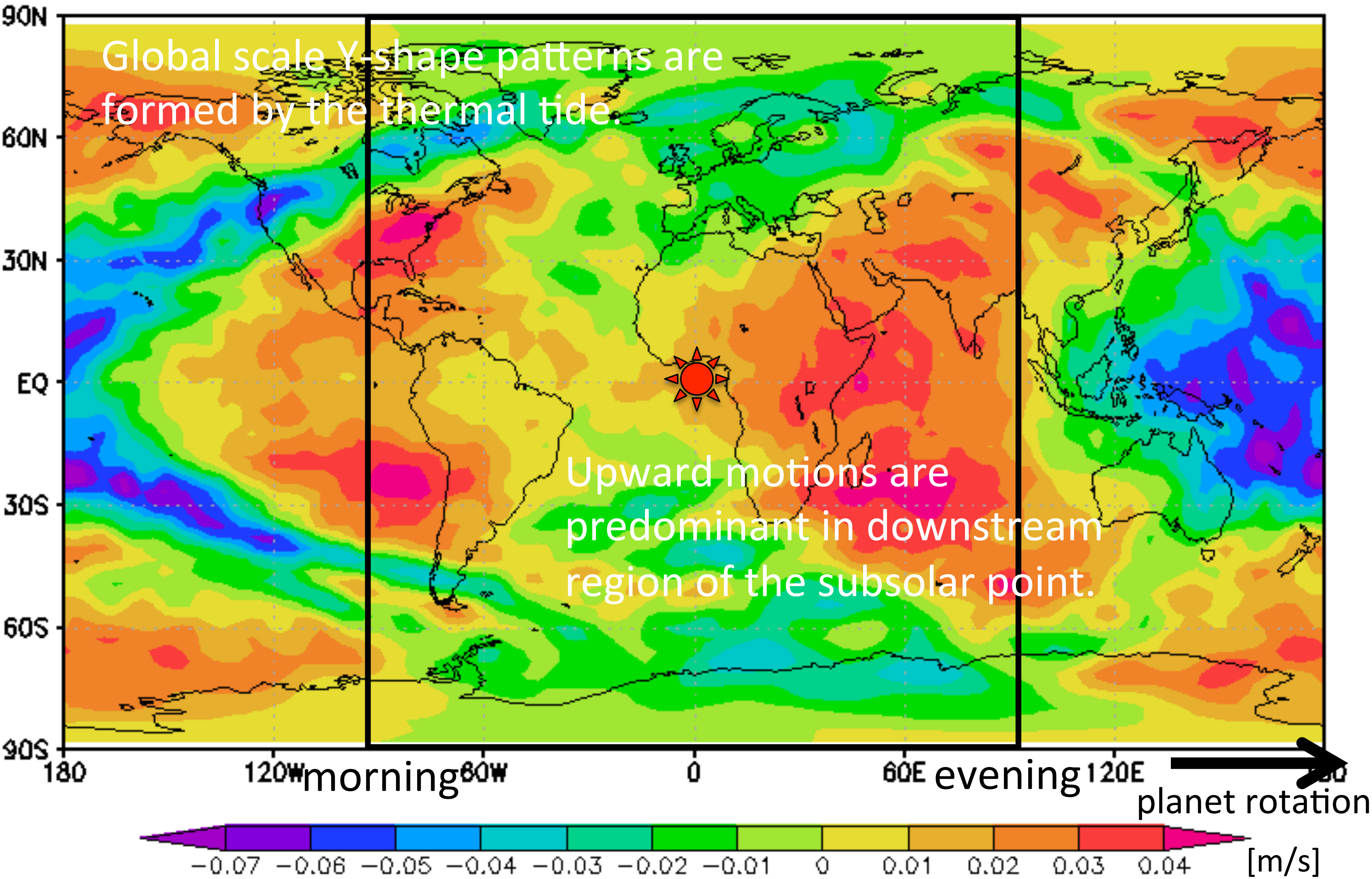

Vertical wind of the thermal tide at the equator

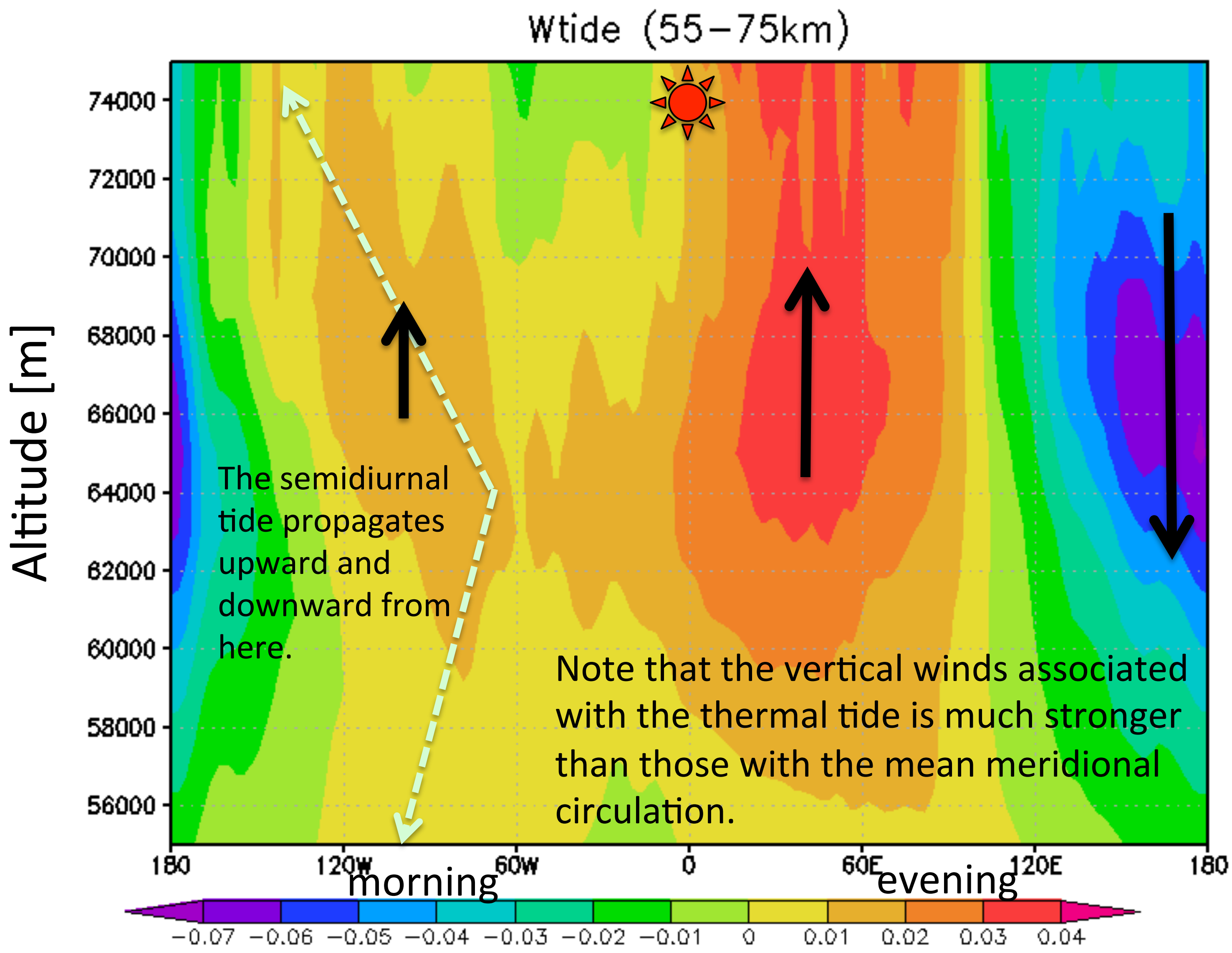

Equatorial dark region downstream of the subsolar point, related to the thermal tide?

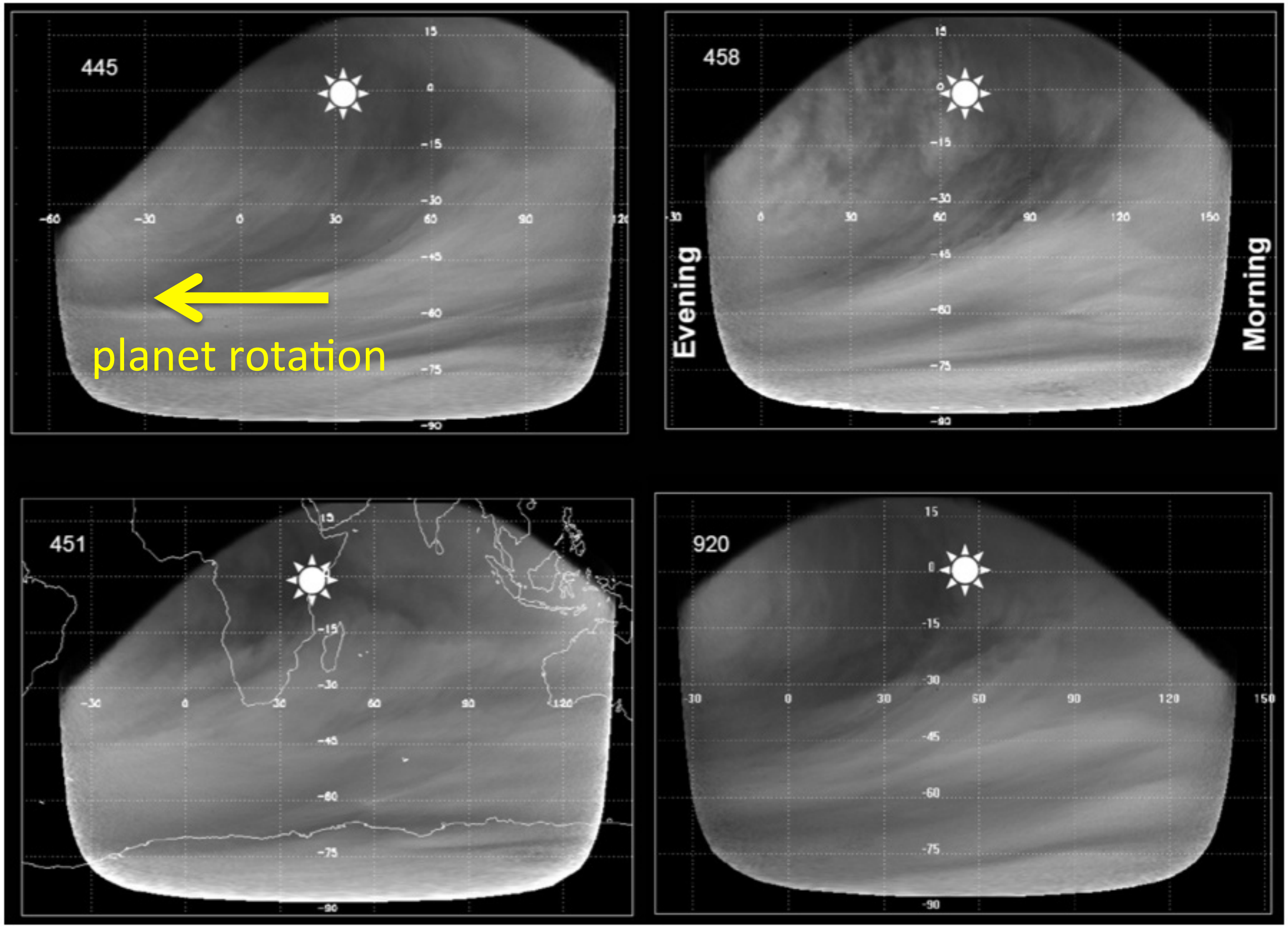

Fig. 6. UV images of the Venus Southern hemisphere in a simple cylindrical projection. Morning is on the right, evening is on the left. The atmosphere rotates from right to left. The Sun symbol marks the location of the sub-solar point. Orbit numbers are given in the upper left corner of each image. Contours of the Earth's continents are overplotted on the image from orbit #451 to illustrate position and scale of the Venus global cloud features.

Titov et al. (2012)

雲層高度の平均子午面循環
（オイラー平均）

南北流

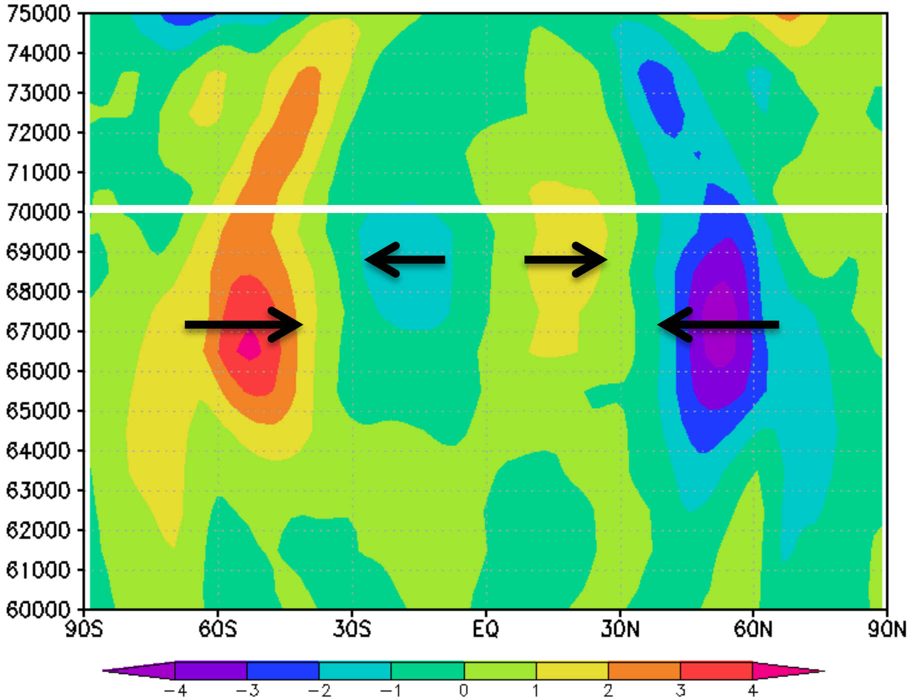

鉛直流

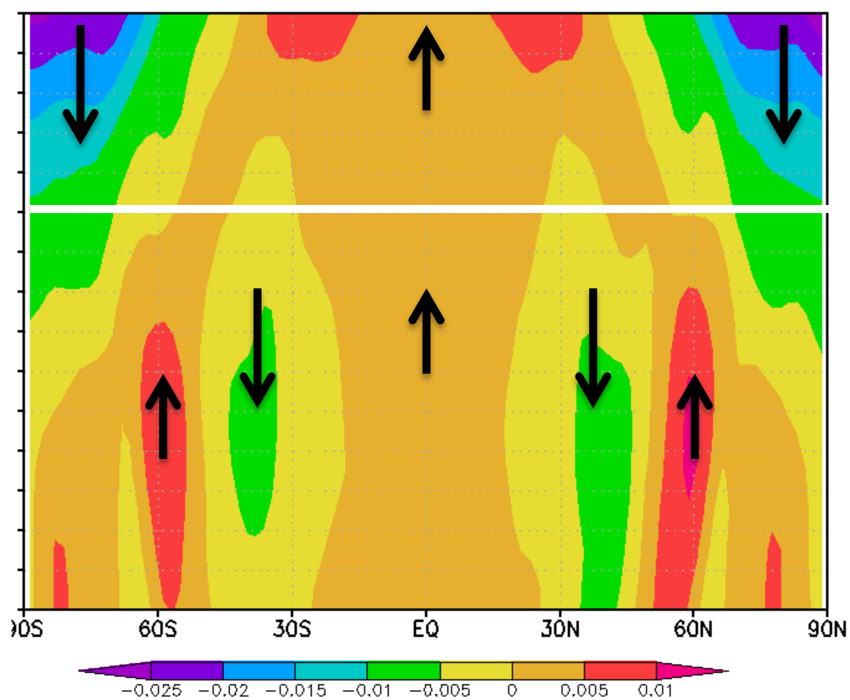

Thermal tide and short-period waves

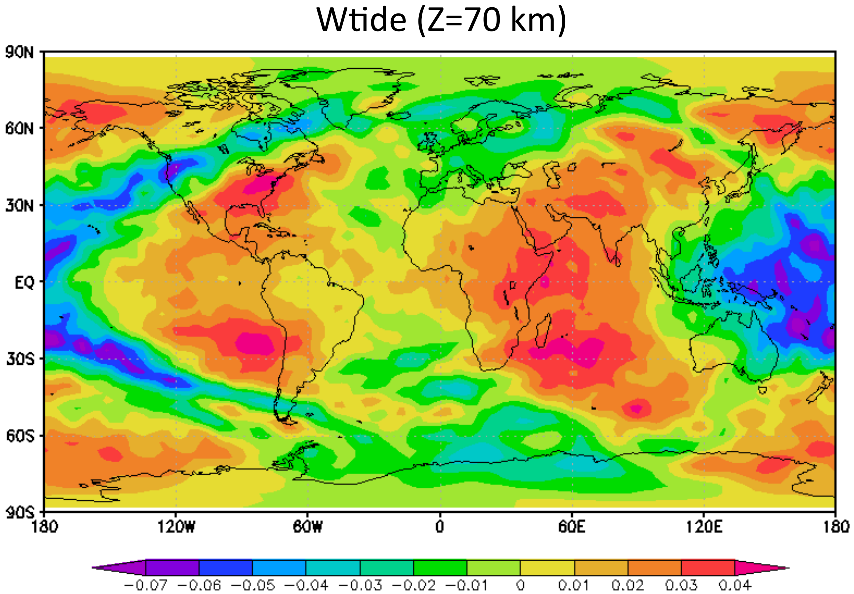

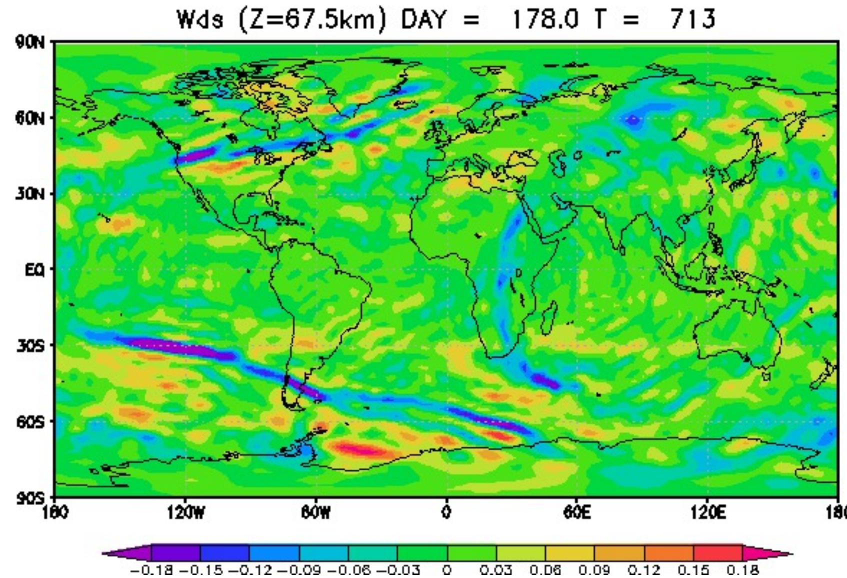

It seems that the short-period disturbances (Y- and bow-shape structures, convective cells, and gravity waves) are related to the vertical wind distribution of the thermal tide.
Are these disturbances generated by (nonlinear) interactions between the zonal wind and the thermal tide, as suggested by Belton et al. (1976)?

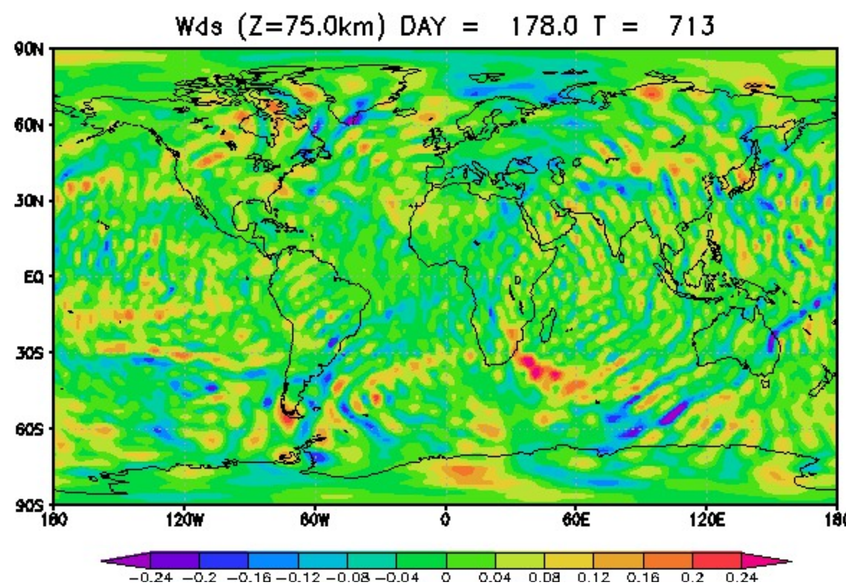

熱圏の大気大循環

- Bougher et al. (1986, 1988, 1990, 2006, 2015)
- Bougher and Borucki (1994)
- Brecht and Bougher (2012)
- Hoshino et al. (2012, 2013)

金星中間圏・熱圏の観測

高度	平均東西流	夜昼間対流	
> 70 km	高さとともに減少	?	温度分布からの推定
97 km	132±10 m/s	?	Shah et al. (1991), CO 吸収線
95 km	40±15 m/s	40±15 m/s	Lellouch et al. (1994), CO 吸収線
105 km	90±15 m/s	90±15 m/s	Lellouch et al. (1994), CO 吸収線
110±10 km	25±15 m/s	120±30 m/s	Goldstein et al. (1991), CO2 吸収線

大気光の時間変動（地上観測）

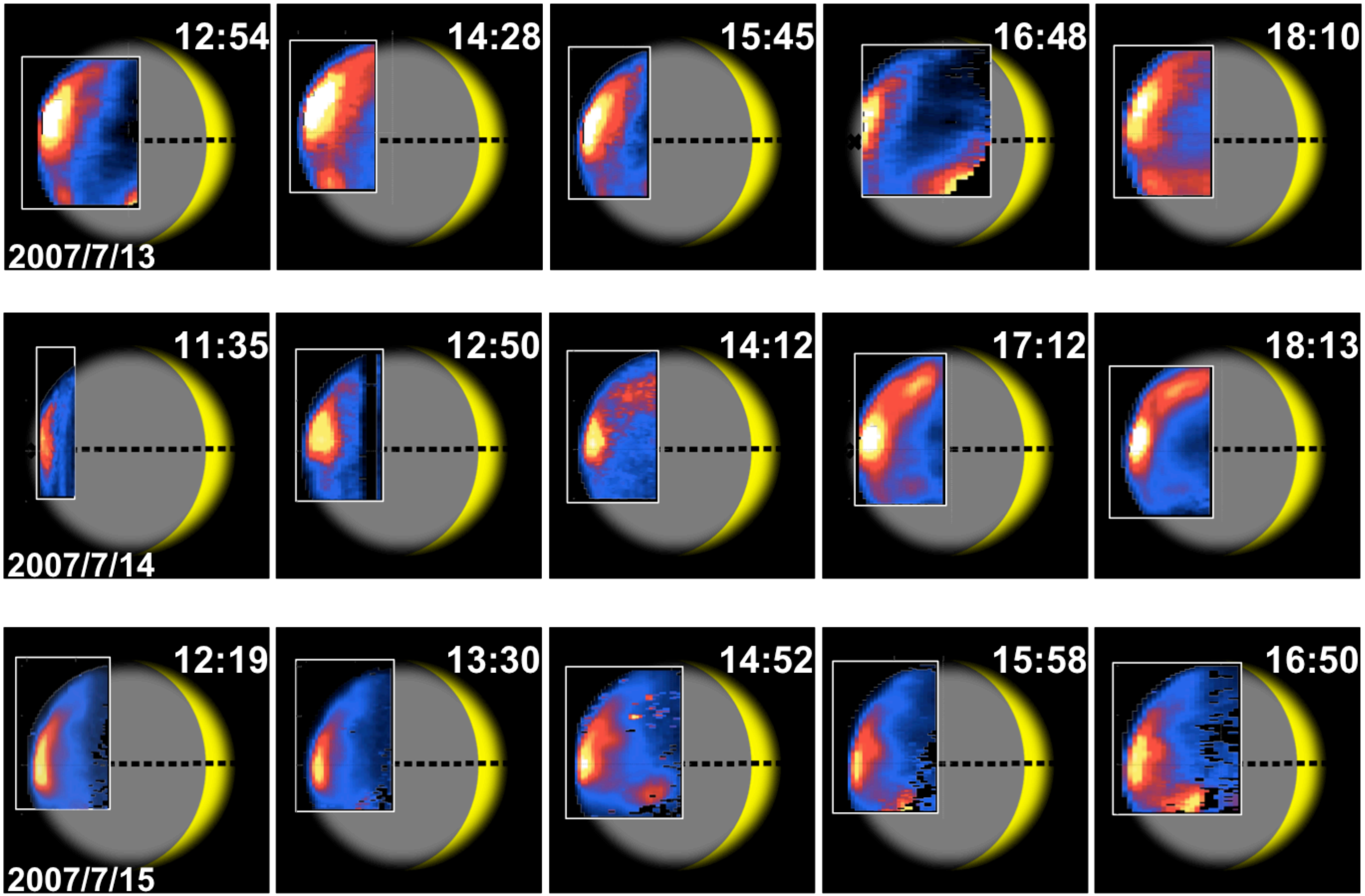

Ohtsuki et al. (2010)

VIRTIS/Venus Express の観測

高度 95-100 km

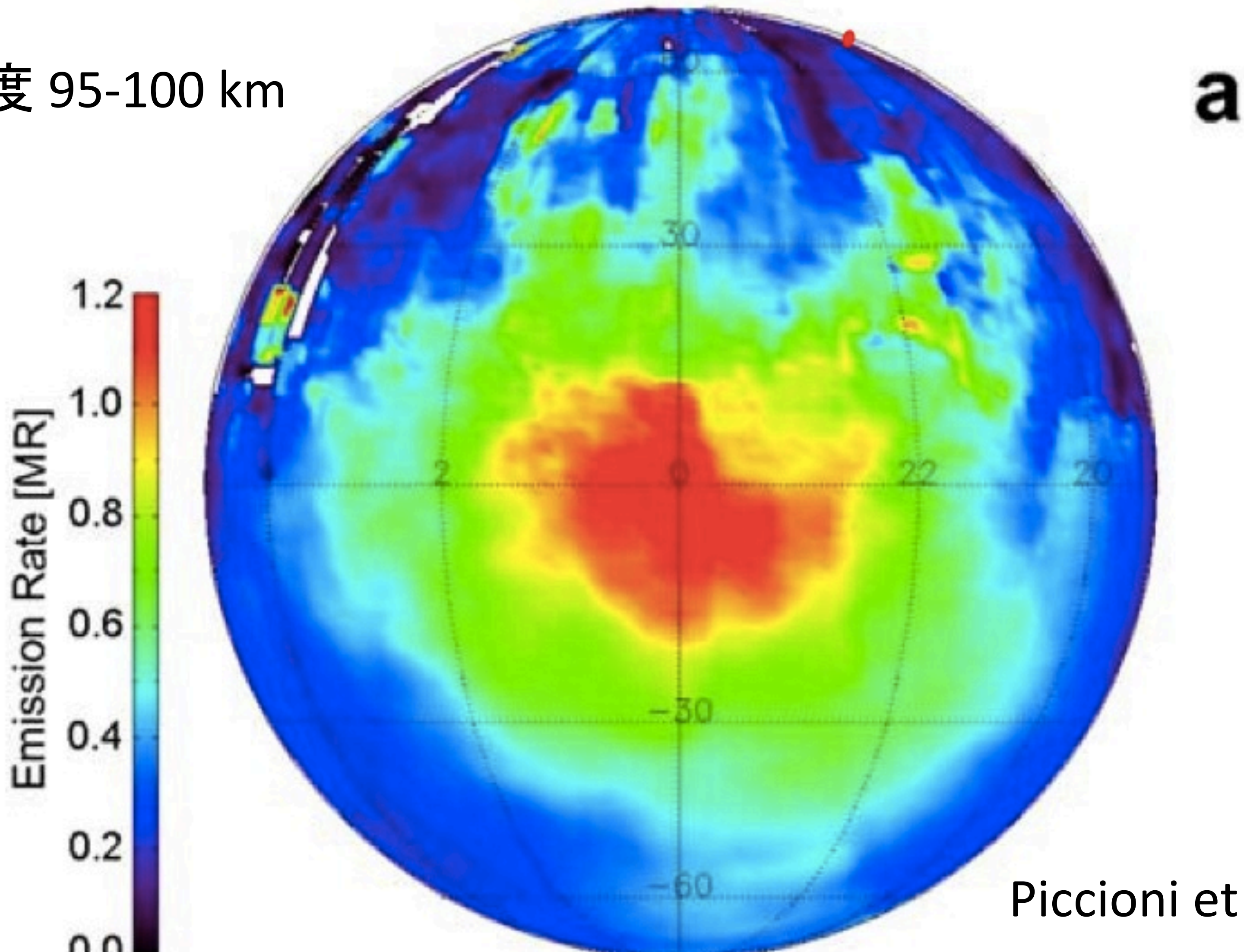

Piccioni et al. (2009)

Mean global map of the (0,0) oxygen nightglow

金星中間圏･熱圏の大循環

- 平均東西流と夜昼間対流が時間的･空間的に大きく変動している可能性がある。
- 夜光の強度変化から、大気大循環の変化の時間スケールは数時間～数日。
- VIRTIS/Venus Express の観測結果は平均東西流の存在に否定的。
- 中間圏･熱圏に平均東西流はあるのか、ないのか？

金星上層大気のモデリングの現状

東西風分布

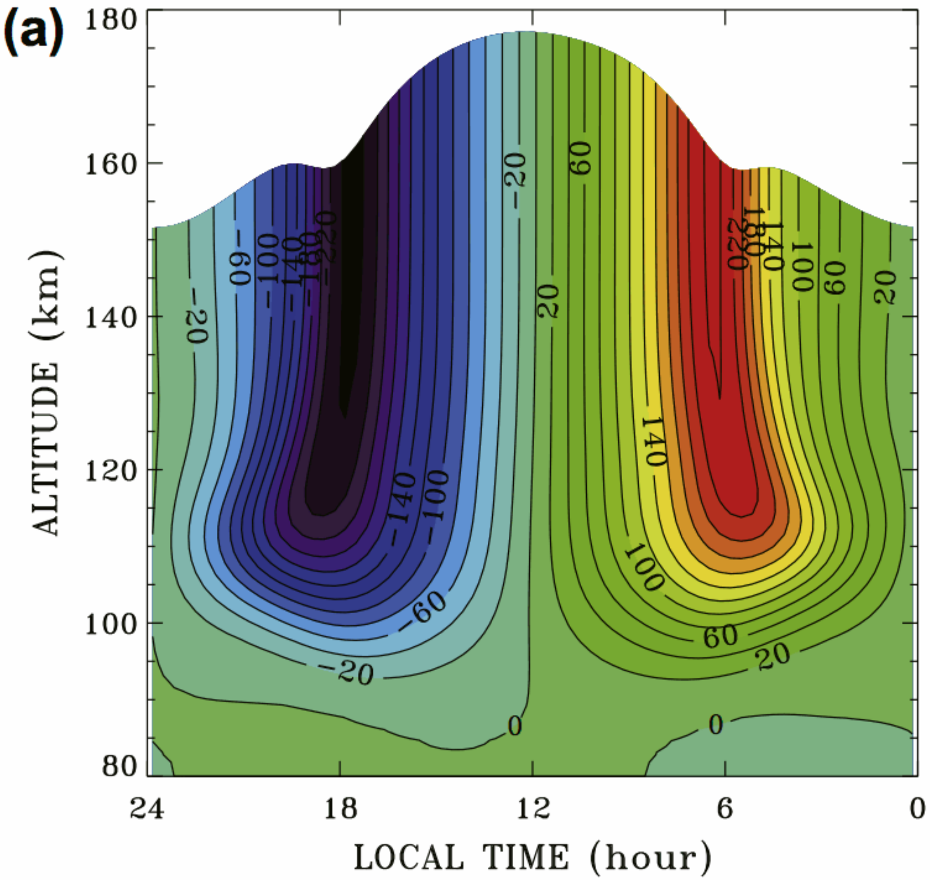

温度分布

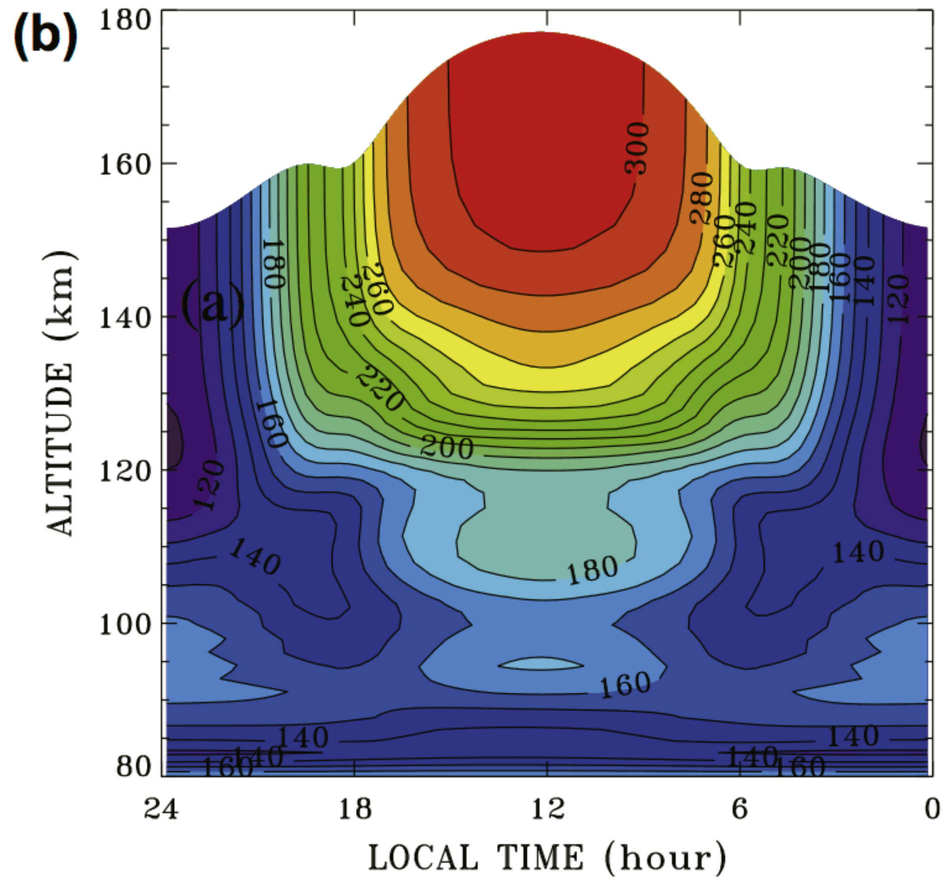

下層（70 km 以下）のスーパーローテーションを考慮しなければ、強い夜昼間対流の卓越を予想 (u~250 m/s)。

Hoshino et al. (2011)

O_2 夜光の強度分布

U = 0 m/s at 80 km

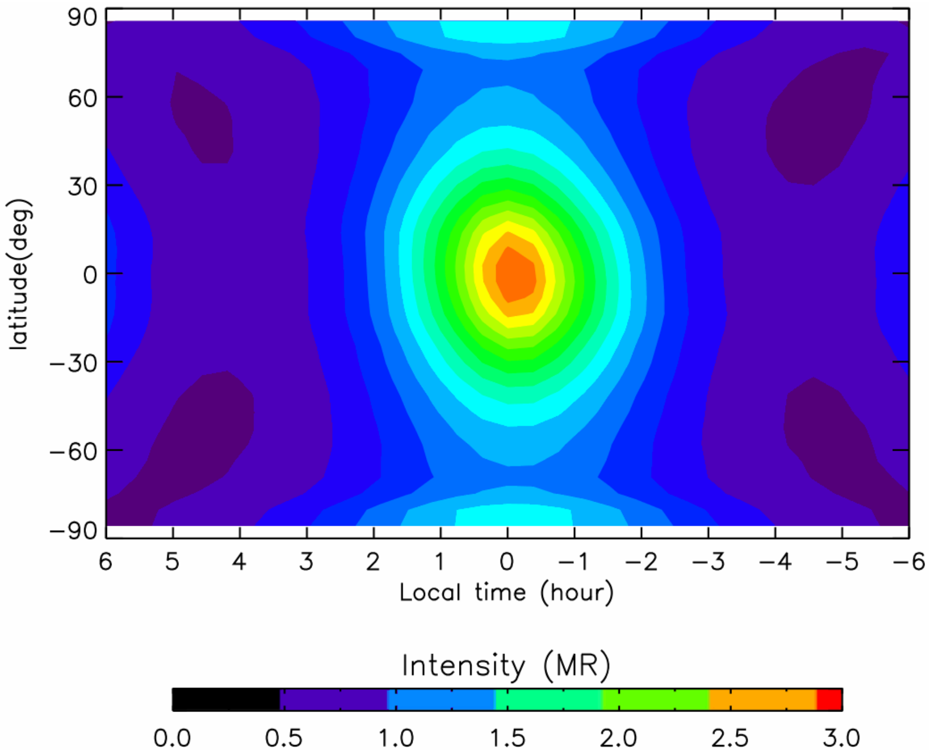

U = –40 m/s at 80 km

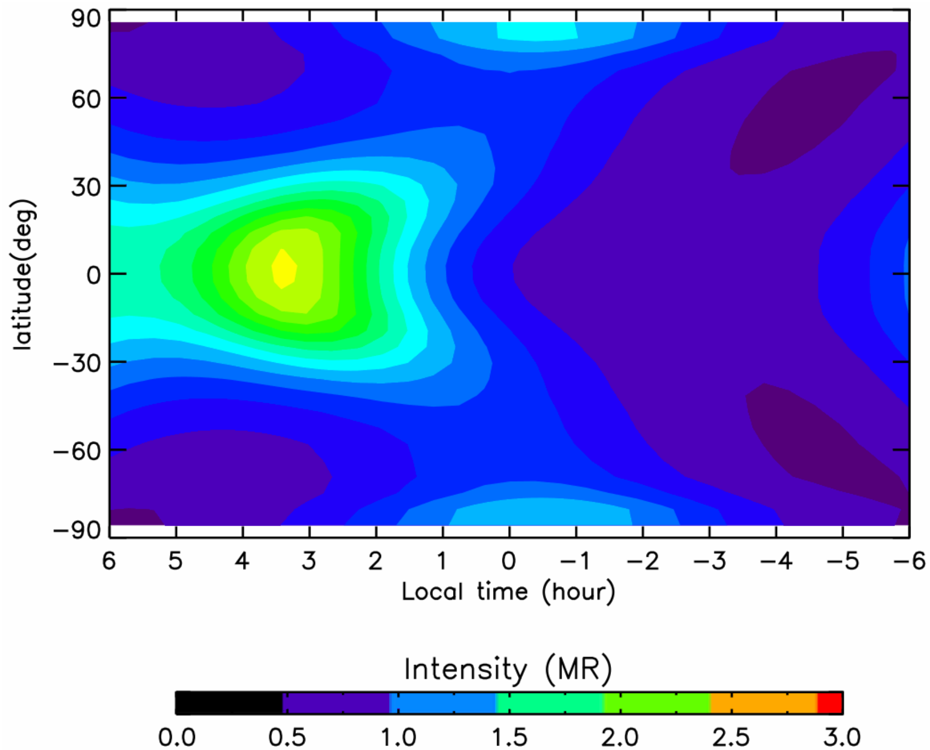

モデル大気下端 (80 km) で –40 m/s のスーパーローテーションを仮定した場合は、3.5LT 程度の朝側へのシフトが見られる。

Hoshino et al. (2013)

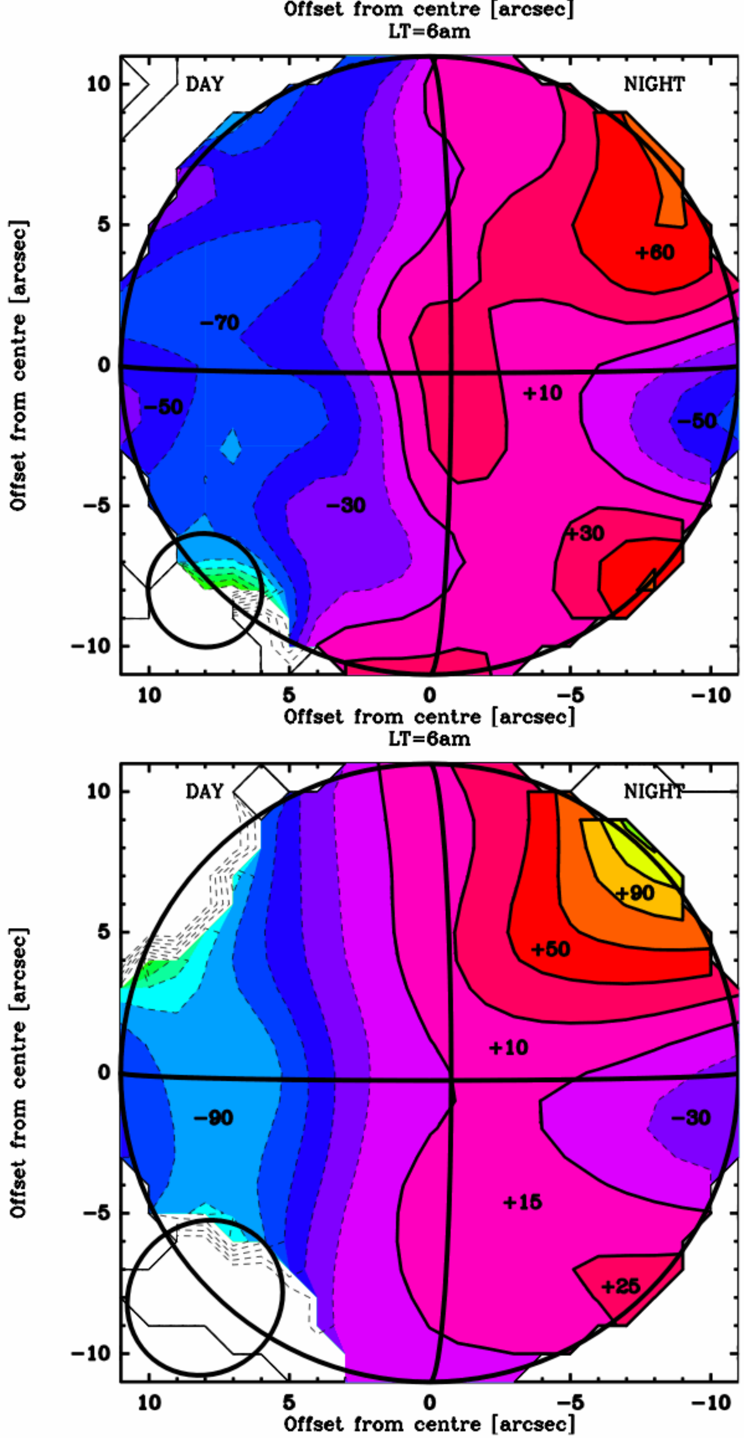

視線速度 (LOS velocity) の比較

左図: CO の吸収線観測によって測定した視線速度の分布。

右下の図: 大気大循環モデルの結果を左図と同様にプロットしたもの。（高度約 110 km, 下端でスーパーローテーションを与えた場合）

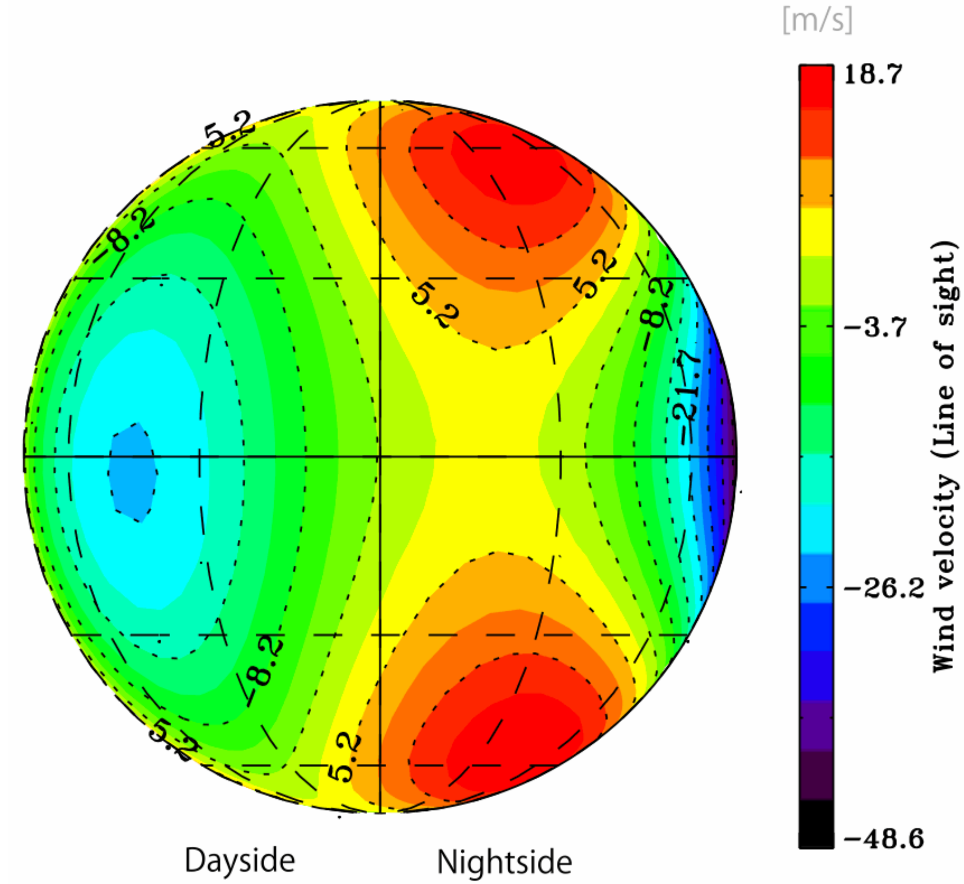

Hoshino et al. (2013)

Moullet et al. (2012)